

https://dspace.org/

Quantum transport in low dimensional carbon: from graphene to superconducting diamond

Coleman, Christopher

2018

https://hdl.handle.net/10539/25872

Coleman, Christopher. (2019). Quantum transport in low dimensional carbon :from graphene to superconducting diamond. University of the Witwatersrand, https://hdl.handle.net/10539/25872

Downloaded from a DSpace repository. https://dspace.org/



WITS
UNIVERSITY

Quantum transport in low dimensional carbon: From graphene to superconducting diamond

A dissertation submitted to the department of physics of the University of the Witwatersrand towards fulfilment of the requirements for the degree of doctor of philosophy

Christopher Coleman

February 2018

Declaration

I declare that this thesis is an original report of my research, has been written by me and has not been submitted for any previous degree. The experimental work is entirely my own work; the collaborative contributions have been indicated clearly and acknowledged. Due references have been provided on all supporting literatures and resources.

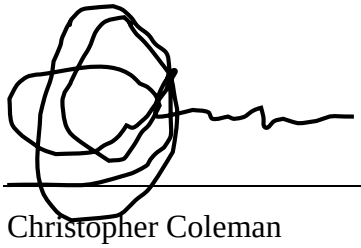

Christopher Coleman

1 June 2018

Abstract

In this work investigations into the quantum transport of two different low dimensional carbon systems are presented. Heavily boron-doped nanocrystalline diamond is known to be superconducting and has attracted much research attention as it forms a new class of superconductor; the doped semiconductor superconductor. The system follows a Mott transition with doping concentration and has thus lead to various proposed pairing mechanisms forming the Cooper pair, this includes phonon mediated as well as resonating valence band mechanisms for pairing. Although generally considered a three dimensional system to date very few reports exist on determining the dimensionality of the quantum conduction channels in the system.

I investigate the dimensional crossovers in transport using the well-known scaling analysis such as Azlomazov-Larkn and Lerner-Varlomov-Vinokur models to establish the characteristic dimensionality within the fluctuation regime and establish a two dimensional phase that occurs before Josephson coupling between grains becomes significant. The field induced superconductor to insulator transition is then investigated in light of the previously proposed charge-glass state that has been observed in other 2D superconducting systems. It is shown that there the predicted universal scaling analysis can in fact be applied to this system with critical exponents that follow the expected values Further supporting the claim of a 2D system. Subsequently one of the result of the two dimensionality, the Berezinskii-Kosterlitz-Thouless transition is observed through both current-voltage scaling as well as temperature dependent resistance. In addition to these aspects of low dimensional transport the possibility of Andreev bound states is exhibited in the differential resistance, these resonant features are related to the mid gap states observed in layered cuprate systems with anisotropic order parameter (d-wave).

Novel magnetoresistance features such as a change from negative to positive magnetoresistance (weak localization to anti-localization) is observed to occur in the fluctuation regime near the established BKT transition point, this is related to normal state electrons that undergo spontaneous time reversal symmetry breaking as the superconducting stage is reach. Such novel transport features are often related to signatures of topological non-trivial phases which can be of use for various quantum computation technologies. This work also investigates the effect of strain deformation on the transport in graphene. Raman annealing is proposed as a non-destructive tool for the formation of nano-scaled deformations, the effect

of the deformation on the phonon modes is discussed and related to possible psuedomagnetic field Landau quantization. A novel method utilizing nanomanipulators is employed for fabricating wrinkled multilayer graphene devices allowing for transport features to be compared to flat quasi-2D devices. The magnetoresistance shows a conversion from the 2DEG to a linear positive magnetoresistance with large deformation. These processes can be of interest for carbon based quantum technology. The suitability and possible fabrication methods for creating diamond based superconducting circuit elements are discussed.

Acknowledgements

The submission of this PhD. thesis sees the culmination of four years of work dedicated to research in quantum transport. There have been many ups and downs as well as many people who have supported and assisted me during this time. First and foremost, I would like to acknowledge my supervisor, Professor Somnath Bhattacharyya. Not only is he a pioneer of carbon based quantum and nano-technology, but has lead our research group with an enthusiasm and dedication that I have not seen matched in my short time as a researcher. The establishment of world class facilities at the Nano-Scale Transport Physics Laboratory (NSTPL) has allowed access to rich and interesting physics that was largely out of reach in South Africa at the time of his appointment, I am thus greatly indebted to him for the opportunity to have work in such interesting fields as that presented here.

Secondly I would like to acknowledge the previous and current members of my research group particularly Siphephile Ncube, Davie Mtsuko, Tahir Aslan, Ross Mcintosh and George Chimowa. I have learned much from each of them and value the time spent working together on our various projects. I have also been lucky enough to have had technical support from various individuals outside our research group, this includes Charles Sandrock, Rudolf Erasmus and Chris Both, without whom much of the work presented here would not have been accomplished.

Lastly, but by no means least, I would like to acknowledge my family and friends. The dedication required to complete this body of work has kept me quite busy during the past few years. The moral support as well as understanding during this time is much appreciated and will not be forgotten.

Contents

Abstract ii

Acknowledgements iii

Part 1: Superconductivity in boron-doped diamond 1

1 Introduction 2

1.1 Microstructure…….... 2

1.2 Band structure…… 7

1.3 Transport features……..…… 9

1.4 Pairing mechanism…… 11

1.5 Unconventional transport features…… 15

2 Two dimensionality of boron doped superconducting diamond 19

2.1 Fluctuation spectroscopy…….. 19

2.2 Fluctuation spectroscopy of granular superconductors……. 21

3 The field induced superconductor to insulator transition 29

3.1 Superconductivity and duality…….. 29

3.2 Signatures of the electron-glass phase…….. 31

4 The Berezinskii-Kosterlitz-Thouless transition 38

4.1 Phase transition without breaking symmetries…….38

4.2 Universal jump and the superfluid stiffness…….43

4.3 Effects of homogeneity, finite size and magnetic field……45

4.4 BKT features of the temperature dependent resistance……50

5 Additional unconventional transport features 55

5.1 Mid gap states, the anomalous zero bias conductance peak……. 55

5.2 Symmetry breaking and residual resistance…….. 60

Part 2: Strain engineering in graphene **67**

6 Strain engineering in graphene **68**

6.1 Dirac dispersion of graphene……68

6.2 Effect of strain on the electronic properties of graphene……..73

7 Nanoscale deformation through Raman annealing **77**

7.1 Phonon dispersion in graphene……. 77

7.2 Effect of disorder on the Raman spectrum……... 81

7.3 Effect of strain on the Raman spectrum……... 83

7.4 Raman annealing…….. 84

8 Deformation of multi-layered graphene through nanomanipulation **91**

8.1 Nanomanipulation of multilayer graphene…….. .91

8.2 Quantum linear magnetoresistance……...96

8.3 Landau quantization and Shubnikov de Haas Oscillations……. .98

8.4 High frequency response of suspended multi-layer graphene…… 104

9 Conclusion **107**

9.1 Graphene and superconducting diamond as suitable quantum matter systems for technological application……. 107

9.2 Future prospects and potential device fabrication techniques…….111

9.2.1 Incorporation of Raman annealing into electron beam lithography device fabrication…….…… .111

9.2.2 Contemporary diamond based microelectronics……... 116

9.2.3 Diamond based Josephson junction devices……..118

9.2.4 Fabrication of diamond electronic circuitry using FIB milling…….121

References **134**

List of publications **153**

List of figures

Figure 1	Microstructure of boron doped diamond from HR-TEM and EELS
Figure 2	Raman spectroscopy evidence for boron bilayer formation.
Figure 3	Band dispersion results from ARPES
Figure 4	MIT transition and critical temperature dopant concentration dependence.
Figure 5	RVB and antiferromagnetic lattice.
Figure 6	STM imaging and spectroscopy of vortex states of superconducting diamond
Figure 7	Anomalous Bosonic resistance peak
Figure 8	Diamond granular surface and temperature dependent resistance
Figure 9	Perturbation Diagrams indicating the main corrections to the fluctuation or excess conductivity
Figure 10	Normalized temperature dependent resistance with AL, LD and HN fittings
Figure 11	The Fluctuation conductance as a function of reduced temperature showing q-0D, 2D and 3D transport regimes
Figure 12	Temperature range of each dimensional crossover with BKT transition point below Tc
Figure 13	Phase diagram of disordered 2D superconductor
Figure 14	The BKT class of transitions.
Figure 15	Temperature dependent resistance at different applied fields, the field induced superconductor to insulator transition.
Figure 16	Zero Temperature critical field from the Ginzburg-Landau theory and vortex binding energy

Figure 17 Magnetoresistance at different temperature below T_C

Figure 18 Universal scaling analysis of superconducting boron-doped diamond

Figure 19 Vortex and anti-vortex forming around a topological defect and the vortex-antivortex binding

Figure 20 Vortex interactions in layered superconductor

Figure 21 Power law scaling of the Current-Voltage characteristics evidence of the BKT transition and superfluid stiffness

Figure 22 Effect of grain size on the BKT transition temperature

Figure 23 Effect of applied magnetic field on the BKT transition

Figure 24 Signatures of the BKT transition in temperature dependent resistance and the HN fitting

Figure 25 Logarithmic temperature dependent resistance and BKT analysis

Figure 26 ZBA in the temperature dependent resistance, below and above Tc

Figure 27 Temperature dependence of FWHM and ZBA peak height and FWHM

Figure 28 Schematic of the Mid Gap resonance states due to anisotropic order parameter

Figure 29 Field dependence of ZBA and split peak structure,

Figure 30 Inverse temperature dependence e of resistance, finite resistance regime

Figure 31 Low field magnetoresistance, WL to WAL transition

Figure 32 Magnetoconductance within the fluctuation regime at different bias and angle dependent magnetoresistance

Figure 33 Schematic of type 1 and type 2 Weyl semi-metals

Figure 34 Crystal lattice, reciprocal space and dispersion relation of graphene

Figure 35 Integer Quantum Hall resistance and Shubnikov de Haas oscillations of graphene

Figure 36 Effect of trigonal warping n the interference effects

Figure 37 Measurement of strain induced gauges through Aharonov-Bohm interferometry

Figure 38 Strain engineering in suspended graphene device

Figure 39 Phonon dispersion modes and lattice vibrations

Figure 40 Electron-Phonon resonances and the Raman spectrum of graphene

Figure 41 AFM and Raman conformal mapping for determination of number of layers of multilayer graphene

Figure 42 Effect of strain on Raman spectrum

Figure 43 AFM and Raman mapping of nanoscale deformation

Figure 44 Strain related splitting of the G-band

Figure 45 Signatures of quantum interference due to Pauli blocking in the 2D and D-bands

Figure 46 SEM micrographs of the nanomanipulation technique used for fabrication multi-layered graphene devices

Figure 47 Comparison of the Raman spectrum of single and multilayer graphene

Figure 48 Magnetoresistance of wrinkled multilayer graphene device.

Figure 49 Mangetoresistance of smooth multilayer graphene device, Landau quantization and Shubnikov de Haas oscillations

Figure 50 Inverse field dependence of the magnetoresistance oscillations

Figure 51 Properties of the charge carriers from Shubnikov de Haas oscillations

Figure 52 High frequency response of multi-layered graphene fabricated through nanomanipulation techniques.

Figure 53 Single layer graphene through scotch tape exfoliation technique

Figure 54 electron beam lithography resist etching

Figure 55 Single layer graphene device fabrication using electron beam lithography

Figure 56 Array patterned graphene devices

Figure 57 Diamond based NV-centre devices consisting of nitrogen implanted diamond arrays and the Diamond SQUID

Figure 58 Schematic of Majorana braiding for topological quantum computing

Figure 59 Junction devices for probing the order parameter

Figure 60 Multi-purpose deposition chamber

Figure 61 example of devices fabricated using FIB ion milling

Abbreviations and Symbols

HR-TEM	High Resolution Transmission Electron Microscopy
EELS	Electron Energy Loss Spectroscopy
XRD	X-Ray Diffraction
ARPES	Angle Resolved Photo-electron Emission Spectroscopy
CPA	Coherent Potential Approximation
σ_0	Normal state conductance
n_c	Critical boron dopant concentration
n_B	Boron dopant concentration
θ_D	Debye temperature
H_{C2} or B_{C2}	Critical magnetic field of type 2 superconductor
ΔB_C	Thermal distribution of critical field
Δ	Superconducting gap
T_C or T_M	Critical temperature (mean field critical temperature)
μ_0	Permeability of vacuum
μ_B	Bohr magneton
λ	London penetration depth or AL dimensional critical exponent
DoS	Density of states
RVB	Resonating Valence Band
Z_2	Symmetry class that is invariant between electric and magnetic fields
STM	Scanning Tunnelling Microscopy
BCS	Bardeen-Cooper-Schrieffer
MIT	Metal-Insulator Transition

VHR	Variable Range Hopping
BKT	Berezinski-Kosterlitz-Thouless
H-SIT	Field induced Superconducting to insulating transition
SQUID	Superconducting Quantum Interference Device
2D	two dimensional
3D	three dimensional
q-0D	quasi- zero dimensional
AL	Azlamazov-Larkin
LVV	Lerner-Varlamov-Vinokur
LD	Lawrence-Doniach
HN	Halperin-Nelson
$\Delta\sigma$	Excess/fluctuation conductivity
$\Delta\sigma_{2D}$	Two dimensional fluctuation conductivity
$\Delta\sigma_{3D}$	Three dimensional fluctuation conductivity
ε	Reduced temperature within AL formalism
d	Interlayer spacing
D	Diffusion constant
R	Resistance
R_N	Normalized resistance w.r.t normal state
E_C	Charging energy of individual grain
E_J	Josephson coupling energy between grains
Γ	Tunnelling energy
E_T	Thouless energy
QMTV	Quantum Macroscopic Tunnelling of Vortices

vz	Critical exponent describing Bose-glass phase
I	Current
V	Voltage
I_C	Critical current
J_S	Superfluid stiffness
J_C	Superfluid stiffness along c-axis
J_{ab}	Superfluid stiffness in ab-plane
J_{BCS}	Superfluid stiffness predicted by BCS model
μ_{XY}	Vortex core energy according to the XY model
μ/J_S	Reduced vortex core energy
t_c	reduced temperature within HN formalism
Λ_J	Pearl screening length
Λ	In plane screening length
Λ	out-of-plane screening length
K	Superfluid coupling
g	Vortex fugacity
L_{phys}	Length of homogeneous regions affecting BKT transition
L	Length of sample
φ_0	Flux quantum
ABS	Andreev Bound State
dI/dV	Differential conductance
FWHM	Full Width at Half Maximum
WL	Weak Localization
WAL	Weak Anti-localization

HLN	Hikami-Larkin-Nagaosa (equation)
QLMR	Quantum Linear Magnetoresistance
ABA	Bernal stacking order of trilayered graphene
MR	Magnetoresistance
NV-centre	Nitrogen Vacancy-centre
MIKD	Microwave Inductance Kinetic Detector
HEB	Hot Electron Bolometer
JJ	Josephson junction
FIB	Focused Ion Beam
S/F	Superconductor/Ferromagnet junction

Part 1

Superconductivity in boron-doped diamond

Chapter 1

Introduction

1.1 Microstructure and composition

Superconductivity was discovered in heavily boron doped single crystal diamond in 2004 [1] and along with Silicon and germanium form a new class of covalently bonded doped superconductors [2,3]. Since then in addition to single crystal, superconductivity has been observed in polycrystalline [4] as well as nanocrystalline [5] boron doped diamond films as well. As diamond is commonly known to be a wide band gap insulator, the discovery was quite unexpected and soon after the initial discovery inspired a surge of research to understand the possible pairing mechanisms as well as some of the properties of the metallic and superconducting phases.

The study of boron and nitrogen doping in diamond is well established and thanks to breakthroughs in synthesis techniques that allowed for the fine tuning of transport and structural properties in synthetic diamond systems much is known about the relationship between microstructure and electronic transport. Nitrogen doping in diamond allowed for the production of n-type metallic samples which showed that the smaller the grain size the more a graphitic or sp^2 phase featured in spectroscopic measurement [6]. It was found that nanocrystalline diamond grains were connected through a graphitic network which allowed for a percolation transport along the grain boundaries [7]. On the other hand, early studies on boron doping of diamond yielded interesting spectroscopic features; It was found that the deep lying (~ 36 eV) boron acceptor state was doubly degenerate that exhibited spontaneously broken time reversal symmetry at low temperatures due to a static Jahn-Teller effect probed directly through cryogenic Raman spectroscopy and Fabry-Perot Interferometry measurements [8].

The effect of the boron doping on the microstructure of the superconducting films has also enjoyed a large amount of attentions. High Resolution Tunnelling Electron Microscopy (HR-TEM) studies have revealed that in granular samples, particularly in samples with micrometre grain size, the boron aggregates and forms triangular pockets between diamond crystal

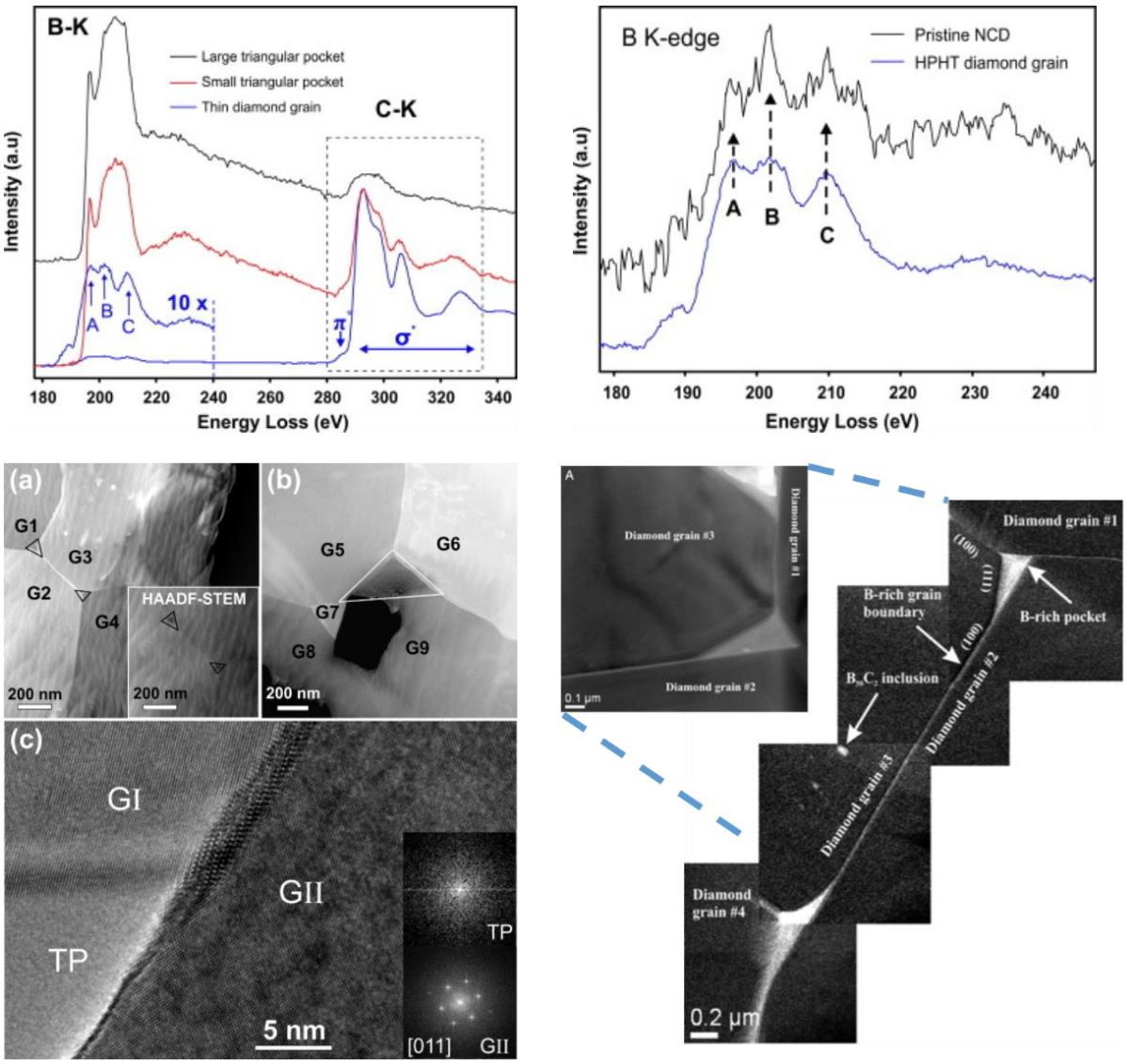

Figure 1. (a) EELS mapping of the B-K and C-K ionization edges has been used to map boron and carbon distribution in boron doped diamond systems. Pronounced signals from boron is generally dominant in the intergranular triangular pockets and along the grain boundaries. (b) The EELS spectrum for the boron rich regions do not show rhombohedral phase of boron instead show an amorphous boron-carbide phase. (c) HR-TEM images of the granular structure, the triangular boron pockets can clearly be seen at the diamond corners. Also visible is the boundary region composed of an amorphous carbide (d) EELS mapping of the boron content, some intergranular boron inclusions also exist near the diamond edge. Images adapted from references [9,10]

grains [9,10]. The grain boundary showed a distinctive born phase that connected the triangular pockets and separated boron rich diamond surfaces as indicated in figure 1 (c & d). Other studies did however reveal diamond grains without boron interfacial phase [11]. The HR-TEM studies were usually accompanied with complimentary Electron Energy Loss Spectroscopy (EELS) which proved useful in determining composition of the different boron rich regions. The EELS mapping was conducted on both the boron K and carbon K ionization edges and showed that the triangular pockets were composed of an amorphous boron-carbide composed of approximately 95 % boron and only 5 % carbon. Such EELS mapping also showed that the interior diamond structured grains had a homogeneous dispersion of boron concentrated near the surface of the grains. The grains however did show some isolated regions of high boron concentration where the boron inclusion formed plate-like structures. These investigations into the microstructure revealed that the in the granular samples the morphology is fundamentally different from other granular superconducting systems. The authors of [11] took this along with supporting data to indicate that the intergranular boron network was responsible for the superconductivity instead of the diamond, this idea has however not yet been confirmed and is by no means the general consensus. More recent structural studies [12] employing a combination of X-Ray diffraction (XRD) and Raman spectroscopy of high quality large crystal (mm scale) samples have come to an entirely different conclusion regarding the microstructure and its role in inducing the superconducting state. The authors of reference 12 exhibited data that suggested the formation of C-B bilayer sheets that occur along the {111} planes, this included high-order, super-lattice reflections in X-ray diffraction and Laue patterns which unambiguously showed an incommensurately modulated structure due to the displacement of boron atoms. Through electronic excitations measured using Raman spectroscopy they showed the formation of a new acceptor level of approximately 37 meV associated with the B-C sheets. The same authors also claimed to measure superconducting phase only along the (111) crystal planes. It should also be noted that most structural studies have been conducted on samples with grain size in the micro to milli-meter range and a lack of information on nanocrystalline boron doped diamond exists. Although there is still some confusion regarding the origin of the superconducting phase as well as its relationship to the microstructure and boron-carbon ratio, these structural studies have highlighted some important features of this system; The boron doped diamond films do not show the morphology of generic granular superconducting systems. This is because in the case of superconducting diamond, the boron interfacial material

forms a sub-system that alternates with the diamond system in a somewhat ordered fashion similar to a superlattice, in conventional granular superconducting material there is usually no additional subsystem separating the individual superconducting grains. Additionally, the granularity of the superconducting diamond system was shown to be vital in controlling many of the transport properties, particularly in nanocrystalline samples where grain diameters approach tens of nanometres. For example, it was shown that the properties such as critical temperature, localization radius at the boron site, normal state resistance, coherence length, Hall mobility as well as the H_{C2}-T phase boundary were all grain size dependent [13], and as the grain size can be controlled through synthesis parameters offers a great deal of control over physical properties of the system. Raman spectroscopy proved to be vitally important in understanding structural properties as well as developing a deeper understanding of the electron-phonon coupling which is believed by many to be the most probable mediators of the Cooper pairing. Raman spectroscopy has also identified some interesting features in superconducting systems, a most notable regularly observed phenomena is a Fano resonance that occurs around a wavenumber of 1330 cm^{-1} when the system is doped to appropriate boron concentrations to induce the metallic phase [14]. Raman spectroscopy was also used to observe the change in critical temperature with Boron doping concentration due to relaxed electron-phonon coupling [15], such studies were used early on as a means of testing the Bardeen-Cooper-Schrieffer (BCS) theory. Raman spectroscopy has also helped in differentiating this material from the metallic N-type nanocrystalline diamond systems where it has been shown that as the grain size decreased, a more significant sp^2 hybridized carbon species existed, which was likened to multi-layer graphene platelets [15]. In Boron doped diamond however it was found that for decreasing grain size, the sp^2 phase would decrease and boron would be more significant [16]. As mentioned above electronic excitations have also been measured in boron doped diamond using Raman spectroscopy [12]. Some of the most notable studies involved investigations into the excitations involving the boron acceptor state and the spin-orbit split top of the valence band, as reported in [12] the boron dopants can self-assemble into plate-like sheets forming bilayer structures along the [111] crystal plane. These boron bilayers are supposedly responsible for the Raman bands that occurs at approximately 480 and 1230 cm^{-1} when the diamond system is doped into the metallic phase. The B-C bilayers were also claimed to result in a new acceptor level at around ~ 37 meV and was able to mix with the spin-orbit split diamond valence band. The Raman features, particularly observations of new phonon modes, Fano resonance and depletion of sp^2 phase are all significant evidence for the formation of an impurity band related to the boron doping.

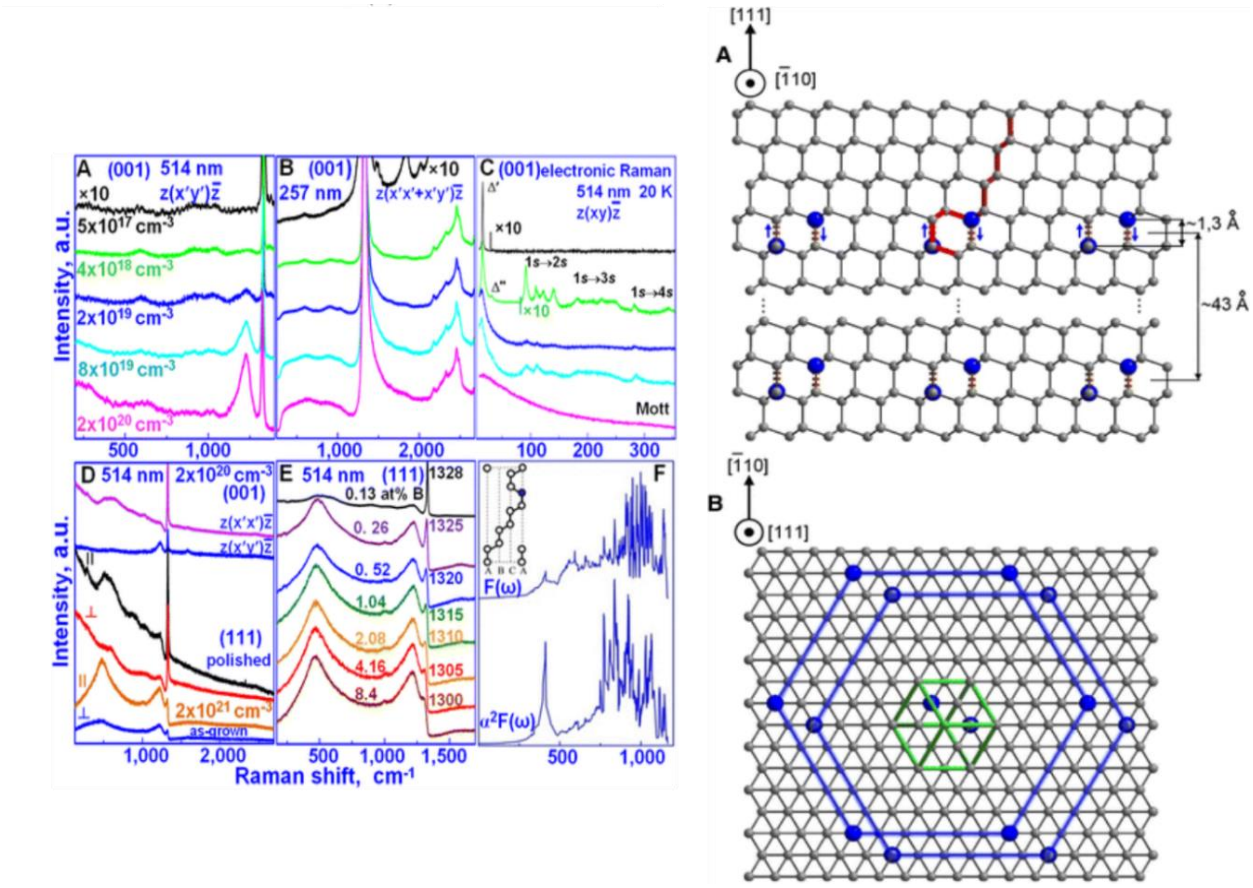

Figure 2 (a) Electronic Raman spectroscopy has been used to investigate the phonon modes across the insulator metal transition with increasing boron concentration. On approaching the metallic phase (and hence superconducting phase) bands corresponding to an impurity level due to B-C has been claimed. Transitions between spin-orbit split valence bands and this impurity band have been mapped. (b) a 2D phase corresponding to B-C layers composed of boron dimers in the diamond lattice has also been suggested from XRD data. Figure adapted from reference [12]

1.2 Band structure

Although the band structure of pure diamond as well as the effect of boron doping has been well researched, the exact implications of inducing a metallic state through heavy boron doping on the band structure is one of the most controversial aspects of research in this material. There are at least two schools of thought regarding the effect of boron doing, the first is related to hole occupation within the intrinsic valence band of the diamond due to substitutional boron doping, the second is related to the formation of an impurity band due to overlap and hybridization of low lying boron acceptor states. This is not a trivial distinction as the pairing mechanism and hence much of the underlying physics of the system can be heavily influenced by the band structure. Work conducted on single crystal samples using angle resolved photo-electron spectroscopy (ARPES) has revealed that upon doping single crystal diamond through the metal-insulator transition, the Fermi-level shifts in a rigiedd manor into the valence band thus adding hole carriers to the top of the valence band [17]. This work was conducted on [111] oriented films along the $\Gamma \rightarrow K$ direction in the Brilloiun zone and is shown in figure 2(a). This was initially taken as direct evidence for the intrinsic diamond bands interpretation for the band structure of the metallic phase, however more recently additional ARPES measurements [18] have been conducted along different directions in the Brillouin zone for [100] oriented single crystals and epitaxial films. Such studies were conducted as the effect of spin-orbit coupling on the top of the valence band is expected to lead to interesting phenomena such as warping of the valence band near the Γ point. The spin-orbit splitting of the top of the valence band was indeed observed along certain directions in the Brilloiun zone this is shown in figure 3 (b) where the band structure along the $\Gamma \rightarrow K$ and $\Gamma \rightarrow X$ directions are compared. Through this study the authors were able to extract Luttinger parameters and hence hole masses for these valence bands [18]. It should also be noted that the ARPES experiments conducted thus far on the boron doped diamond have all been concerned with bulk features in single crystal samples. To date no work focusing on surface band structure of this material has been, to my knowledge, conducted. This is quite surprising as experiments have already indicated that both pristine diamond (100) and (111) surfaces exhibit negative electron affinity due to low lying conduction band 7.5 eV above the valence band [19], other works based on ARPES of hydrogenated and pristine diamond surfaces established the formation of two surface states, bonding and antibonding which are degenerate at the J points in the Brillouin zone and related to the dangling bonds of the terminated diamond surface as well as the C-C bond length that was found to be substantially different from the bulk diamond [20]

.

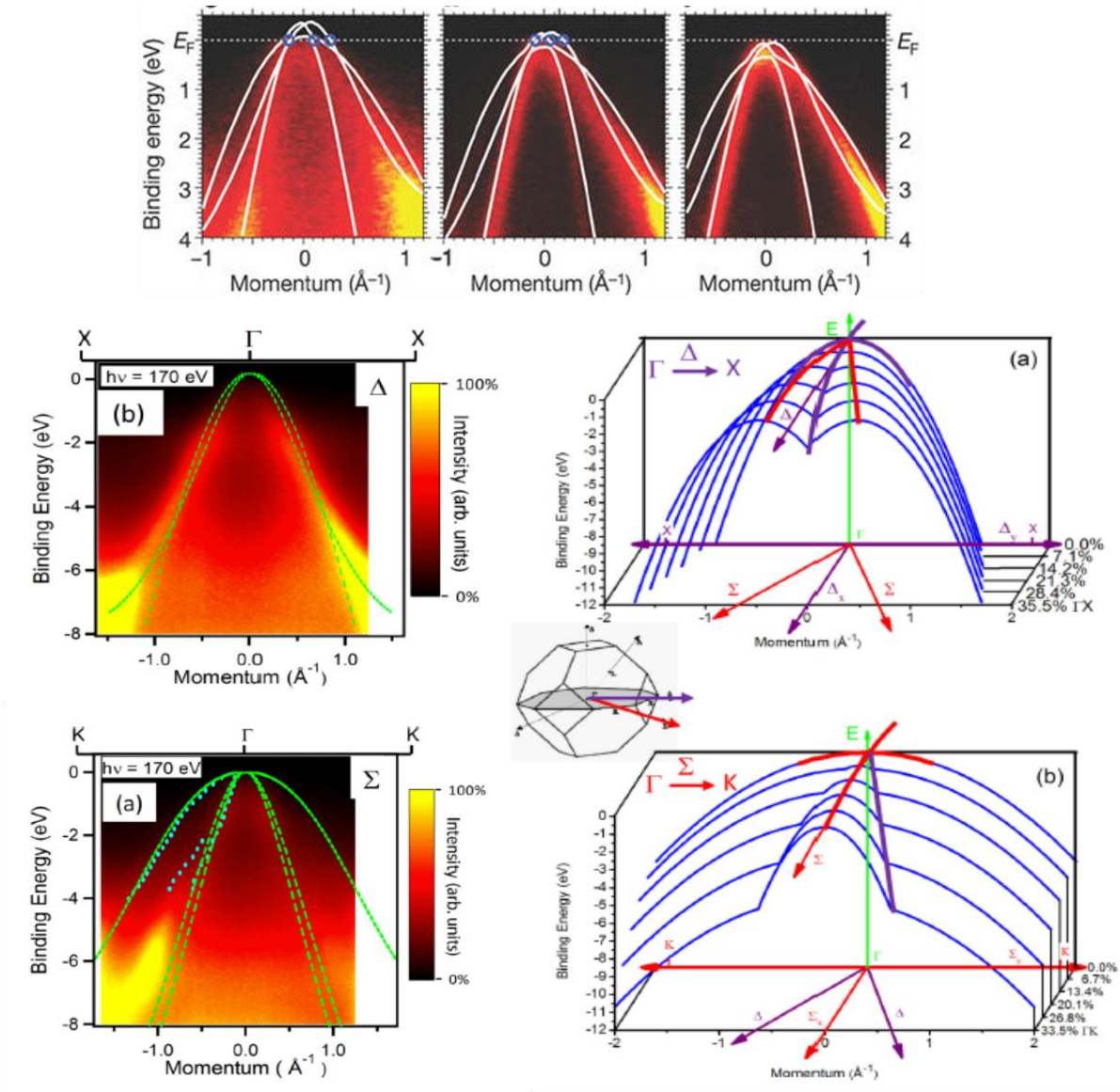

Figure 3. (a) ARPES on single crystal [001] oriented boron doped diamond single crystal samples along the Γ – K direction, a rigid shifting of the fermi level below the top of the valence band with increasing doping concentration is observed (b) More recent studies have looked at the evolution of the bands near the Γ point but along different directions of the Brillouin zone. It has been shown that along the D direction the bands split and can show complicated divergence due to spin-orbit coupling. Figure adapted from references [17and 18]

1.3 Transport features

In terms of transport studies most of the initial work was conducted on investigations relating to the mechanism of Cooper pair formation. One of the initial aspects that enjoyed a great deal of research attention was the metal-insulator-transition (MIT) in single crystal samples. The MIT is a well-documented phenomenon and allows for an ideal system to test theoretical models relating to doping induced superconductivity in semiconductors, essentially it allows for the doping concentration to be used as an experimental parameter to drive the system between phases. It was observed that at critical boron concentration of $n_c \sim 4.5 \times 10^{-20}$ cm^{-3} the MIT occurs [21]. The superconducting phase has been observed only in samples on the metallic side of the transition i.e. $n_B > n_c$. On the insulating side of the transition the system exhibits transport properties closely following variable range hopping (VRH) [22], however as the boron concentration is increased the VHR temperature decreases until the metallic phase is reached where the normal state resistance is best fitted to transport models taking into account quantum interference effects [23]. In this regime the conductivity was found to scale as:

$$\sigma_0 \propto \left(\frac{n_B}{n_c} - 1\right)^{\upsilon} \qquad (1)$$

Where the critical exponent was determined to be $\upsilon = 1$, this behaviour is similar to other disordered metals and semiconductors, a clear indication that weak localization effects plays a crucial role in transport of the normal state.

Studying the experimentally accessibly parameters of the MIT (such as T_c behaviour) allowed for the development of a number of theoretical investigations. Most of the founding theoretical work focused on studies related to electron phonon coupling, specifically involving the coupling of phonons to holes in the top of the σ bonding bands [24].

Accordingly the critical temperature was experimentally shown to roughly follow a $(n_B/n_c - 1)^{1/2}$ behaviour and was explained as a result of slow decrease in the coupling constant with increasing dopant concentration [25] which is counter intuitive as the electron-phonon coupling is expected to increase approaching the MIT, this contradiction raises questions on the validity of such phonon mediated transitions.

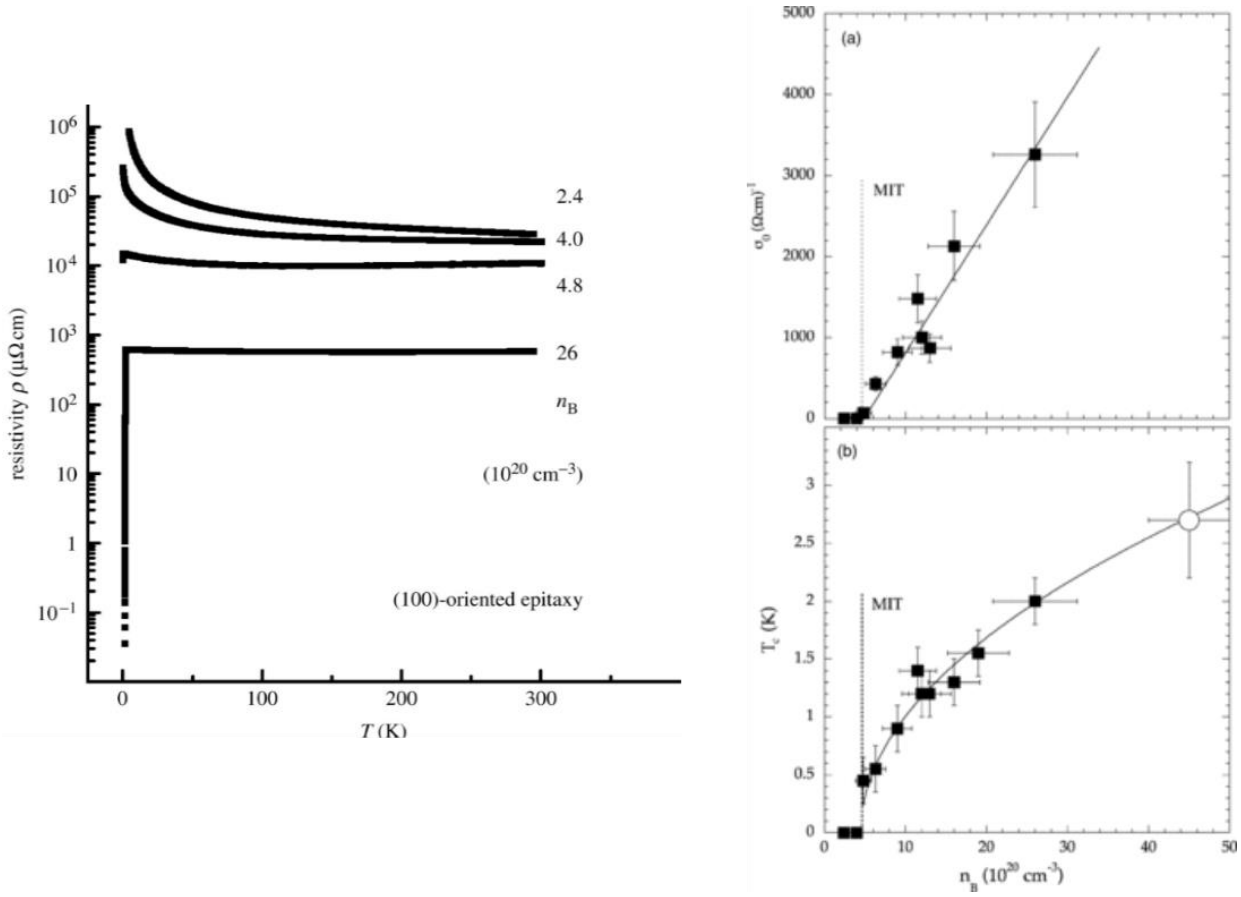

Figure 4. Various experimental findings regarding the transport properties correlated to boron concentration (a) the temperature dependent resistance showing the insulator-metal transition with increasing doping concentration. (b) The conductivity as a function of boron concentration (c) The critical temperature as a function of boron concentration, the straight line is a fitting to the equation 1. Figures obtained from references [21, 22, 23]

1.4 Possible pairing mechanisms

The initial theoretical studies revolved around the electron-phonon coupling as the likely pairing mechanism, this was seen as a consequence of the coupling of phonons to holes in the top of the σ bonding bands, a scenario used to explain the high T_C in the MgB_2 system [26]. However, the MgB_2 has a graphitic-like lattice and is thus quasi-2D with a higher electron-phonon coupling than the 3D diamond lattice thus limiting the T_C in diamond from reaching comparable values to MgB_2. As these models allow for an investigation of the electron-phonon coupling they could immediately be compared to experimental data. This is done through the McMillan relation [27]:

$$T_C = \frac{\theta_D}{1.45e^{-1.04(1+\lambda)/\lambda}} \qquad (2)$$

Where θ_D is the Debye temperature known to be 1860 K for diamond and λ is the electron-phonon coupling constant. These models were successful in matching, at least quantitatively, the properties of the experimentally observed Critical temperature behaviour.

One notable body of work was conducted on the use of the coherent-potential-approximation (CPA) within the diagrammatic perturbation formalism, which allows for the introduction of disorder [28]. There studies were concerned with determining quasiparticle life time as well as density of states and concluded that the evolution of the impurity states with increasing doping, i.e. the formation of impurity bands, may be of vital importance for describing some of the physical properties. Essentially it was found that the impurity levels broaden and gain weight as the doping concentration is increased and intersect the valence band at around n_B = 0.2 %. This work was able to determine critical temperature within the experimentally observed range (near 5 K) and suggested that higher doping concentrations as well as lower levels of disorder would lead to higher critical temperatures. This was later experimentally verified through the work of Y. Takano who grew polycrystalline films of low disorder and claimed critical temperature onset as high as 25 K [29], the highest reported value to date. However as previously explained, this work contradicts the ARPES data [17] which showed a rigid shift of the Fermi surface into the valence band with increasing dopant concentration. The limitations of the model were due to simplifications such assuming a simple cubic lattice, this has the consequence of ignoring the degeneracy of the valence bands, which was determined to be of important by other groups.

Similar concepts based on theoretical work such as ab initio and virtual crystal approximation were also conducted but proved to be less successful as they expected a fast decrease in the electron-phonon coupling. Electronic structure of B-doped diamond was studied based on first-principles calculations with supercell models for substitutional and interstitial doping at 1.5–3.1 at.% B concentrations. Substitutional doping induces holes around the valence-band maximum in a rigid-band fashion. The nearest neighbour C site to B shows a large energy shift of 1s core state, which was related to experimental features in photoemission and X-ray absorption spectra [30]. Such work, particularly the ab initio studies, however were based on the electronic structure of ordinary pure metals and not on the disordered Mott metal which the system is known to be and thus do not capture the full picture of electron correlations most notably localization effects which are known to play a role in the transport.

In addition to the phonon mediated BCS type pairing, very soon after the initial discovery a few groups have attempted to introduce various unconventional pairing mechanisms based rather on carrier correlations. Prompted by the Mott metal behaviour of the metallic state there have been reports on the possibility of quantum interference effects between weakly localized holes as a possible mechanism for the initiation of the superconducting phase transition, essentially redefining the system as an unconventional superconductor [31]. This idea resulted as competition to the phonon mediated picture because most of those theoretical models supporting that idea modelled the system as an ideal conductor not taking into account the Mott metal nature of the system or the effects Coulomb repulsion which is intuitively thought to be significant in such an insulating system. It was argued that two holes on adjacent boron acceptor sites would be able to overlap, in order to conform to Pauli's exclusion principal a spin-flip event may be necessary for such a hole pair. This energy of such a spin-flip event is:

$$\frac{\Delta}{2} = \frac{\mu_0 \mu_B^2}{b^3} \qquad (3)$$

Where μ_0 is the permeability of vacuum, is the Bohr's magneton and b is the effective (C-C≈C-B) bond length. The value obtained for the energy gap of the hole pairing obtained was $\Delta = 3.6 \times 10^{-4}$ eV, which when used in the Coopers relation:

$$2\Delta = \Lambda k T_C \qquad (4)$$

Gives a value of $\Lambda = 5.1$ which is comparable to the theory prediction for weak metals being $\Lambda = 3.52$. It should also be noted that there are multiple theoretical reports that have been

developed to explain phenomenological models explaining superconductivity in terms of the Cooperon propagator [32]. Essentially allowing for quantum interference effects and superconductivity to be explained using the same model. Although this model lacks a theoretical description it does highlight the possible unconventionality of the system as well as introduces a novel pairing mechanism that may be more relevant for the Mott metal related to weak localization interference effects.

This mechanism was heavily influenced by the work of Baskaran and Anderson who introduced the concepts of resonating valence bond (RVB) mechanism within the impurity band [33]. The RVB is concerned with describing gapped quantum matter, such as the Mott insulator, by a degenerate ground state that is made up of a linear superposition of a large number of different configurations of electrons paired into singlets. This phase of matter is different from paired states such as antiferromagnets which have long-range order but a non-degenerate ground states, shown in figure 5 (a and b). This model is very similar to Pauli's original ideas on resonating π-bonds in the benzene molecule. Kivelson showed that such a resonating ground state would allow for exotic phenomena such as fractionalization whereby the electron wave function is splintered into quasi-particle excitations analogous to photons allowing for spin and charge separation [34]. Lattice gauge theory was adopted as the most convenience theoretical language as it most neatly captured the underlying physics of such systems and as a consequence much theoretical work was then developed around identifying specific gauge symmetries in order to identify possible ground state configurations. One such phase that enjoyed some success was the quantum dimer model on the Kagome lattice which is an example of a Z_2 phase [36]. The Z_2 RVB phase was shown to have a gap to all excitation and therefore could be appropriately applied to gapped quantum systems with long ranged entanglement such as the Mott insulator. In this gauge theory a gapped excitation called a vison was predicted, this quasiparticle carries neither spin nor charge, transporting only energy and is thus analogous to dark matter. What makes the RVB mechanism interesting is that the degeneracy of the ground state of the system is directly dependent on the topology of the spin (dimer) manifold (figure 5 c and d). In other words, this state is topologically ordered. This is can be visualized by considering the manifold with specific topology, i.e. the torus shown in figure 5, the red line intersecting the manifold will cut through a certain number of valence bonds which is directly determined by the bond configuration of the ground state, thus the degenerate ground states can be categorized in terms of the conservation of the number of cut

valence bands. This means that the topological order of the ground state is a quantum number for that state.

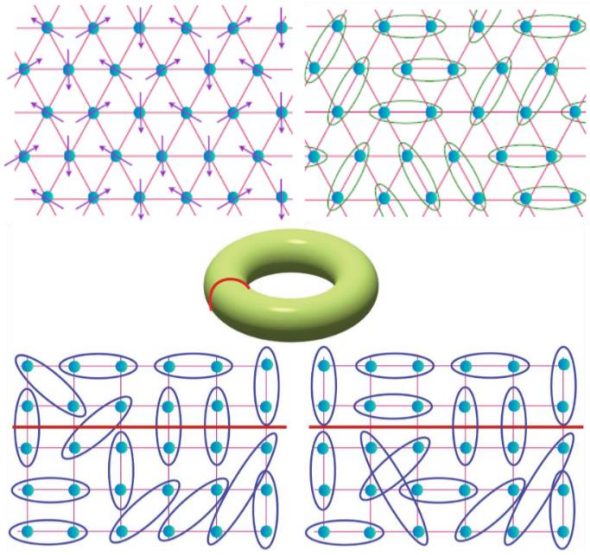

Figure 5. Schematics showing (a) the Kagome lattice where the antiferromagnetic state is considered as a gapless ground state, this can be contrasted to the (b) RVB ground state which is degenerate and is considered gapped. (c) the RVB ground state is considered to topological non-trivial as the topology of the spin/charge manifold leading to the singlet pairing determines the state of the system, this is indicated in (d) where two systems of different topological numbers (dimers crossing the cut) constitute two distinct ground states even though the number of dimers is conserved between them. Schematics obtained and adapted from reference [33]

The concepts have been applied to superconducting boron doped diamond. As argued by Baskaran [36], the high doping density in the boron doped diamond system is comparable to the critical density expected for an Anderson-Mott transition therefore indicating the electron correlations are vital in explaining the transport features of the system. The system was thus described within a RVB impurity band model where diamond, negligible electron correlations, offers a "vacuum" to boron subsystem. Within the diamond the random coulomb potential would remove the three fold degeneracy of the acceptor states.

This is expected to induce a single, narrow band of holes. Such a system would allow for Singlet pairing between spins of neighbouring neutral acceptors B^0–B^0. Crossing the insulator to metal transition, charged B^+ and B^- states (free carriers induced at the boron sites) get spontaneously generated and are delocalized. This delocalization coupled to the random

coulomb potential causes resonating behaviour of the pairing of the singlets resulting in a resonating valence bond superconducting state.

1.5 Unconventional transport features

One of the most useful and widely used experimental methods for determining properties of the supercondensate is scanning tunnelling microscopy (STM). This method relies on detecting the local density of states using tunnelling processes and is frequently used to probe the order parameter, superconducting gap as well as spacial distribution and dynamics of vortex states. The first studies on superconducting boron doped diamond claimed a conventional BCS features where vortices form an Abrikosov triangular lattice [37]. Accordingly Later more precise measurements indicated that the superconductivity follows the granular structure with mostly well connected, transparent grain boundaries and fewer more weakly coupled (opaque) boundaries [38]. This study also showed that there existed in addition to the BCS-type a non-BCS differential scanning conductance.

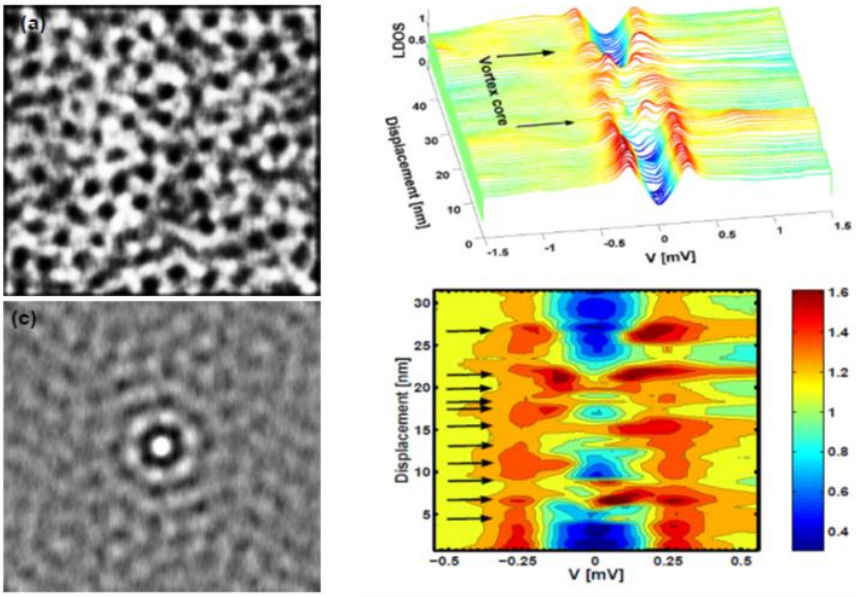

Figure 6. (a) A low temperature STM image showing the vortex configuration at low magnetic fields, a disordered Abrikosov lattice can clearly be seen particularly in (b) where the Fourier transform of the image has been made. (c) High resolution STM measurements have also been performed on single vortex states, it was found that there is a definite signature of non-zero density of states that occur near the vortex core. Figure taken from references [38,40]

Because of the strong coupling between grains, a proximity effects occurs in weakly superconducting grains and inverse proximity effect in strongly superconducting grains. STM measurements on homoepitaxcial diamond films showed different STM spectra for (111) and (100) planes, this is a clear indication of anisotropy [39].

Additionally quasiparticle excitations below the superconducting energy gap were observed within the vortex core [40]. This is significant when taking into account some of the theoretical investigations regarding the relationship between odd frequency superconductivity and vortex bound states. In fact an entire range of STM spectra are expected for quasiparticle excitations with different wave function pairing regarding orbital momentum (parity) and frequency such bound states have non-trivial topology [41].

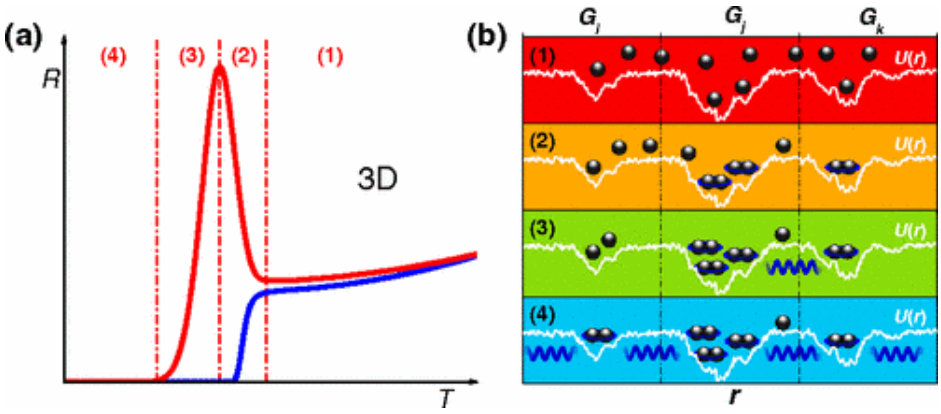

Figure 7. One of the first transport features signifying unconventional superconductivity was the re-entrant bosonic anomaly reported by Zhang et al. This feature was explained with in a resistive network model composed of bosonic islands within the diamond grains that eventually reach global coherence and hence the superconducting phase. Figure taken from ref. [41]

More recently however additional unconventional features have been observed in the transport of nanocrystalline samples. Re-entrant peak structures below the T_C that are strongly field dependent were demonstrated by several group [41, 43]. The re-entrant peaks where initially explained to exist due to the formation of a bosonic insulator phase. As the system is conventionally assumed to be 3D the peak was called anomalous as such Bosonic insulator excitations are typical for low dimensional (i.e. 1D and 2D) systems only. The formation of this so-called anomalous bosonic insulator was ascribed to be due to confinement effects thanks to the granular nature of the system. The resistance upturn was phenomenologically explained as a result of normal state electrons being removed from the conduction channels as they pair,

forming phase-locked bosonic droplets within the grains, as the temperature is decreased the bosonic islands grow and eventually couple between grains, resulting in the global phase coherence and a fully superconducting state. This explanation is dependent on a two-step process involving normal electron conduction separated in temperature from the global phase coherence and coupling (intergrain) tunnelling. This concept however lacks any theoretical backing and analysis was based purely on the authors own empirical model and thus does not yield any additional information especially regarding the nature and properties of such a bosonic insulator phase. To date the boron doped superconducting system has been analysed in terms of 3D quantum transport, the aim of this body of work is to investigate the possibility of a 2D phase.

Superconductivity in reduced dimensions are well known to exhibit interesting physics [44], in particular superconductivity in 2D has been investigated with regard to non-trivial topological ordering due to spontaneous time reversal symmetry breaking [45]. Such non-trivial topological superconductors are generally described in terms of odd-parity and spinless wavefunction [46] and have been observed experimentally only in a handful of materials [47]. Since topologically protected states are expected to be useful for decoherence robust qubits [48], much research is directed at identifying potential materials offering such exotic low dimensional phases. Low dimensional effects of superconductivity have generated a large amount of interest. This is due to the interesting physics that accompany the condensation of Cooper-pairs in two dimensions (2D). The field experienced rapid development with both the theoretical backing and experimental investigation into the quantum critical phase transition that occur due to the increased interaction of fermions. One of the first realizations of 2D superconducting planes was within the high temperature cuprate superconductors. This was thanks to the crystalline structure of such materials, where conduction typically occurs within crystal planes with weak coupling between planes. Superconductivity in 2D is predicted to allow for the formation of rare and interesting quasiparticle excitations.

In this work the superconducting nanocrystalline boron-doped diamond is investigated with respect to 2D transport. Firstly the fluctuation spectroscopy is of the paraconductivty is analysed within the Azlamazov-Larkin and LVV models. Secondly the field induced superconductor-insulator transition in looked at, here the magnetoresistance is related to the theoretical predictions of M. Fisher regarding Bosonic metal\insulator formation on the insulating side of the transition. Thirdly one of the most tricking features of the 2D phase, the BKT transition is observed, thus indicating a possible phase of topological significance.

Table 1. The analysis presented in this work has been conducted on data generated from four boron-doped superconducting diamond films of differing grain size. In the table below the thermodynamic properties such as critical temperature, critical field, critical current, superconducting energy gap and grain size is listed.

Sample	T_c (K)	B_c (T)	I_c (μA)	Δ (meV)	D (nm)
B1	3.6	2.5	>800	0.56	100
B2.5	1.2	0.9	25	0.18	60
B4	1.8	1.0	40	0.27	70
B5	2.0	1.1	20	0.30	30

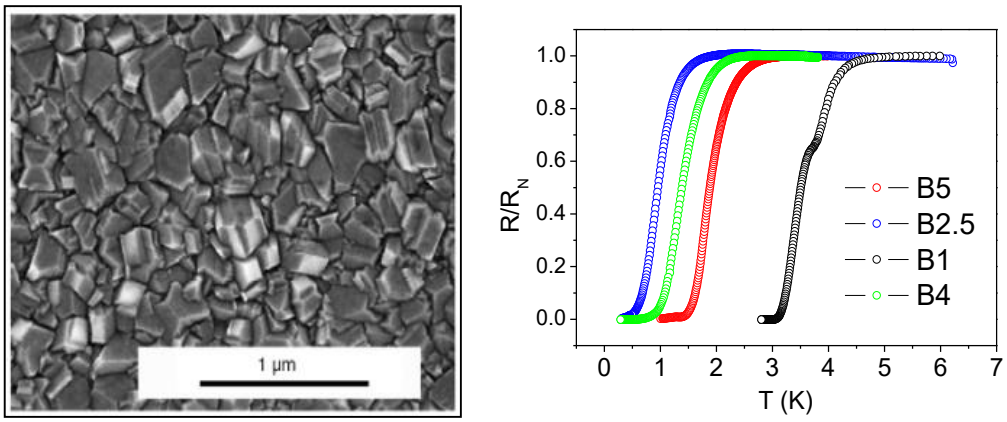

Figure 8. (a) the surface of one of the boron doped samples, the average grain size is determined from SEM imaging. (b) The temperature dependent resistance of the films show a strong grain size dependence.

The samples investigated in this work were synthesised using microwave plasma enhanced Chemical vapour deposition (MPCVD). The diamond samples were grown in a gas mixture composed of 2.5%, 4% and 5% CH_4 in H_2 (therefore named B2.5, B4 and B5). The boron precursor (trimethylborane) was kept constant through the synthesis of the respective films, leading to an estimated concentration of ~4000 ppm in all three samples. Scanning electron microscopy (SEM) has been used to study the morphology of the as grown films. As seen in figure 8 (a) the boron doped samples have a granular surface morphology with grain sizes that vary from 30 nm for sample B5 and 100 nm for sample B1. Resistance measurements were conducted in a four-probe van der Pauw configuration on un-patterned films. Transport measurements were carried out using a closed system cryostat (cryogenic) capable of reaching 300 mK. The temperature stability was better than 10% at 300 mK. Table I gives a comparison of the critical temperature, critical field, critical current, superconducting energy gap and grain size is listed of the three samples grown under different conditions.

Chapter 2

Signatures of 2D transport

2.1 Fluctuation spectroscopy

The study of fluctuation phenomena in superconductors near the superconducting transition has been and still is a subject that has enjoyed a great amount of attention due to its practical and fundamental importance. The theoretical models developed to explain the fluctuation effects were experimentally verified soon after their development through the observation of one of the fluctuation effects, namely the excess conductivity (or paraconductivity). Since then, superconducting fluctuations in various systems have been widely studied leading to a variety of fluctuation effects being discovered. This field of research became vitally important in analysing thermodynamic properties of the cuprate oxide superconductors (high-temperature superconductors, HTS) due to the fluctuation spectroscopies sensitivity to the extremely short coherence length and low effective dimensionality of such electron systems [48]. Additionally some of the anomalous properties observed in the normal state of such high T_C superconductors were theoretically determined to be a result of the strong fluctuations in these systems. The superconducting fluctuations were initially studied within the framework of the phenomenological Ginzburg–Landau theory and then later to a more extensive degree within the diagrammatic perturbation approach giving a clear microscopic theory [49]. Using perturbative theory the superconducting fluctuations along with other quantum corrections such as the weak localization effect became invaluable for investigations of complex systems such as cuprate superconductors, disordered electron systems, granular materials, Josephson Junctions arrays and super-lattices structures [50]. The theoretical models describing the superconducting fluctuations were easily tested experimentally, this was because such models accurately described the strong temperature and magnetic field dependence of such fluctuations near the phase transition. Essentially this allowed for the separation of fluctuation effects from other contributions to the excess conductivity thus yielding information about the microscopic parameters of the materials of interest. The superconducting fluctuations are sensitive to relaxation scattering processes, specifically ones which lead to phase decoherence, and this

ensures that fluctuation spectroscopy is a versatile tool for the characterization of any new superconducting system.

The fluctuation spectroscopy models developed for identifying the dimensionality of superconductors have been extensively used in both single crystal and polycrystalline materials [51,52], proving to be invaluable in helping to classify materials, so much so that this area of analysis is sometimes referred to as 'fluctuoscopy'[53]. Superconducting fluctuations are generally described in terms of three main contributions:

- Aslamazov-Larkin (AL) process.
- Anomalous Maki-Thompson (MT) process.
- Density of States (DoS) term.

The fluctuation spectroscopy was initially developed by Azlamazov and Larkin to explain how the formation of finite lifetime Cooper pair excitations above, but near to, the mean field critical point contribute to the excess conductivity in zero applied field. The model allowed for the determination of the dimensionality of the transport channels in a range of superconducting materials based on the temperature dependence of critical exponents of various thermodynamic properties [55-57]. The AL contribution is given by diagram 1 in figure 9. Soon after the seminal work by Azlamazov and Larkin, Maki and Thomson extended the model by introducing the effects of electron scattering off of the fluctuations for dirty superconducting systems, this lead to the identification of a diverging term known as the anomalous Maki-Thomson correction [58]. This term is analogous to the coherent backscattering of normal electrons observed in dirty metals known as weak localization. The AL and MT processes result in appearance of positive and singular contribution to conductivity on approaching the critical point. The final term (DOS) is due the changes in the single-particle density of state as the electrons form Cooper pairs, this results in a decrease of the Drude conductivity as there is now a lack of single-particle excitations at the Fermi level [59].

This DOS contribution is less singular in temperature than both the AL and MT contributions and is significant only when the AL and MT processes are suppressed (as in the case of inter-layer transport in layered superconductors) or at temperatures much higher than the mean field critical point.

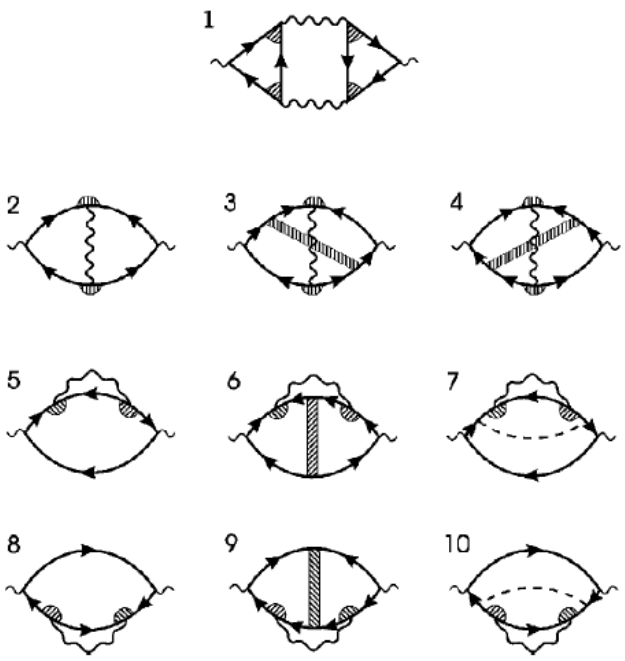

Figure 9. Using diagrammatic perturbation the various contributions to the conductivity are shown, these are a result of the impurity averaging diagrams contributing to the mixed phase paraconductivity in the first order (one loop) approximation. It should be noted that experimental results are generally only described through the AL term as temperatures approach the mean field critical point. Figure obtained from reference [49]

2.2 Fluctuation spectroscopy of granular superconductors

More recently the effects of granularity on the dimensionality of the transport channels has been suggested [60]. The granularity allows for charging and additional scattering effects and offers a suitable system for studies of the interplay of electron correlations and mesoscopic disorder. The granularity is often a parameter than be controlled through the various synthesis techniques and thus offers a test bed for the various theoretical models developed around granularity in transport. The effects of granularity are usually expected be most significant at temperatures below the intergranular single electron tunnel rate. This is not surprising as granular media are predicted to host novel and subtle quantum interference effects including additional modifications to the weak localization correction to conductivity [61]. Lerner, Varlamov and Vinokur (LVV) suggested a characteristic scaling scheme for granular

superconductors which is based on the evolution of the temperature dependent Ginzburg-Landua coherence length driven by inter and intra-grain coupling [60].

This generalized model predicted that granular superconducting media would follow a series of dimensionality crossovers starting from a 3D regime within the grain to a quasi-0D regime where the coherence length is comparable to the grain size and finally a 3D regime as the coherence length increases beyond the grain size and Josephson coupling between grains occurs. The basis of this model is essentially on the dominance of tunnelling, either between grains (intergrain coupling) or restricted within the grain (intragrain). This means that a generic and characteristic feature of granular superconductors would be the appearance of two different scales for the superconducting coherence length, $\xi_g = (D/T_C)^{1/2}$ and $\xi_T = (\Gamma a^2/T_C)^{1/2}$, corresponding to either intra or inter-grain transport regimes respectively. In terms of the reduced temperature, the crossover from the q-0D to 3D regime occurs at $\sim\varepsilon_t = {}^{\Gamma}/_{k_B T_C}$, where Γ is the tunnelling energy. The second dimensional crossover would take place at $\sim\varepsilon_g = {}^{E_T}/_{k_B T_C}$, where E_T is the Thouless energy which equals $E_T = {}^{\hbar D}/_{a^2}$, and D is the diffusion constant and a the lattice constant.

Accordingly, the excess conductivity is expected to show an increase in approaching the T_c signifying the q-0D regime, then decrease steeply after reaching the 3D regime, this is essentially due competition between the suppression of single electron tunnelling and coherent charge transfer of Cooper pairs. This upward trend in the resistance is was determined to be sensitive to weak magnetic fields and is thus a novel Maki-Thompson-type mechanism. This model has recently been applied to superconducting boron doped diamond [63] and although the predicted upturn in resistance was not reported there, the dimensionally crossover in the temperature dependent critical exponents of the fluctuation conductivity predicted by the model was indeed observed [63].

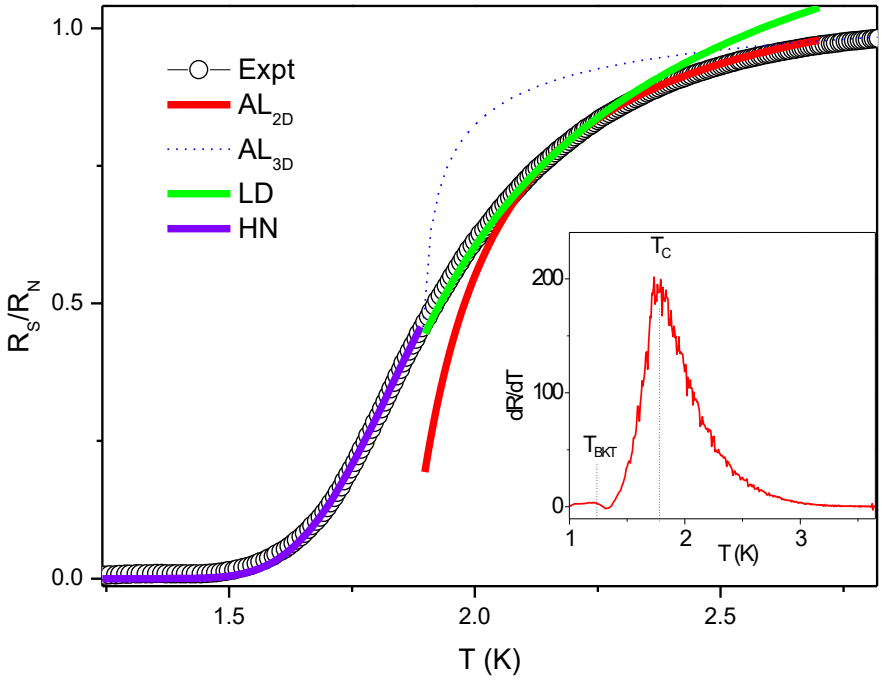

Figure 10 The temperature dependent resistance normalized with respect to the resistance above 4K, the dotted line is an indication 3D AL, a more close fit is observed when using the 2D model as indicated by the red line. The green line represents the Lawerence-Doniach formula which takes into account the crossover between 2D and 3D transport regime, as can be seen this formula fits the data over the largest temperature range when compared to the purely 2D or 3D case. The inset shows the temperature dependent first derivative of the resistance with respect to the temperature as a function of temperature. The temperature at the peak is used as the mean field critical point in the fittings shown in the main panel. Also shown in figure 10 is the Halperin-Nelson formula related to the curvature below the mean field critical temperature and the Berezinskii-Kosterlitz-Thouless transition which will be discussed in a subsequent section.

In this work we investigate more deeply the excess conductivity region between the q-0D and 3D transition and show through the application of both the AL and LVV models that the smoothness of the superconducting transition is due to a small yet distinct temperature range where the fluctuation conductivity follows the theory predicted for 2D transport. As shown in figure 10, the superconducting transition (here normalized with respect to the normal state resistance) of the diamond films shows a broad smooth transition instead of a sharp downturn to the superconducting state. This is typically observed in superconducting materials that show

dimensional transport channel crossover. In order to investigate the nature of such dimensionality crossover the AL equations are firstly used to fit the data, as mentioned before this model has been successfully used for a number of materials including both thin films and bulk crystals which have 2D character [64,65]. In this scheme the correction to the fluctuation induced conductivity can be represented in 2D as well as 3D according to:

$$\Delta\sigma_{2D} = \frac{e^2}{16\hbar d}\frac{T}{T-T_C} \qquad (5)$$

$$\Delta\sigma_{3D} = \frac{e^2}{32\hbar\xi(0)}\left(\frac{T}{T-T_C}\right)^{1/2} \qquad (6)$$

Or in a more compact and generalized form as:

$$\Delta\sigma = A\varepsilon^{-\lambda} \qquad (7)$$

Where A is a coefficient taking on the respective values for 2D or 3D depending on the coherence length or interlayer spacing (d) as given in equations 1 and 2 . ε is the reduced temperature $(T - T_C)/T$. As shown in the inset of figure 10, the mean field critical point is determined from the first derivative of the resistance with respect to temperature. The exponent λ is dependent on the dimensionality of the transport and takes on values of -1.0 and -0.5 for 2D and 3D respectively. Shown in figure 10 is the application of the AL equations. For a direct comparison both the 2D AL (red line) and 3D AL (dotted line) equations have been fit to the data. As can be seen the 3D equation does not fit the data set particularly well especially near the superconducting transition temperature, whereas the 2D fit correctly follows the curvature of the resistance to some extent but deviates from the experimental data approaching the mean field critical point. This clearly demonstrates that although there is a significant 2D component to the fluctuation spectroscopy a crossover in the dimensionality does occur. In order to further demonstrate this crossover an additional fitting with the Lawrence-Doniach (LD) model [66] is applied to the data, indicated by the green line in figure 10. The LD model was develop to take into account the change from a 2D to 3D character as the coherence length extends beyond

the ab plane into the c-axis due to Josephson coupling between 2D planes observed in the cuprate superconductors. This model is given by:

$$\Delta\sigma = \frac{e^2}{16\hbar d}\varepsilon^{-1}[1 + (\frac{2\xi(0)}{d})^2]^{-1/2} \qquad (8)$$

Where, as before, $\xi(0)$ is the coherence length and d is the intergrain separation. As can be seen in figure 10 the LD model does indeed fit the data to a better extent than the purely 2D or 3D Al equations, verifying the dimensionality crossover and highlighting that the superconducting diamond transport properties behave more like the high temperature cuprates than the conventional s-wave superconductors. To verify the various transport dimensionalities within the fluctuation conductivity regimes the excess conductivity is plotted as a function of the reduced temperature, as is the convention, for a number of sample having different grain sizes, as shown in figure 11 (a-c). The crossover from the quasi-0D to 3D regime with critical exponent of $\lambda = 3$ (previously observed [64]) is clearly interrupted by a smooth conductivity region that follows the critical exponent of $\lambda = 1$ as predicted by the AL model. This 2D region is further more believed to be significant as it occurs across of temperature range of up of 300 mK and was found to be strongly dependent on the grain size. As shown in the inset of Fig 10 (c), the decrease in the 2D phase temperature range with an increase in the grain size can be identified, indicating that the smaller grain size is more closely related to the 2D phase as can be intuitively expected. Interestingly this is the same trend exhibited by the grain size dependent Thouless energy [63] and indicates that in smaller grain size samples electron correlations are more significant.

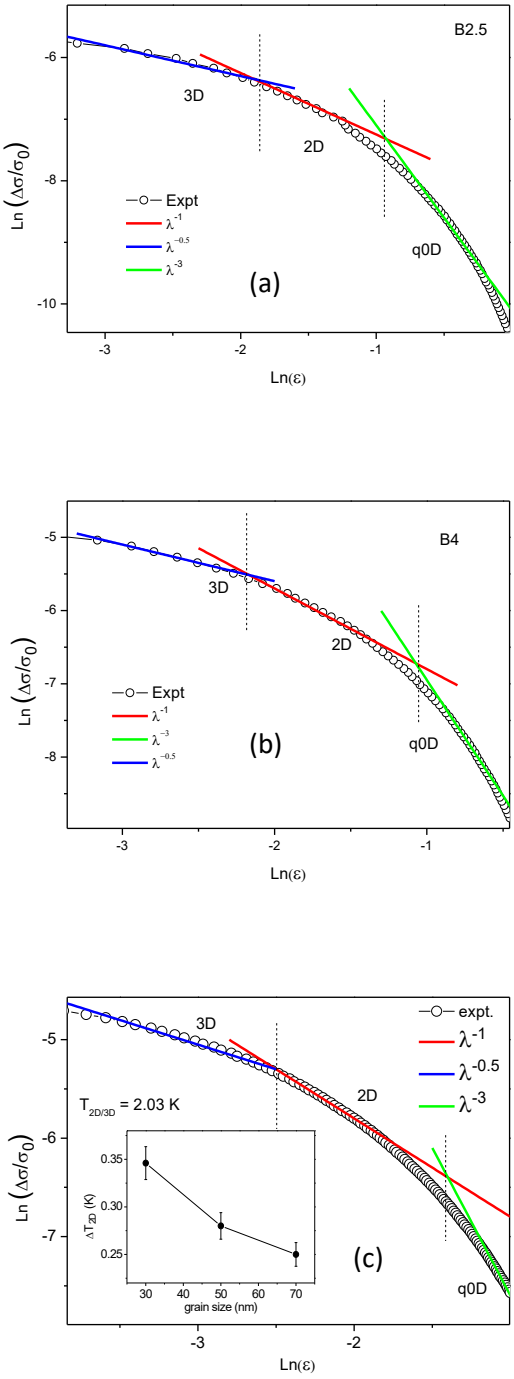

Figure 11. (a) The fluctuation conductivity as a function of the reduced temperature previously defined for three samples. (b) The quasi-0D region (indicated by the green line) to 3D (blue line) transition is clearly interrupted by a conductivity that follows the expected temperature dependence of a 2D phase. The temperature range of this 2D is found to be grain size dependent and as shown in the inset of figure 11(c), the smaller grain sized samples has a longer temperature range of occurrence.

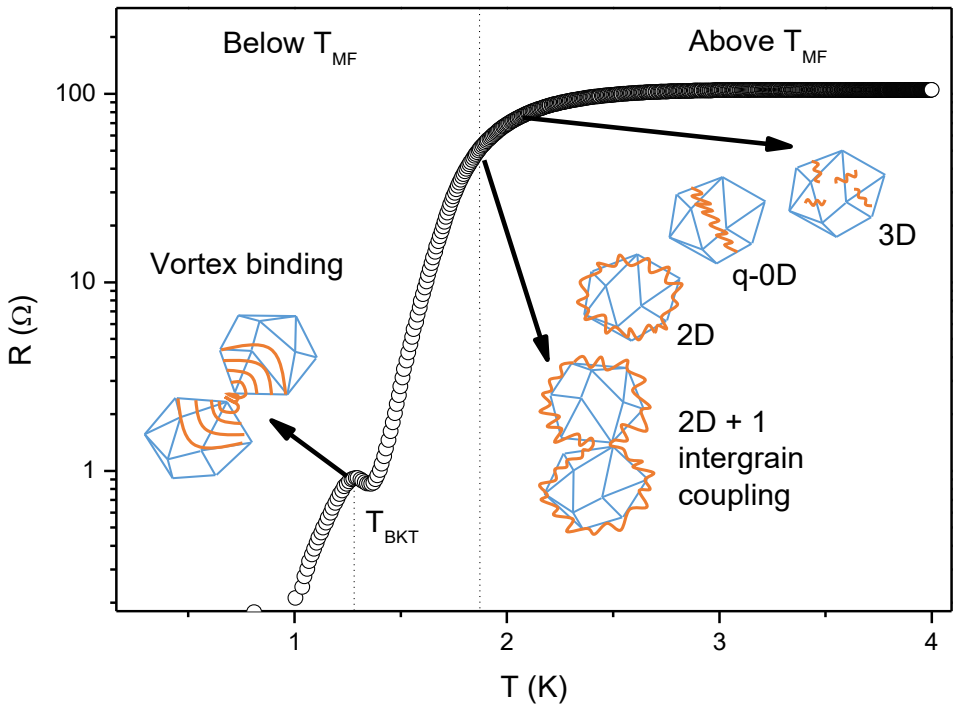

Figure 12. The temperature dependent resistance in log scale. Indicated by the dotted lines are the mean field critical temperature and BKT temperatures. The fluctuation spectroscopy regime occurs at temperatures directly above the Tc. In this regime the dimensionality crossovers discussed above are shown schematically.

The analysis presented in this chapter follows a combination of the Azlomozov-Larkin and LVV theories developed for various superconducting systems. As indicated in figure 9 and 10, the models are in good agreement with the experimental data. Although the LVV model has before been fit to the fluctuation conductivity of superconducting boron doped diamond, this model was developed specifically for granular superconducting media and does not take into account any two-dimensionality. Here we have presented a distinct temperature range that falls between the quasi-0D and 3D region that follows the expected temperature dependence for a 2D material. In order to make sense of this analysis we rely on a comparison between the granular diamond and cuprate (layered) superconductors. The superconducting diamond film is composed out of nanocrystalline diamond grain separated by a thin (low dimensional) boron rich layer. According to the LVV and 2D AL models the evolution of the coherence length is thus expected to influence the dimensionality of the transport in the following way: At

temperatures above the mean field critical point, fluctuations occur, in this higher temperature range the cooper pairs are short lived and have a coherence length much shorter than the grain diameter, the conductivity thus follows a 3D as the fluctuations can occur in all spatial dimension within the grain. At lower temperatures the coherence length increases as the fluctuations become more stable, this occurs until the coherence length is comparable to the grain size, this region is the quasi-0D regime predicted in the LVV model. Up to this point the transport is dominated by intragrain processes. Our analysis indicates that upon further decrease in temperature, but before intergrain tunnelling becomes significant, a 2D phase is realized. This intuitively can occur if we introduce a topological phase where the fluctuations are larger than the grain size, (i.e. beyond the q-0D regime) but however are restricted to the surface of the grains. When cooling the system further, the single particle tunnel energy will be reached, beyond this temperature electrons are able to move between grains and Josephson Coupling occurs, this final stage is the final 3D phase predicted by the LD an LVV models and can actually be thought of as a 2D + 1 phase. The realization of 2D phase is quite significant as superconducting systems in 2D are known to exhibit a range of novel and exotic features ranging from bosonic excitations to topological non-trivial phases. The analysis presented above is in line with what has been reported on for the cuprate superconductors where the 2D phase which occurs within the ab plan of such materials is known to exhibit non-s-wave order parameter with respect to the orbital pairing. In such systems the order parameter is known to be of the d-wave pairing due to the anisotropic nature of the materials. It is shown here that the diamond films follow this behaviour quite strongly indicating that there is a strong possibility of non-s-wave behaviour. Additionally, this work raises additionally questions regarding the nature of the 2D phase. Currently there is a large amount of research directed at the investigation of topological non-trivial surface states. This is primarily for the field of quantum information processing as qubits developed using such materials are expected to yield fault tolerant logic operations due to the topologically protected surface states. This raises the question as to the nature of the 2D surface state identified in superconducting diamond, additional studies on the microstructure, particularly the low dimensional intergranular boron phase will need to be conducted to establish non-triviality.

Chapter 3

Field induced superconductor-insulator-transition

3.1 Superconductivity and duality

The physics of superconductivity in confined two dimensional space has attracted a great deal of research interest. In such system the reduced dimensionality is expected to result in a range of exotic phases or excitations [67]. One such theory that has enjoyed a great deal of success thanks to experimental verification is that of quantum dual phases [68]. In order to study duality phenomena both the disorder and field induced superconductor-to-insulator transitions have been used [69,70]. In such experiments the superconducting state is driven to an insulating phase by controlling the disorder of the system, either through films thickness, doping concentration , level of structural disorder, or by systematically applying a magnetic field.

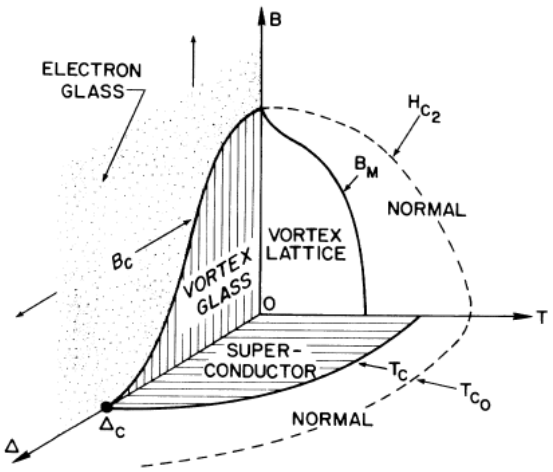

Figure 13. A phase diagram for the critical disorder and field induced SIT. In two dimensions' superconductors have been theoretically and experimentally shown to exhibit unconventional phases changes to an insulating state through either the application of a magnetic field or through tuning the disorder of the system. In disordered superconductors this insulating phase is known as the electron-glass or charge-glass state that is formed from localized cooper pairs that interact through a repulsive Coulomb interaction. Diagram taken from reference [67].

One of the leading theories for explaining the SIT in disordered materials is that of the charge-vortex duality [67]. In this model when the system is in the superconducting phase Cooper pairs are condensed into a superfluid leading to a decrease in resistance whereas bosonic excitations in the form of vortices are delocalized and lead to a finite resistance. On the insulating side of this transition the Cooper pairs become localized, leading to a rise in resistance and the vortex states condense into a macroscopic state of zero conductivity. The charge-vortex duality has been applied to arrange of different systems including Josephson junction arrays. In this system the insulating state is a result of a Coulomb blockade or repulsion between superconducting regions analogous to granular material. The model derived by M.P. Fisher [67] predicts a universal scaling behaviour of the resistance as a function of applied magnetic field. Also predicted by the model are universal values of longitudinal and transverse resistivity's predicted to have a value of $h/4e$ at the SIT, these universal values are however difficult to verify except in well-defined patterned structures [71]. One of the consequences of this duality is the dual Berezinskii-Kosterlitz-Thouless transition called the charge-BKT transition [72]. This occurs on the insulating phase where the vortices which are bound during the superconducting phase unbind and form the electron-glass quantum phase. The charge-BKT effect has found widespread success in the analysis of Josephson Junction arrays where the insulating state was determined to result from Coulomb forces acquire a 2D character (i.e. act logarithmically) and result in the so called superinsulating phase [73]. This superinsulating phase is nothing more than localized Cooper pairs. Such studies have for obvious reasons been of great value in development of quantum technologies as size and charging effects are can be greatly beneficial for quantum technology development [74].

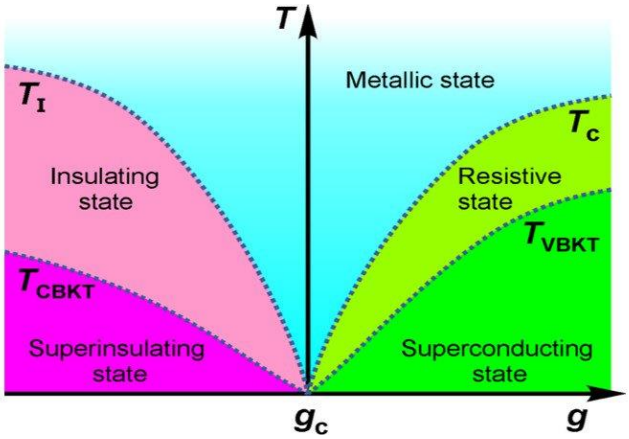

Figure 14. The BKT transition is a class of transition that can have dual phases including a dual charge-BKT analogue involving the binding of charge and anticharge. Diagram from reference [73].

3.2 Signatures of the charge-glass state

As shown in figure 15 (a & b) the application of a magnetic field has effect of initially lowering the critical temperature, until driving the system to a non-superconducting state identified by the reduced downward slope of the transitions and finally a seemingly temperature independent phase (at approximately 3 T for the sample shown in figure 15) with saturating resistance equal to the normal state resistance. According the Ginzburg-Landua pair breaking theory the coherence length can be determined from the field dependent resistance isotherms. This is shown in figure 16 (a) where the temperature dependence of the critical field (B_{C2}) is shown with a fitting to the well-known relationship:

$$B_{C2} = \frac{\varphi_0}{(2\pi\xi_{GL}^2)}(1 - \frac{T}{T_C}) \qquad (9)$$

The values of the critical magnetic field are derived from the temperature dependent resistance at fixed field (figure 15(a)), and for the particular sample shown here gives a Ginzburg-Landua coherence length of approximately 10 nm, which is smaller than the estimated grain size of 30 nm. As this value is dependent on the application of field it demonstrates that the Cooper pairs are confined to within the grains, this can be related to the previous chapter where based on the AL theories for granular materials it was determined that applying a magnetic field leads to decoupling of the grains (i.e. confining superconducting Cooper pairs to the grains). This result indicates that applying the magnetic field acts in a way to localize the cooper pairs, this is an essential ingredient for the formation of the electron glass phase where the cooper pairs act as localized charged bosonic excitations. More information about the effect of the applied magnetic field can be extracted when representing the temperature resistance data in logarithmic scale as a function of inverse temperature as shown in figure 15 (b). As shown there, when no field is applied, the system follows an activated Arrhenius type downward trend interrupted by a re-entrant peak (determined to be an indication the BKT transition and will be thoroughly analysed in the next chapter) and then condenses to the superconducting state. When the field is increased to 0.25 T the trend still follows the activated transport associated with the proliferation of vortices as they are unbound, with the applied field however the BKT transition is not again observed, as is generally expected, and instead appears to approach a saturation in the resistance but eventually reaches the superconducting phase. At higher fields the system is even more interesting, as the field is strengthened, the activated region is terminated by a temperature independent phase with an onset temperature that decreases with larger fields.

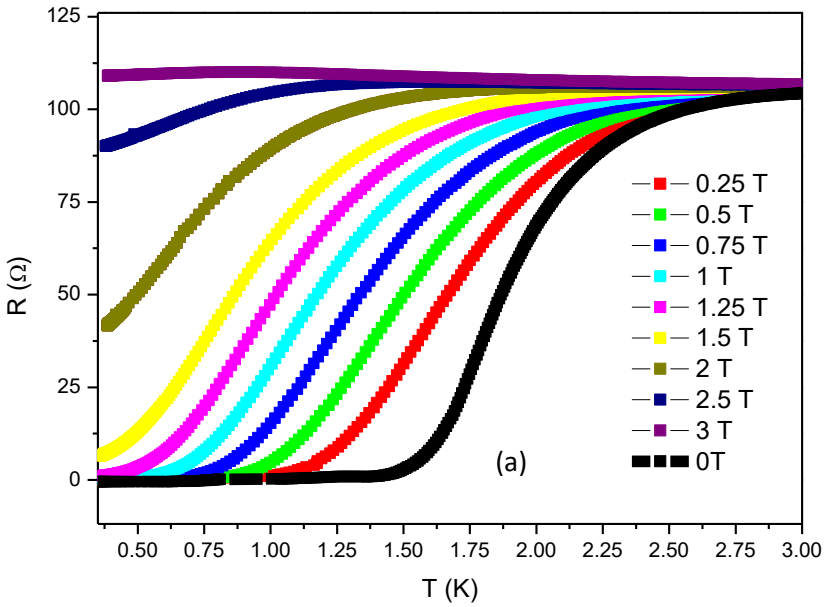

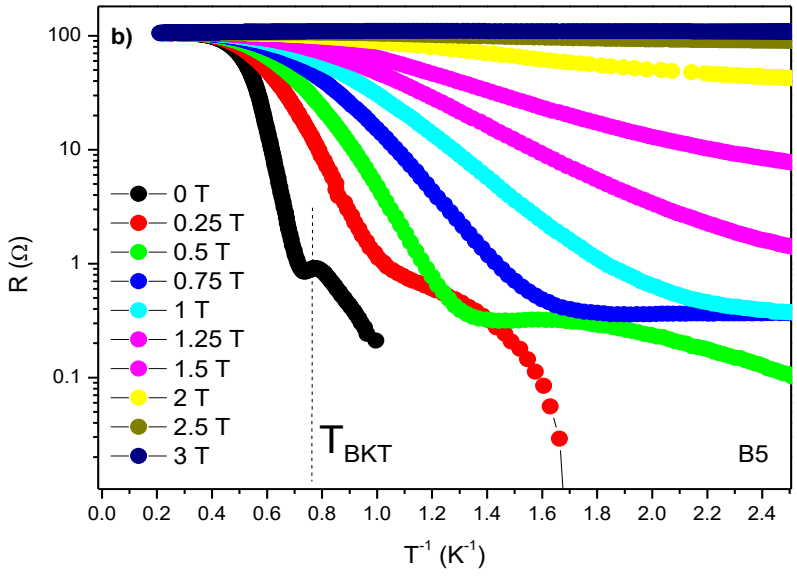

Figure 15 (a) Although the field induced superconductor to insulator transition has been investigated in boron doped diamond, as the system is generally assumed to be a strictly 3D material, as shown here the application of magnetic field supresses the critical temperature until breaking the superconducting phase. Figure 15 (b) More information can be extracted from the same temperature dependent data when represented on a logarithmic scale with respect to the inverse temperature. As can be seen the superconducting transition follows an Arrhenius type down turn which crosses over to a temperature independent phase at higher fields.

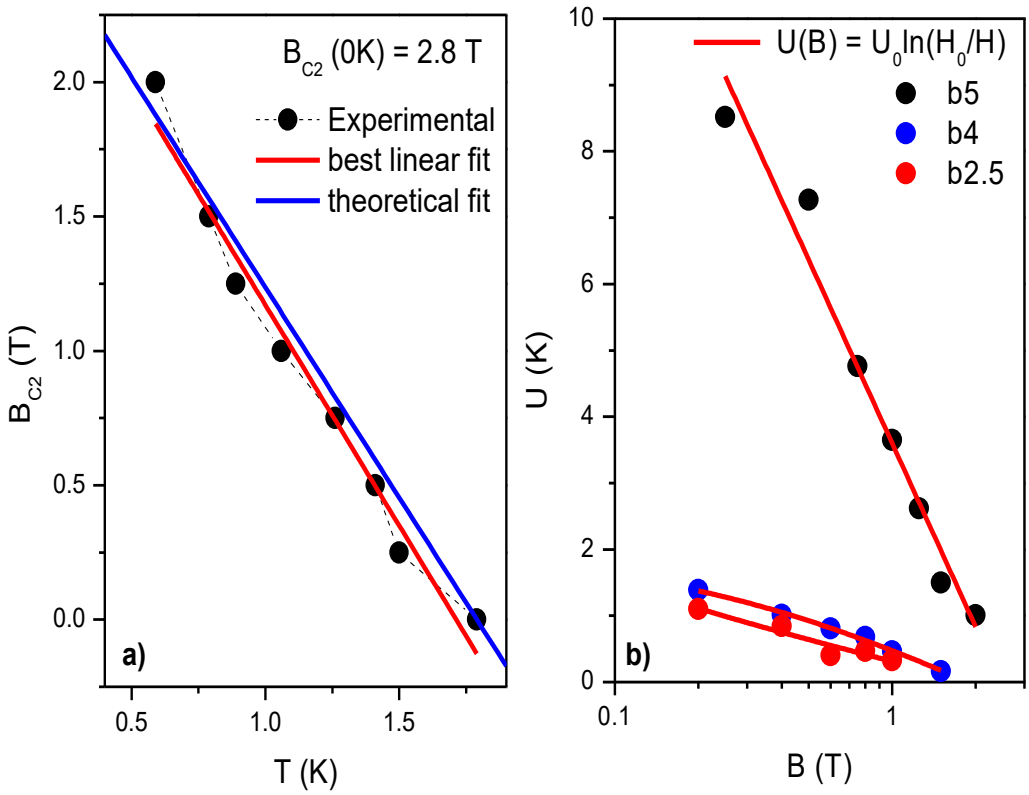

Figure 16 (a). Using the Ginzburg-Landua pair breaking theory it is possible to derive the coherence length, determined from the straight line fit to the experimental data. We find a zero field coherence length of 10 nm for the sample represented here. Figure 16 (b) For the activated region shown in figure 15 (b) it is possible to determine the vortex binding energy, here shown as a function of the applied field. As expected increasing field strength weakens the vortex-antivortex binding energy.

The formation of the temperature independent phase is quite significant and can be related back to the field induced superconductor insulator phase transition depicted in figure 15. At these fields the system has essentially been driven to the glassy phase, this is also sometimes explained as quantum metal phase or the quantum macroscopic tunnelling of vortices (QMTV), where the finite resistance is a result of unbound vortex dynamics. This quantum phase is a precursor to the electron-glass phase. Figure 16 (b) shows the field dependence of the vortex pairing energy for at least three samples with different grain size.

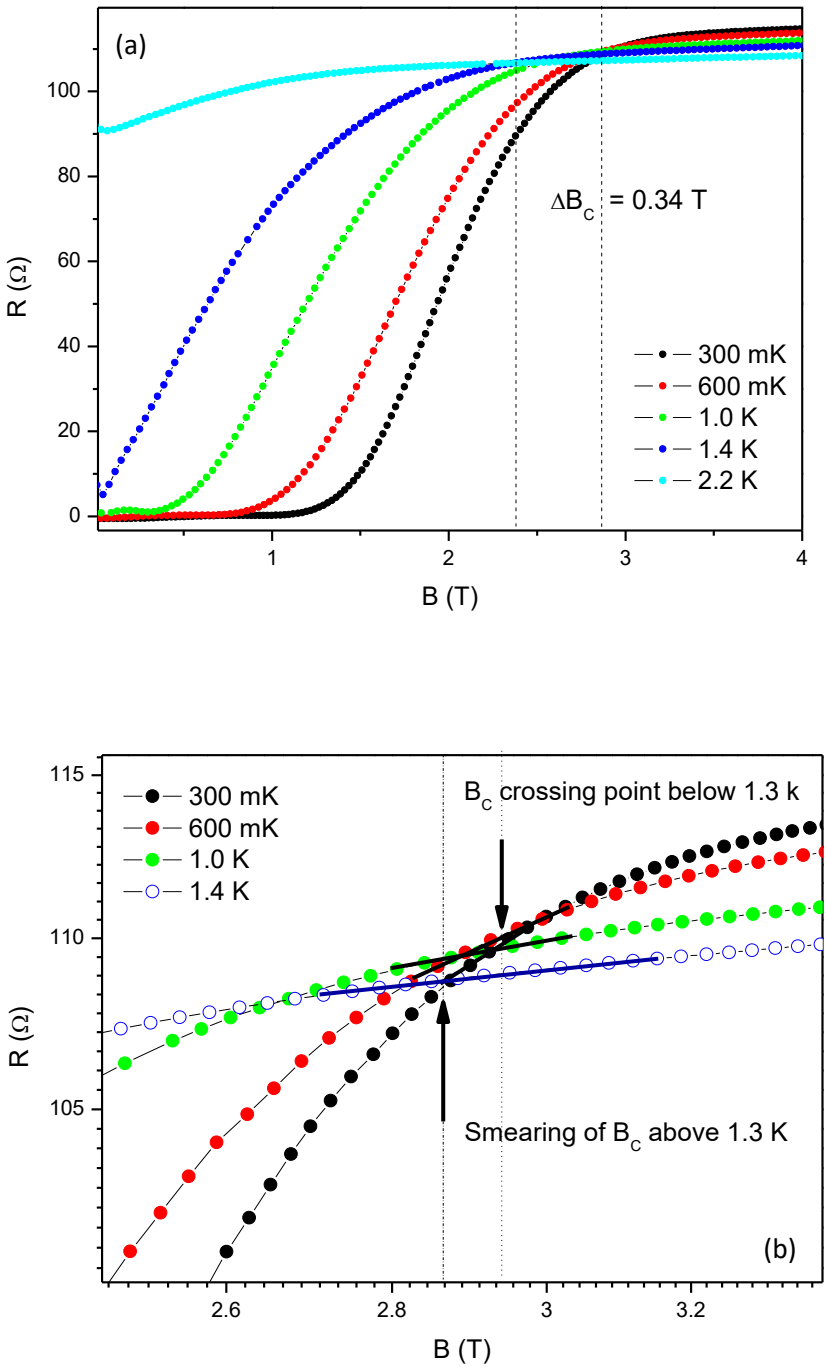

Figure 17 (a) The magnetoresistance at different temperatures starting from 300 mK, i.e. far below the critical point. As shown here there is a distinct critical field region where the isotherms cross, this is one of the indications of a critical field signifying a critical quantum point or phase transition. Figure 17 (b) A closer look at the crossing point reveals that near this critical point the isotherms follow a power law behaviour, this is one of the predictions for the charge-vortex duality.

The sample B5, having the smallest grain size (~ 30 nm) shows an appreciably higher vortex pairing energy, again this can be attributed to the confinement of excitations within the grains, from the fit the critical field can be extracted, for sample B5 this was determined to be 2.46 T and is 0.34 T smaller than that obtained from the Ginzburg-Landau fitting shown in figure 14 (a), this discrepancy is most likely related to the respective models used, in the activated Arrhenius fitting the coherence length is related to the proliferation of vortices and their respective dynamics whereas the GL theory is related to the Cooper pair coherence length, and is an indication of the mixed phase of excitations, either Cooper pairs or vortex states at these intermediate fields.

When the strength of the applied field is increased to approximately 3 T or beyond the system is driven to the insulating state. Fortunately the theoretical model developed for the identification of the electron-glass state can easily be compared to experimental data. This has already be used for the verification of this phase in various materials but most notably in MoGe [75] and InO [76] thin films. According to this model [67] the critical exponents Z_B and V_B follow a specific scaling function and can be used to characterize the resistance near the transition, i.e.:

$$R[c_0(B - B_c)/T^{1/z_B\nu_B}] \qquad (10)$$

This allows for a convenient representation of the magnetoresistance isotherms that a can be used to test for the occurrence of the electron-glass (insulating) phase:

$$\left(\frac{dR}{dB}\right)|_{B_c} = \left(\frac{h}{4e^2}\right)c_0 T^{-\frac{1}{zv}} R'(0) \qquad (11)$$

In other words by plotting the field dependent differential of the resistance as a function of inverse temperature it is possible to evaluate the product of the critical exponents zv from the slope of the plot. This analysis was performed on two samples, B5 and B2.5 which have grain size of 30 to 70 nm respectively and span the range of the samples used. This analysis is shown in the inset of figure 16. As seen there the critical exponent product of both samples fall within the experimental range of unity as expected for the electron-glass phase. Once the critical exponent product and the critical field are known it is possible to use the scaling form of R to test the validity of the electron-glass phase using only experimental fitting parameters. This is achieved by plotting $R(T,B)$ against the absolute value of the scaling variable $(B - B_C)/T^{1/zv}$. This is shown in the main panel of figure 15, where the resistance for the two samples have been normalized to their respective normal state resistance. The scaling is very near universal with the entire range of points falling on the expected

trend. The branches of the scaling behaviour can be dived into two regions, above the critical field and below. The region below the critical field indicates that only at the lowest temperatures (i.e. 300 mK) do the samples deviate most strongly with the universal behaviour, this is possibly an indication of an additional phase at low temperatures. In the region above the critical field the low upward bend of the curve is unlike the bulk superconducting samples analysed in this manner and has been observed before in MoGe samples [75]. The reason for this was given as evidence of electrons in the normal state that tunnel and contribute to the conductance instead of being entirely bound in coop pairs and localized. This is quite plausible in our system as mentioned in the previous section granular samples have additional phenomena due to the intergrain coupling and tunnelling. Essentially the localization of charge carriers within the grain is reduced as temperature increases and thus the insulating state is not as severe. It has also been shown that the breakdown of the universal scaling can occur due to finite size effects and the formation of Josephson networks at certain grain size [77]. Nevertheless the scaling behaviour here results in critical exponent products of $z\upsilon = 1.024 \pm 0.3$ and $z\upsilon = 1.028 \pm 0.2$ for samples B5 and B2.5 respectively. These values are well within the theoretical prediction of unity for a two dimensional system and are confirmed by the best fit to the dR/dB isotherm data taken at the critical field B_C (figure 18, inset). These observations are a good indication that this system may very well exhibit the charge glass state above the H-SIT as predicted for disordered 2D superconductors.

This signifies the importance of low dimensional effects in complex systems such as superconducting diamond, at first glance this system has been assumed typical three dimensional material [42], however due to granularity and interfacial boron layers it is quite obvious that additional effects, most notable those related to electron tunnelling, charging effects and quantum interference can lead to quantum phase transitions. This is particularly important in the field of quantum technology where phase transitions as well as the excitations of exotic quasiparticles can have serious consequences for the operation of such technologies [78]. The effect of localized Cooper pairs as bosonic excitations as demonstrated here can be of interest for device application. In the granular system, just as in Josephson Junctions the properties are

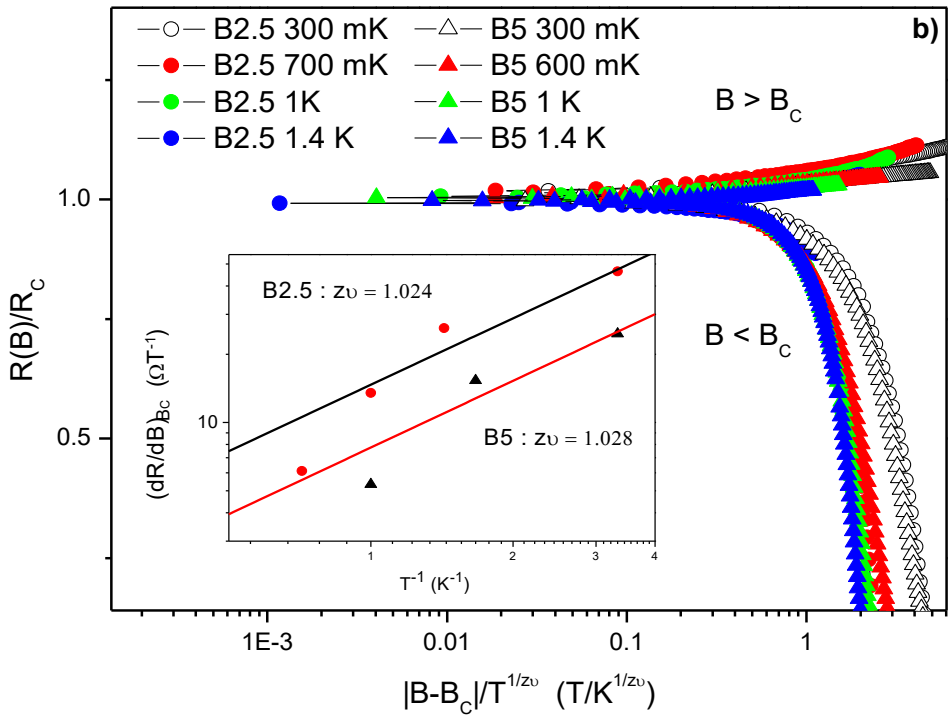

Figure 18 As predicted by the theoretical model, the samples show universal scaling behaviour with critical exponents well within the range expected for the indication of a charge-glass bosonic excitation as shown in the inset, vz are very near to the theoretical value of 1.

controlled through the tunnelling phenomena of the system. In the strongly coupled regime Cooper pairs can tunnel between grains, corresponding to a regime where the Josephson coupling energy between grains is higher than the charging energy of the grains ($E_J > E_C$). However as demonstrated here the realization of the electron glass phase is very heavily dependent on the Coulomb repulsion between charges. In this instance the charging energy exceeds the Josephson coupling ($E_C > E_J$) resulting in this insulating phase. As mentioned before in this insulating phase a charge-BKT transition can occur between these charges leading to the binding of charge and anti-charge pairs, this is due to the 2D (logarithmic) interaction of such charge carriers and leads to the so called superinsulating phase. This superinsulating phase is however not observed in the superconducting diamond in these accessible field range. The hall mark of such a state is the steep upward turn of the temperature dependent resistance below the critical point [79].

Chapter 4

Berezinskii-Kosterlitz-Thouless transition

4.1 Phase transitions without breaking underlying symmetries

The pioneering [80] and now Nobel Prize winning work of Kosterlitz and Thouless (KT) on topological excitations in 2D systems has generated a great deal of interest [81]. Although the transition was first predicted by Berezinskii in his work on superfluid He [82] (hence the B-KT transition), much of the mathematics regarding the physics of this transition was put forth by Kosterlitz and Thouless. The BKT transition describes the metal –superconducting phase transition by invoking the thermal excitation of topological defect pairs called vortex and antivortex. In the metallic or resistive state, the vortices are unbound and proliferate leading to a finite resistance. At the BKT transition temperature the vortices bind into pairs, leading to the divergence of the coherence length. The original idea was conceived using the so called XY-model of a 2D array of spins. Such systems up to the time of KTs discovery had been proven through rigorous theoretical work to not allow phase transitions with long range order on approaching low temperatures [83]. The transition was very early on observed experimentally in a range of systems including 2D crystals [84], thin superconducting films [85] and even ion trapped gasses [86], this provided a great deal of experimental data for the development of a more concrete and refined theory of topological phase transitions that is currently enjoying a great deal of attention. The key feature of the BKT transition is that it occurs due to the unbinding of topological defects that are paired by a logarithmic interactions in 2D thus breaking the long range order as they proliferate without breaking the underlying symmetries of the system. The BKT transition has been identified in a number of thermodynamic transport properties and are is intimately linked to the superfluid stiffness which defines the energy scale related to the areal density of superfluid cooper pairs. This is described as:

$$J_S = \frac{\hbar^2 n_s d_{BKT}}{4m} = \frac{\hbar^2 c^2}{16\pi e^2}\frac{d_{BKT}}{\lambda^2} \qquad (12)$$

Where n_s and m denote the superfluid density and carrier mass respectively, λ is the magnetic penetration depth and d_{BKT} is the effective length scale the system is considered 2D. The possibility of observing the BKT transition is thus linked to low values of the ratio: $\frac{d_{BKT}}{\lambda^2}$. The interaction between vortex pairs remains logarithmic as long as the pearl screening length, $\Lambda_J = 2\frac{\lambda^2}{d_{BKT}}$, is larger than the system size. In conventional superconductors this length scale is determined by the thickness of the film. The BKT transition has also been investigated in a range of bulk superconducting systems that possess 2D crystal planes [65]. This is well established in many of the high T_c superconductors where the crystal lattice is composed of 2D CuO planes (*ab* plane) which are weakly linked in the third spatial dimension (*c*-plane). In such layered systems the presence of other superconducting planes squeezes the field of the pancake vortices into a narrow range along the c-axis. It has been established that Josephson coupling between layers can affect the logarithmic interaction between vortices in the same plane. This is because the pearl screening length causes an upper cut-off to the logarithmic interaction between vortices:

$$\Lambda_J = \xi_0 / \sqrt{J_\perp / J_\parallel}, \qquad (13)$$

Where $J_\parallel$ and $J_\perp$ are the in-plane and out-of-plane superfluid stiffness respectively and ξ_0 is the zero field coherence length. This means that the coupling between the superconducting planes influence the vortex-antivortex interactions. In the limit of weak coupling, $J_\perp / J_\parallel \ll 1$, then the effective pearl screening length will be large enough to allow for the BKT transition, independent of the film thickness (*d*). Because of these finite size effects the BKT transition observed in layered bulk superconductors occurs at temperatures slightly higher than purely 2D case. This has been confirmed in experiments where the number of ab-planes was controlled, thus determining the effective thickness from this analysis to the known thickness of the films [87]. Thus by measuring thermodynamic transport properties it is possible to identify the BKT transition.

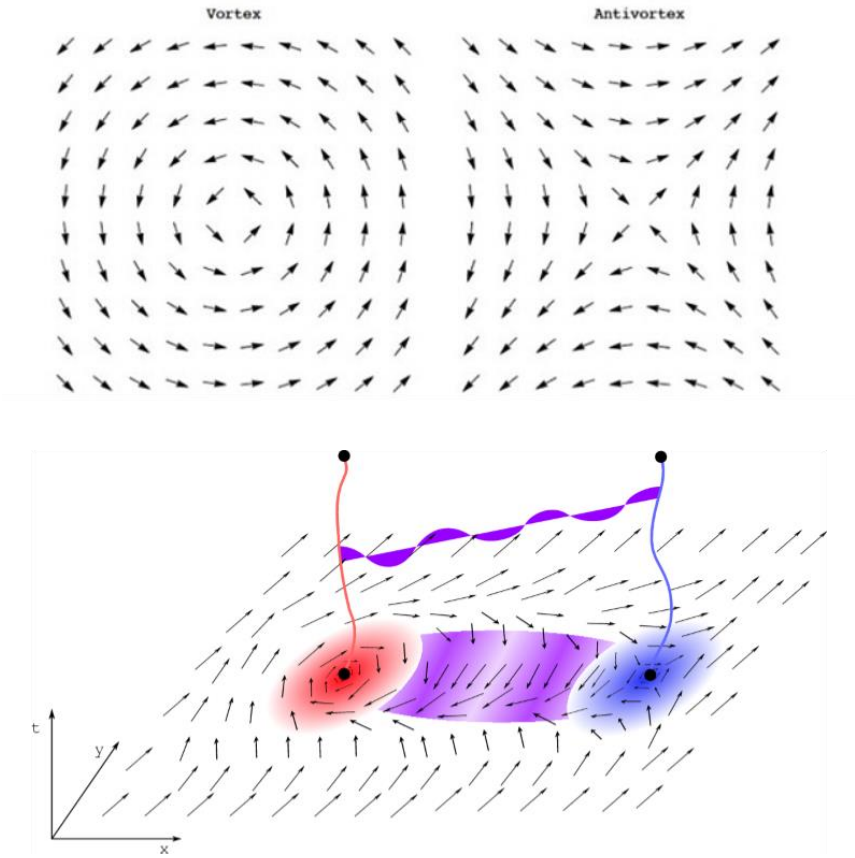

Figure 19. Topological defects (a) vortex and (b) antivortex involved the BKT transition once vortex-antivortex binding occurs (c). The bound state where vortex-antivortex pairs are locked in position and do not contribute to resistance.

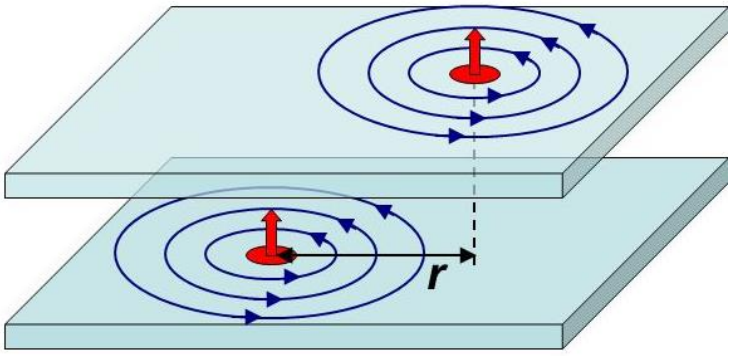

Figure 20. The BKT transition has also been experimentally verified in bulk layered superconducting system. This is due to vortex and antivortex pairing between layers, indicated in the schematic above is a depiction of vortex dynamics between superconducting layers and can lead to new novel phases of vortex-matter.

The theoretical models used to describe the BKT transition are based on the renormalized group equations presented by Kosterlitz and Thouless, these equations describe the large distance behaviour of the dimensionless vortex fugacity (g) and superfluid coupling (K), given by:

$$\frac{dK}{dl} = -K^2 g^2, \qquad (14)$$

$$\frac{dg}{dl} = (2 - K)g, \qquad (15)$$

Where $\Lambda = \ln(r)/\xi$, i.e. the interaction length rescaled with respect to the length cut-off scale of the coherence length. The value of K is determined from the BCS theoretical value at small length scales;

$$K = \frac{\pi J_{BCS}(T)}{T} \qquad (16)$$

And the value at large distances is determined from the presence or absence of vortex excitations which are described by the large scale behaviour of the vortex fugacity:

$$g = 2\pi e^{-\beta\mu} \qquad (17)$$

μ being the vortex core energy and β the Boltzmann temperature. Using these equations the physical superfluid stiffness can be obtained from the numerical solutions of these equations at larger length scales. Using these relations for analysing experimental data one relevant parameter that can be extracted from the fitting is the ratio μ/J_S and can be compared to the theoretical value of the XY-model:

$$\mu_{XY} = \frac{\pi^2}{2} J_S \qquad (18)$$

The value of μ/J_S is related to the temperature scale where vortex behaviour causes significant deviations of J_S from the BCS value.

Although originally thought to only occur in strictly 2D systems, the BKT transition has been observed in a range of quasi-2D materials that are appreciably thicker than the ultra-thin superconducting films the transition is typically reported for. This includes materials such as the Fe-based superconductors [65], layered cuprates [87] and novel systems such as 4A carbon nanotube/zeolite composites [88]. The quasi-2D system is essential one which exhibits a 2D to 3D crossover, usually as a result of Josephson coupling between layers or planes.

This can effectively be discussed within the 3D XY-model:

$$H_{XY} = -\sum_{<ij>} J_{ij} cos(\theta_i - \theta_j), \qquad (19)$$

Where $\theta_{i,j}$ is the superconducting phase on two neighbouring sites (*I* and *j*). The energy scales can thus be related to intra- or inter-plane coupling, in a similar way suggested for the Doniach-Lawrence scaling of the fluctuation spectroscopy mentioned in a previous chapter.

$$J_{ab} = \frac{\hbar^2 d \rho_s^{ab}}{4m} = \frac{\hbar^2 c^2 d}{\lambda_{ab}^2 16\pi e^2}, \qquad (20)$$

$$J_c = \frac{\hbar^2 a \rho_s^c}{4m} = \frac{\hbar^2 c^2 a}{\lambda_c^2 16\pi e^2}, \qquad (21)$$

Where λ_{ab} and λ_c are the in-plane and out of plane penetration depth, respectively. *m* is the electron mass, *a* is the in-plane lattice spacing and *d* the inter-layer distance. The anisotropy of such a quasi-2D systems manifests as a rapid down turn in the superfluid density instead of the sharp universal jump, the downturn has also been reported to be dependent on the vortex core energy. In contrast to the purely 2D XY-model where the vortex core energy is fixed by the in-plane coupling, in quasi-2D systems such as the layered superconductors the vortex core energy takes on values larger than the XY model. The vortex core energy thus provides a useful energy scale which has proven valuable in categorizing the various types of superconducting systems. In conventional BCS superconductors $\mu/J_S \simeq 1$ and the experimental $J_S(T)$ deviates significantly from the BCS theory at temperatures below the transition. In the cuprate superconductors however this value can be up to $\mu/J_S \simeq 5$.

In any case even though the BKT effect has been observed in a range of superconducting system, its occurrence has not yet been investigated in boron doped diamond. This is mainly due to the assumption that the system is strictly 3D, despite numerous evidence signifying two dimensionality. The experimental characteristics of the BKT transition are well documented and generally easily identified through analysis of temperature dependent transport properties and in the next section the occurrence of the BKT transition is investigated in the superconducting boron doped diamond system. In this study we present the temperature dependence of both resistance and *VI* to verify the occurrence of the BKT transition.

4.2 Universal jump in superfluid stiffness

One of the hallmarks of the BKT transition is the effect of the universal jump in the superfluid stiffness which occurs at the BKT transition temperature. This gives characteristic values for the superfluid stiffness on either side of the transition, namely:

$$J_S(T_{BKT}^{-}) = \frac{2}{\pi} T_{BKT}, \quad J_S(T_{BKT}^{+}) = 0. \qquad (22)$$

According to theory, the temperature dependence of the superfluid stiffness includes both the quasiparticle excitations responsible for driving the stiffness to zero at and above T_C, and the vortex phase fluctuations which are the cause of the discontinuous jump at T_{BKT}. The universal jump in superfluid stiffness and hence the BKT temperature can directly be inferred from the behaviour of the exponent α in the I-V characteristics:

$$V \propto I^{\alpha(T)}, \qquad \alpha(T) = \frac{\pi J_S(T)}{T} + 1. \qquad (23)$$

The superliner behaviour shown here is due to sufficiently large currents causing the unbinding of vortex-antivortex pairs. According to the Kosterlitz-Thouless criterion the parameter α should jump from α = 3 at the BKT temperature to α = 1 above the BKT temperature. At temperature below the BKT point α is expected to increase with decreasing temperature. As shown in figure 21 the voltage-current characteristics are shown on a log-log scale in order to determine the power law scaling. The critical parameter α(T) is determined from the slope of the curves for temperatures ranging from 300 mk to 2.1 K. The crossover from the BKT regime where α = 3 is indicated by the dotted line, also shown is the point at which α = 1 at higher temperature the superconducting phase is destroyed and the systems exhibits a linear behaviour. The power-law behaviour ($V \propto I^{\alpha(T)}$) is clearly observed in the low current regime, here the *V(I)* dependence is predicted to arise from the thermal dissociation of the vortex-antivortex pairs at temperature above the BKT point and from current induced dissociation at temperatures below the BKT point. Using the equation above the superfluid stiffness can be extracted from the α(T) parameter. This is shown in figure 21 (b) where J_S is plotted as a function of temperature for two samples of different grain size. Also shown in figure 21 (b) is the expected behaviour for the superfluid stiffness for a BCS material valid for temperatures above T_C:

$$J^{BCS}(T) = J_0(\frac{T_C - T}{T_C}). \qquad (24)$$

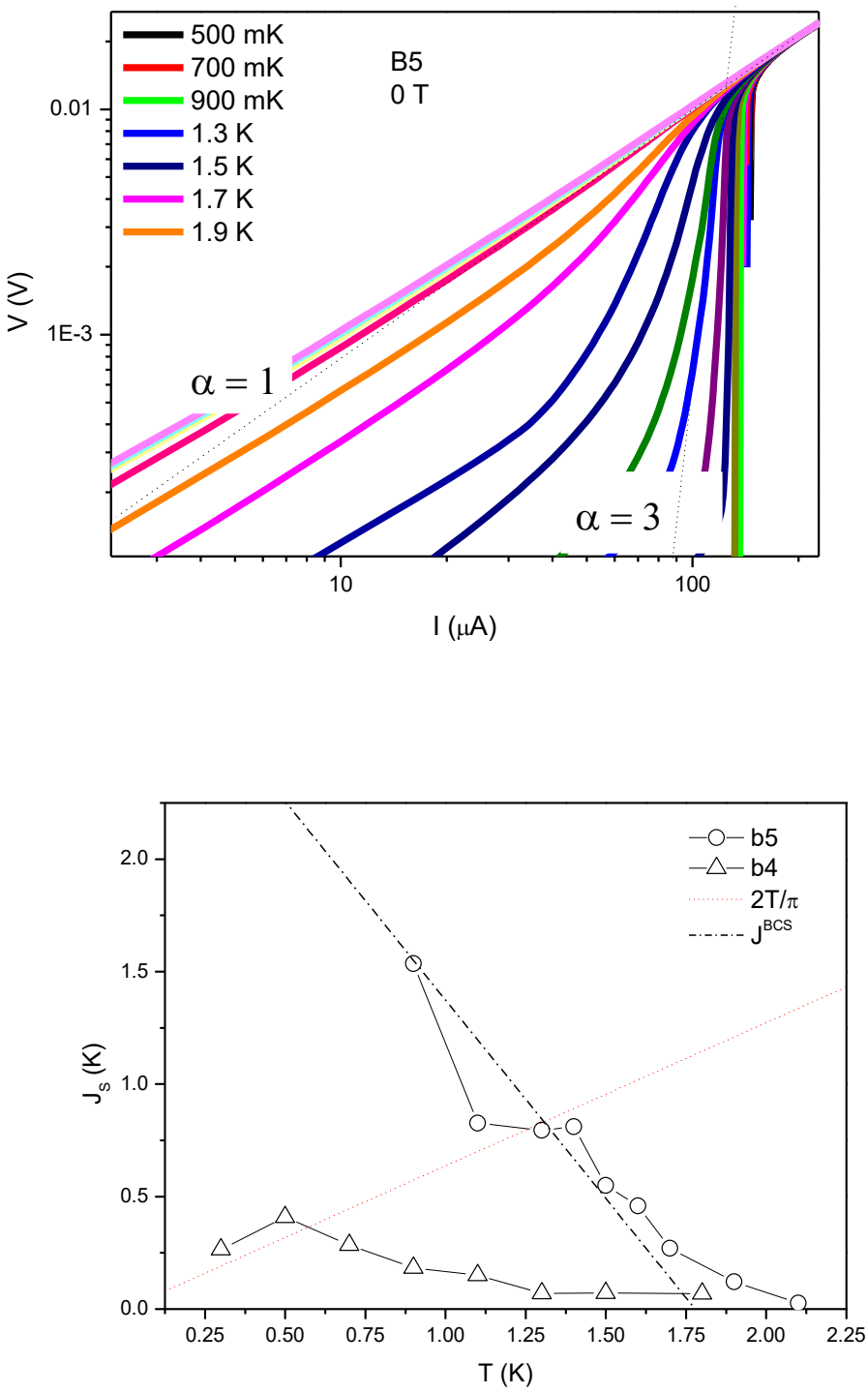

Figure 21 (a) current-voltage response plotted on double log scale. According to the theory, the BKT transition is reached when the $V \sim I^3$ this is indicated by the dotted line and corresponds to a temperature of 1.3 K for the specific sample. (b) The superfluid stiffness as a function of temperature for two different samples. The red dotted line signifies the BKT point. The black dotted line is the linear behaviour predicted by BCS theory.

As the BCS trend does not take into account the effects of vortex binding a clear deviation from the experimental data is observed at temperatures below the BKT point, here defined by the crossing of the red dotted line which is obtained from equation 1 and replacing $J_S(T^-_{BKT})$ by $J^{BCS}(T_{BKT})$, i.e.:

$$J^{BCS}(T_{BKT}) \simeq \frac{2T_{BKT}}{\pi} \rightarrow t_C \simeq \frac{2T_C}{\pi J_0} \qquad (25)$$

The relatively large separation in BKT and mean field critical temperature shown in figure 21 (b) is likely due to confinement effects as has been demonstrated before in homogenously disordered systems or in samples where finite size effects are no longer negligible [89].

This is quite possibly a result of the granularity of the films in this case, as shown in figure 21 (b) the larger grain size sample does show a more broad, less pronounced transition that occurs at lower temperatures.

4.3 Effects of inhomogeneity, finite size and applied magnetic fields

In conventional superconducting materials, the, superconducting transition is usually sharp and T_{BKT} is generally quite close to the T_C.

In cases with a small temperature gap between the two critical points, the superconducting phase will be dominated by Ginzburg-Landua fluctuations described in a previous chapter. In such systems the experimental evidence of the BKT transition can be screened by the simultaneous fast decrease in electron density due to quasiparticle formation near T_C. This is unlike the data demonstrated in samples here where the temperature range between mean field critical point and BKT point can be up to 400 mK, a range large enough to be properly characterized. The broadening of the universal jump in superfluid stiffness has before been reported in cuprate systems with intrinsic inhomogeneity as well as finite size effects [90]. In heterostructured materials the BKT transition has frequently been investigated, here however the superconducting transition is far from the BKT point has generally lead to data being analysed according to the idea that

the fluctuation regime can be described within BKT theory. Such analysis however overlooked certain physical parameters and thus over simplify the system [91]. In order to circumvent this problem a more rigorous model has recently been developed to investigate finite size effects that are likely to play a leading role in the BKT regime, where the broadening in the BKT transition, i.e. the notable resistance tail near the foot of the superconducting regime, was accounted for by converting in a hand waving manor the inhomogeneity's effects into a typical length scale for a particular system [90]. This scale is essentially the mapping of homogenous domains, from the point of view of the superfluid density, within the system that are typically smaller than the actual grain size. Such inhomogeneities are due to impurity scatters or structural defects, whereas finite size effects are a result of granularity. Within this analysis the critical current, above which vortex-antivortex binding leads to the power law behaviour described above, at temperature below the BKT point can be related to this characteristic length scale where such effects are expected to be relevant:

$$I^* = 2\pi J_S \frac{c}{\varphi_0} \frac{L_{phys}}{L}, \qquad (26)$$

Where L_{phys} is the physical size of the sample. Thus from current voltage measurements, the effective homogenous length scale of the system can be identified.

In our samples such finite size effects are observable in temperature dependent *I-V* characteristics as a pronounced hysteresis. The rounded transition of the temperature dependence of the superfluid stiffness as well as broadening of the resistance tail are all indication that finite size and inhomogenieties effect the transport. This is most notable in figure 22 (b) where the critical exponent for samples of different grain size is shown.

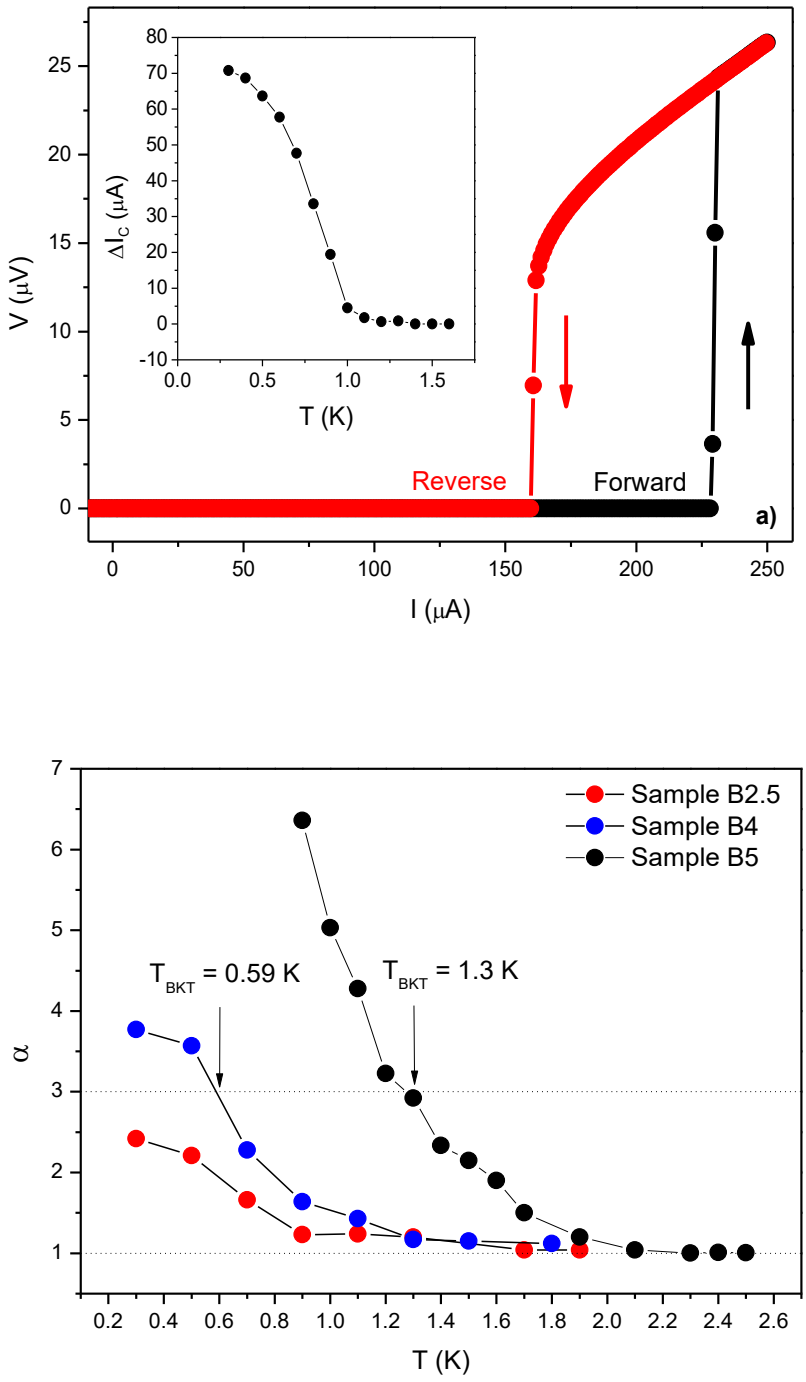

Figure 22 (a) A pronounced hysteresis in the VI curves when measuring from superconducting to normal state or the reverse was observed. This is generally attributed to vortex motion on the resistive side of the transition. The inset shows the temperature dependence of the V-I hysteresis. (b) The BKT transitions (as the mean field superconducting transition) was observed to be dependent on the grain size of the sample, with decreasing grain the BKT temperature increases.

The application of magnetic field has a similar effect to that of fine size structure [89], as shown in figure 23 (a-b), the power law scaling of the *IV* characteristics are greatly changed when with the application of magnetic field. The system is driven away from the BKT transition and the BKT temperature is strongly suppressed (c). The similarity between finite size effects and applied magnetic field has before been studies in refernce [89]. It was there established that the application of the magnetic field ensures an additional limiting length for observing the BKT transition:

$$L_H \propto \left(\frac{\varphi_0}{H}\right)^{1/2} \qquad (27)$$

H being the magnetic field applied perpendicular to the film and is the flux quantum. Thus for small fields where $L < L_H$ the finite size between inhomogeneous regions is the limiting length scale whereas at higher fields where $L_H > L$, the magnetic field will set the limiting length scale. In the high field range the magnetic field controls the density of free vortices which in turn determines the sheet resistance, according to [89] this will lead to saturating of the sheet resistance. Thus the applied field acts in a similar way to finite size or small inhomogeneous distribution, and suppresses the BKT transition driving it to lower temperatures. This is demonstrated in figure 23 (c) where the applied field greatly suppresses the temperature dependence of the critical exponent moving it to temperatures not experimentally achievable using the current measurement set up.

In any case, taking into account the microstructure and nature of the diamond grains it is not surprising that such phenomena are observed in the boron doped diamond, the system has a large concentration of scattering impurities and the granularity is expected to allow for a variation of the Coulomb potential throughout the system, thus ensuring that the BKT transition, just like the mean field superconducting transition, occurs at a local level depending on the local electronic environment and the observed transition point is an averaging over the system. This leads to the broadening of the transition observed in our samples.

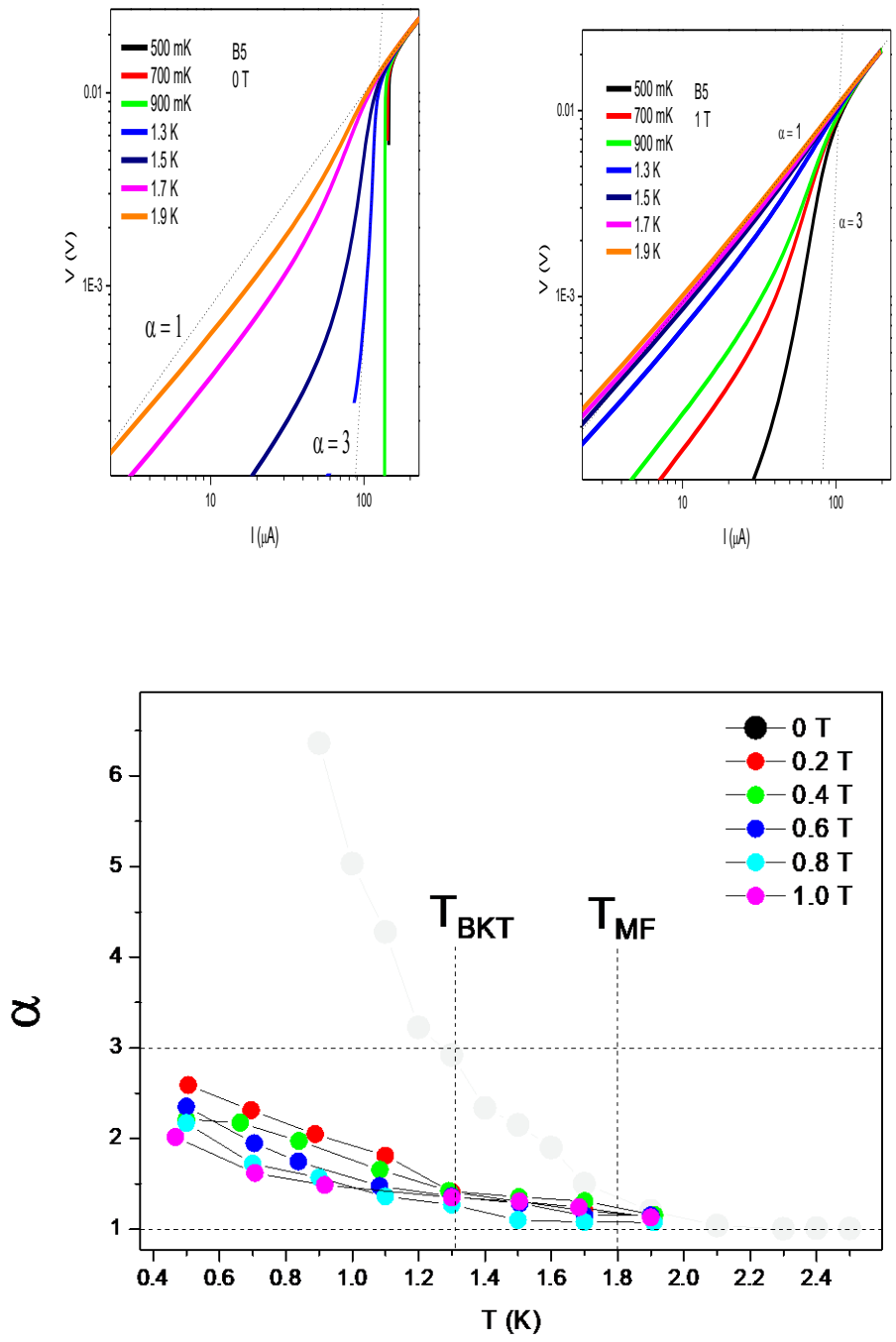

Figure 23 (a) The BKT transition was also found to be supressed heavily by the application of magnetic field. This can be measured by comparing the temperature dependent IV characteristics at different magnetic fields (b) The IV characteristics at 1 T, the slope of the IV characteristics do not reach $V \sim I^3$ in the same temperature range as in (a). The critical exponent describing the IV sweeps is plotted as a function of temperature at different magnetic fields, the curves do not cross 3 in the experimentally accessible temperature range.

4.4 Temperature dependent resistance and the Halperin-Nelson equation

The BKT transition can also be identified in the temperature dependent resistance, this is achieved firstly through analysis of the fluctuation (excess conductivity) region of the superconducting transition in a similar fashion to the scaling relations developed for fluctuation spectroscopy above T_C. The main concept is that the conductivity in this region is influenced heavily by the density of free vortices above the BKT point. The vortex density can be related to the coherence length ξ as $2\pi n_f = 1/\xi^2$ so that close to the transition the ratio between resistance and normal state resistance R_N is given by:

$$\frac{R}{R_N} = 2\pi\xi_0^2 n_F = (\frac{\xi_0}{\xi})^2, \qquad (28)$$

This formula is generally quoted in literature as the paraconductivity due to vortex proliferation. This can be compared to Aslamazov-Larkin (AL) contribution to the conductivity based on Ginzburg-Landua fluctuations, the difference being in the latter case the coherence length has a specific temperature dependence, i.e. $\xi_{GL}^2 \sim T_C/(T - T_C)$, where T_C is the mean field critical point. In a 2D film, the BKT transition occurs below the T_C unlike the fluctuation spectroscopy which occurs above. The distance between the BKT transition and mean field critical temperatures is a function of the microscopic properties of the system and be can very small to a few degree kelvin depending on the material. The conductivity therefore crosses over from the GL regime where it shows power law divergence approaching T_C to the BKT regime identified by the asymptotically diverging coherence length as it approaches the BKT point, i.e.:

$$\xi \sim e^{(b/\sqrt{t})}, \qquad (29)$$

Where t is the reduced temperature given by:

$$t = \frac{T - T_{BKT}}{T_{BKT}}, \qquad t_C = \frac{T_C - T_{BKT}}{T_{BKT}}. \qquad (30)$$

In the pioneering work of Halperin and Nelson [92] it was observed that the BKT fluctuations only occur in the temperature range$t \ll t_c$. From this the now well-known interpolation formula connecting the GL and BKT regimes was obtained:

$$\Delta\sigma = a_{HN}\sigma_N sinh^2(\sqrt{b_N t_C/t}), \qquad (31)$$

Where b_N is a dimensionless constant of order 1. This interpolation scheme thus allows for the exponential divergence of the paraconductivity which is characteristic of the BKT physics at temperatures $b_N t_C/t \gg 1$, and the power law behaviour indicative of the GL behaviour for temperatures $b_N t_C/t \gg 1$. Although used frequently in analysis there is some ambiguity regarding this formula and the fixing of parameters such as the prefactor and exponential coefficients. This ambiguity has led to research directed at improving upon the work of Halperine and Nelson. Recently a modified HN formula has been suggested [90] for fitting the normalized resistance between T_{BKT} and T_C:

$$\frac{R_N}{R} = 1 + (\frac{2}{A} sinh \frac{b}{\sqrt{t}})^2 \qquad (32)$$

this is indicated by the blue solid line in figure 10 (a). The BKT temperature obtained from the HN fitting is the same as that obtained from the *VI* analysis (i.e. 1.3 K for the sample presented here). This occurrence of a transition is also demonstrated when plotting the temperature dependent resistance on a Log scale. As shown in figure 24 (b), the resistance then clearly shows a resistive peak feature at the BKT temperature. As before, when the magnetic field is applied, the BKT transition is not observed indicated by the absence of the resistive upturn. Further verification of the BKT transition can be made by comparing the resistance data to predictions of the BKT theory [93], i.e. showing that the resistance tail below T_c depends exponentially on the inverse square root of the reduced temperature:

$$Ln\left[\frac{R_s(T)}{R_n}\right] = a - bt^{-1/2} \qquad (33)$$

or through analysing the temperature dependence of:

$$[\frac{d(\ln(R))}{dT}]^{-2/3} \qquad (34)$$

As shown in figure 25 (a & b) both representations yield a BKT temperature of between 1.27 – 1.31 K, i.e. a deviation of only 40 mK, indicating good consistency between respective models as well as the BKT temperature arrived at through I-V power law scaling.

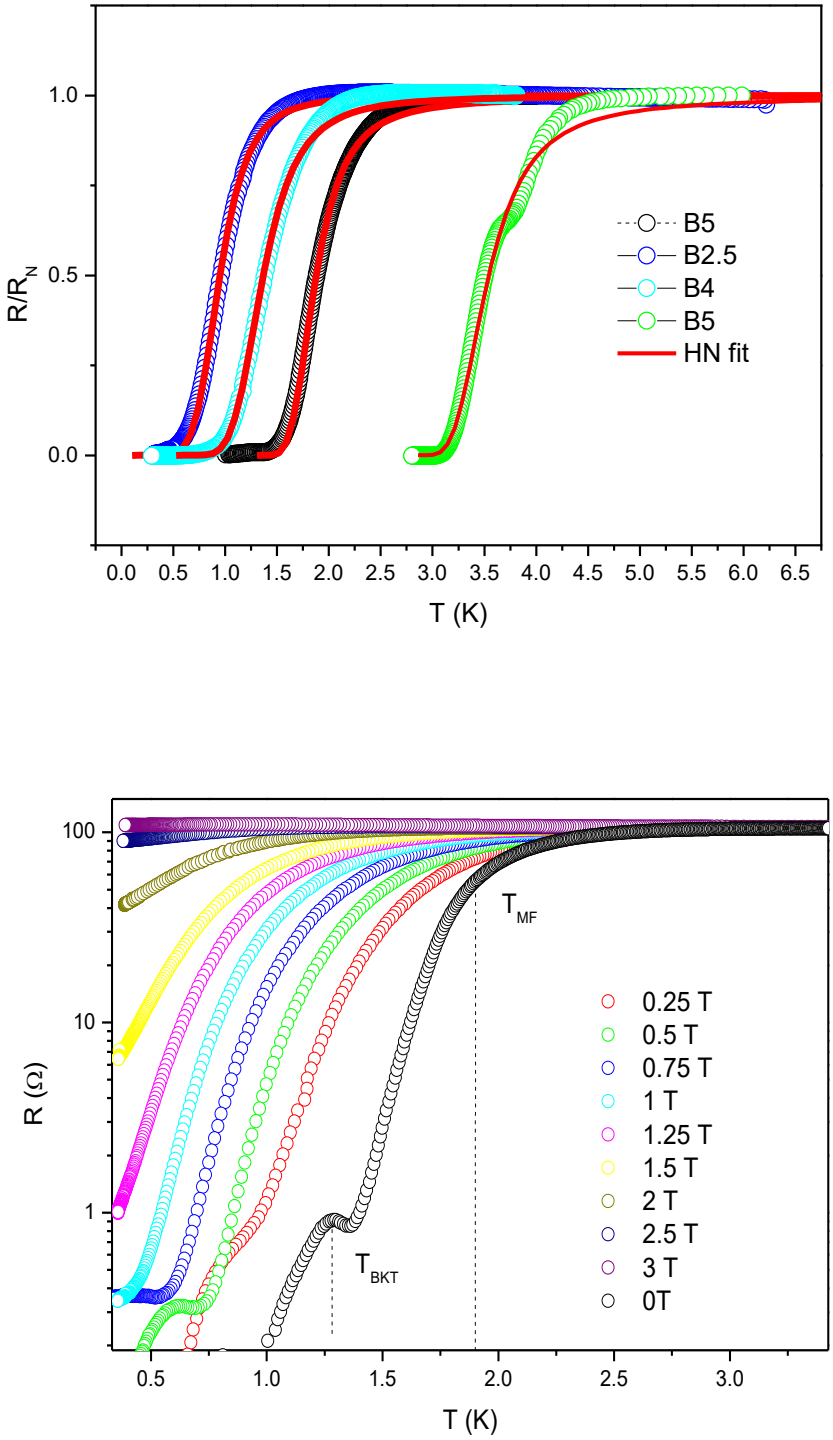

Figure 24. (a) The temperature dependent resistance for the samples of different grain size studied. The red line is a fitting to the HN equation in order to extract the BKT temperature and information regarding the vortex core. (b) In log scale the BKT point can clearly be observed as an increase in resistance leading to a local maximum in the resistance at the same temperature determined as the BKT through IV scaling.

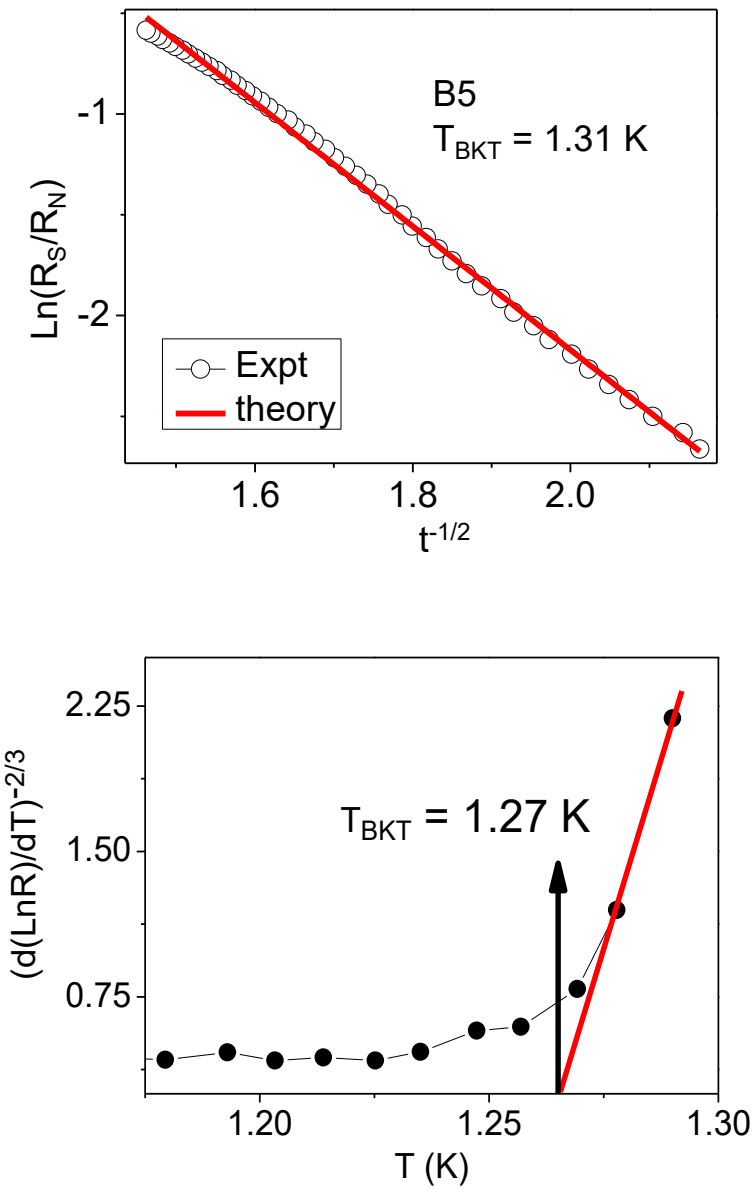

Figure 25. (a) and (b) are various representation schemes for the temperature dependent resistance data where the BKT transition temperature can be confirmed within a temperature margin of only 40 mK, this along with the correlation to the BKT temperature obtained from the IV characteristics is a good indication of the consistency of our findings.

At temperatures below the mean field critical point, the observation of the BKT transition, which is the vortex-antivortex binding point, is most likely a result of the Josephson coupling between adjacent grains, similar to the coupling between 2D layers in the high T_C cuprates [87]. The suppression of this BKT transition with applied field can be explained as a result of the magnetic flux lines which propagate along the grain boundaries decreasing the coupling strength between the grains and imposing limitations of the vortex interaction distance as

explained before. Having presented evidence for both the 2D nature and the topological excitations causing the BKT transition, it is quite plausible to expect a topological phase. The occurrence of topologically protected phases have been theoretically predicted and experimentally observed in a wide range of low dimensional carbon and boron materials [94]. In fact very recently fermi-arcs were observed in the fermi surface of a low dimensional boron called borophene [95]. Recent XRD and Raman spectroscopy studies based on polycrystalline boron doped diamond also suggested the existence of structurally arranged bilayer boron [11] and since weak surface superconductivity in single crystal bulk boron doped diamond [96] has already been observed it is not difficult to imagine the existence of a topological 2D phase in nanocrystalline films presented here. The realization of a topological 2D phase raises some interesting questions particularly regarding the possibility of a non-trivial topological phase which would provide an ideal situation to study potential topological phenomena. Furthermore the coupling between topological grains can be switched by applying a small magnetic field. These properties may be of interest for the development of novel diamond based topological qubits such as the top-Transmon.

Chapter 5

Additional unconventional transport features

5.1 Mid Gap bound State

In addition to the low dimensional transport features described additional unconventional properties have been observed in the boron-doped diamond system. A zero-bias conductance (ZBC) peak Fig. 26 (d). Although this feature is commonly reported to be a signature of Kondo resonance [96] ZBCPs have been observed in both superconducting [97] and pseudo-spin correlated [98] systems, however the analysis for the latter is not as well-known and is currently the focus of intense investigation in the field of quantum dot research [99]. A ZBCP has before been observed in high temperature superconductors where such observation was described as resulting from either spin correlated tunnelling [100] or to the anisotropic d-wave order parameter of such systems due to Andreev reflection [101]. The observation here therefore raises some fundamental questions as to the nature of superconductivity in boron doped diamond.

Due to the unknown origin of the ZBCP we first investigate the resonance features in light of conventional Kondo theory. The two main features of ZBCPs that are routinely analysed are the temperature dependent peak height and full width at half maximum (FWHM). For a spin/pseudo-spin Kondo effect the differential conductance peak height is expected to have a logarithmic temperature dependence. This is however not observed in our samples and as shown in figure 27 (a) the peak height follows a power law scaling. To our knowledge this has not yet been observed in ZBCPs and there does not exist any theoretical model to fit our data. When analysing the FWHM temperature dependence however, we can clearly identify two different scaling regimes dictated by the critical temperature of the samples. This is shown in figure 27 (b), where the FWHM is observed to closely follow the expected temperature dependence (given by equation 6) at temperatures above T_C but however crosses over to a power law dependence at temperatures below T_C.

$$\Gamma = \frac{1}{2}\sqrt{(\alpha K_b T)^2 + (2K_b T_K)^2} \qquad (35)$$

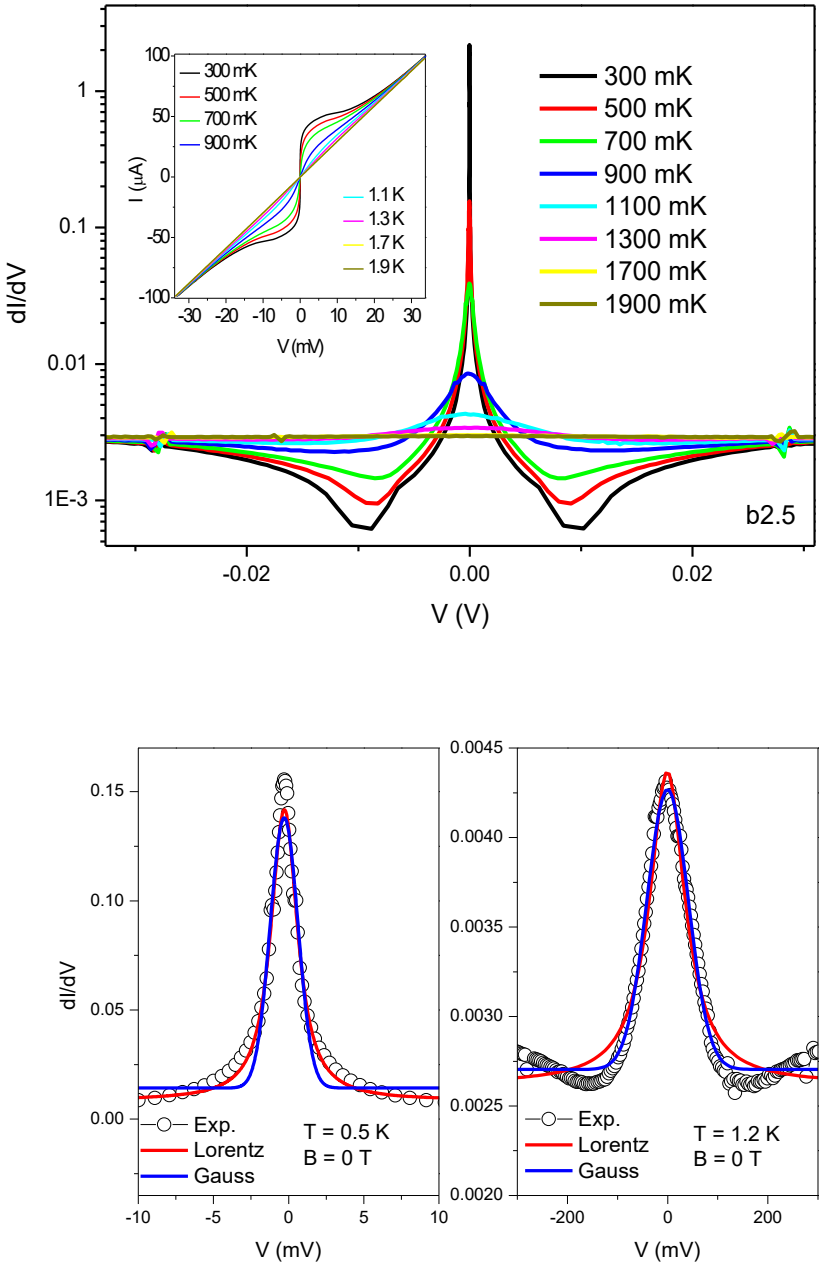

Figure 26 (a) Differential conductance curves showing a pronounced zero bias anomaly observed at temperatures from the fluctuation conductance regime with increasing height as temperature decreases. The FWHM of the ZBCP broadens with temperature increase. Inset shown the current voltage data the differential conductance is derived from. Fig. 1.4.1.b. In addition to the broadening of the FWHM and decrease in peak height, there is a change in the functional form of the ZBP as the temperature crosses the T_C. At temperatures below T_C the ZBP has a more distinct Lorentzian shape whereas at temperature above T_C, the ZBCP has a more Gaussian profile.

Where K_b is the Boltzmann cnstrant and T_K is the Kondo temperature obtained from fitting the T^2 dependence of the resistive peak given in reference 43 where the possibility of a charge-kondo effect was investigated in this system. Such features have to our knowledge not yet been reports for the ZBCP of superconducting systems, these transport features do however imply that the formation of the peak above T_C may be a Kondo-like effect with additional correlations existing below the T_C causing deviation from the Kondo theory.

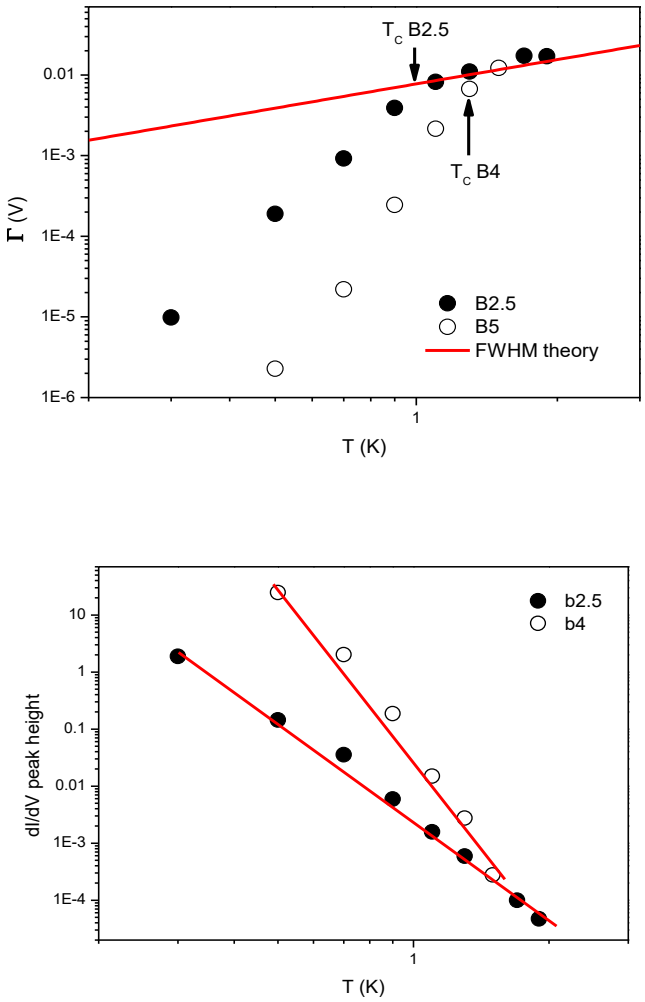

Figure 27 (a) The temperature dependence of the FWHM of the ZBCP for two samples. There is a clear temperature dependent change in FWHM crossing the mean field critical point. Above the T_C the FWHM follows an exponential indicated by the red line, at temperatures below the T_C the FWHM shows a power law temperature dependence. (b) The ZBCP height as a function of temperature, the peak height was found to scale to a power law relation throughout the entire temperature range, having no identifiable crossover as in the case of the FWHM.

The ZBCP also show strong magnetic field dependence, this is shown in figure 29 (a) where the applied field greatly suppresses the resonance peaks as well as changes the functional form of the peak structure. According to the Applebaum-Anderson model [100] the ZBCP can be replotted as the difference between isotherm field dependent isotherms and the zero field sweep (G(B) – G(0 T)), this allows for the subtraction of the steep mid peak and highlights the split peak features which, for spin correlated system are supposed to follow a linear Zeeman splitting with increasing field strength [102]. Deviation from the linear splitting has before been used as verification of d-wave parity of the order parameter, in fact the observation of such resonance peaks is expected to occur for non-s wave superconductors only as it is a result of the sign change of the order parameter at the interface due to the anisotropic parity of such systems [103]. The system at present appears to be somewhat more complicated, here after the subtraction of the central peak from the respective field dependent isotherms show the split peaks but no further Zeeman shifting when the field is increased, in fact the peaks only increase in height but remain at the same level spacing, this is a strong indication that although similar to a spin-Kondo effect, this system is not strictly dependent on the magnetic field and more likely to result from pseudo-spin effects.

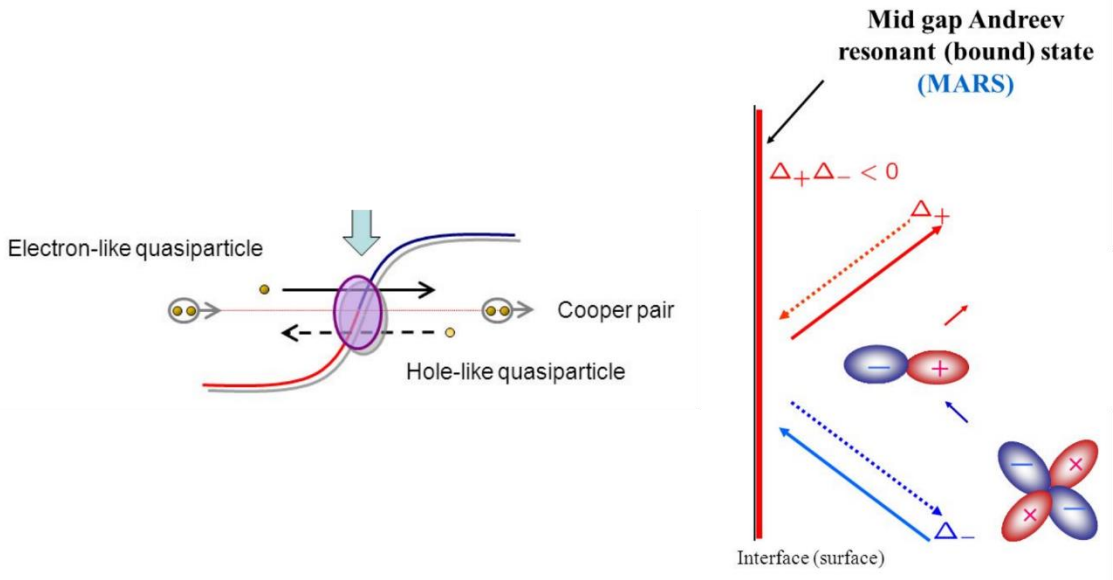

Figure 28 The Mid Gap Andreev bound state is due to constructive interference of hole-like and electron-like quasiparticles at the interface of superconducting and other systems. This is due to the sing change of the parity of the order parameter due to its anisotropic nature (in non-s-wave superconductors). Diagram obtained from http://slideplayer.com/slide/7522639/

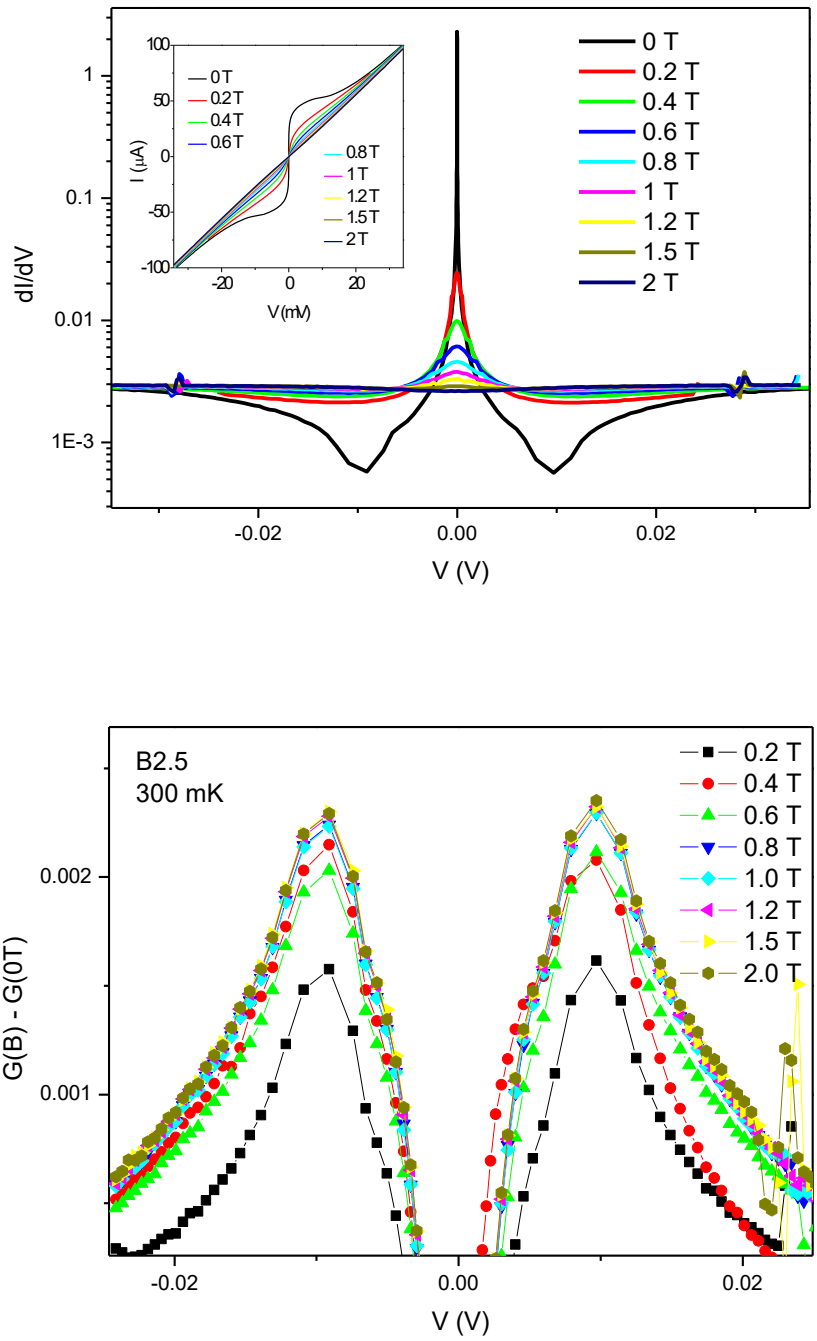

Figure 29 (a) Zero Bias Conductance peaks in the differential conductance also demonstrated a strong decrease in height and FWHM with increasing field. Inset shows the effect of magnetic field on the current voltage characteristics of the film. (b) Identification of the Zeeman splitting once he zero field peak is subtracted from each magneto-therm. Although the split peak structure is clearly visible they do not exhibit much shifting as field is increased up to 2 T.

5.2 Anomalous magnetoresistance features and weak antilocalization

As mentioned in a previous section the temperature dependence of the resistance of the boron doped diamond system shows interesting re-entrant features below the mean field critical temperature. This re-entrant feature has been described as a bosonic anomaly [42] and is strongly field and measurement bias dependent [43]. Shown in figure 29 (a) is the double logarithmic scaling of the temperature dependent resistance at various magnetic fields. The zero field curve clearly undergoes the superconducting transition but exhibits the re-entrant peak at approximately 0.7 K, after which the resistance decreases steadily and reaches a saturating value of approximately 10 Ω. The residual resistance of the system has yet to be studied and to date, not much is known of the nature of the re-entrant bosonic peak. In figure 29 (b) the low field magnetoresistance at temperatures below the peak maximum is shown. A very clear transition from a negative magnetoresistance regime at temperatures near the peak maximum to a positive magnetoresistance as the system is cooled is shown. Additional features such as a temperature independent small value critical field of approximately 0.35 T can be identified by the intersection of all curves in that temperature range. At fields higher than this critical point the magnetoresistance shows a parabolic upturn that is supressed with decreasing temperatures. These features have not been reported for the system before and have been observed in the entire range of sample studied here.

The crossover from a negative to positive magnetoresistance is a well-known phenomenon for materials such as graphene and its 3D analogues such as Dirac and Weyl semi-metals. These materials have characteristic linear dispersion relations with conduction and valence bands in the form of Dirac cones which intersect at specific point in the Brillouin zone. In Graphene the crossover from a negative to positive magnetoresistance has been explained as a change in the scattering mechanism between valleys of different chirality: the weak localization effect is a result of intervalley scattering (time reversal invariant regime) which changes to a weak anti-localization regime (with spontaneous broken time reversal symmetry) with lowering temperature [104]. The situation is somewhat more complicated in topologically non-trivial materials where inversion symmetry breaking, magnetic impurity scattering as well as time reversal symmetry breaking has been shown to lead to the crossover [105-107]. However all such mechanism rely on the fact that such materials have a linear dispersion relation, which has not been established in boron-doped diamond.

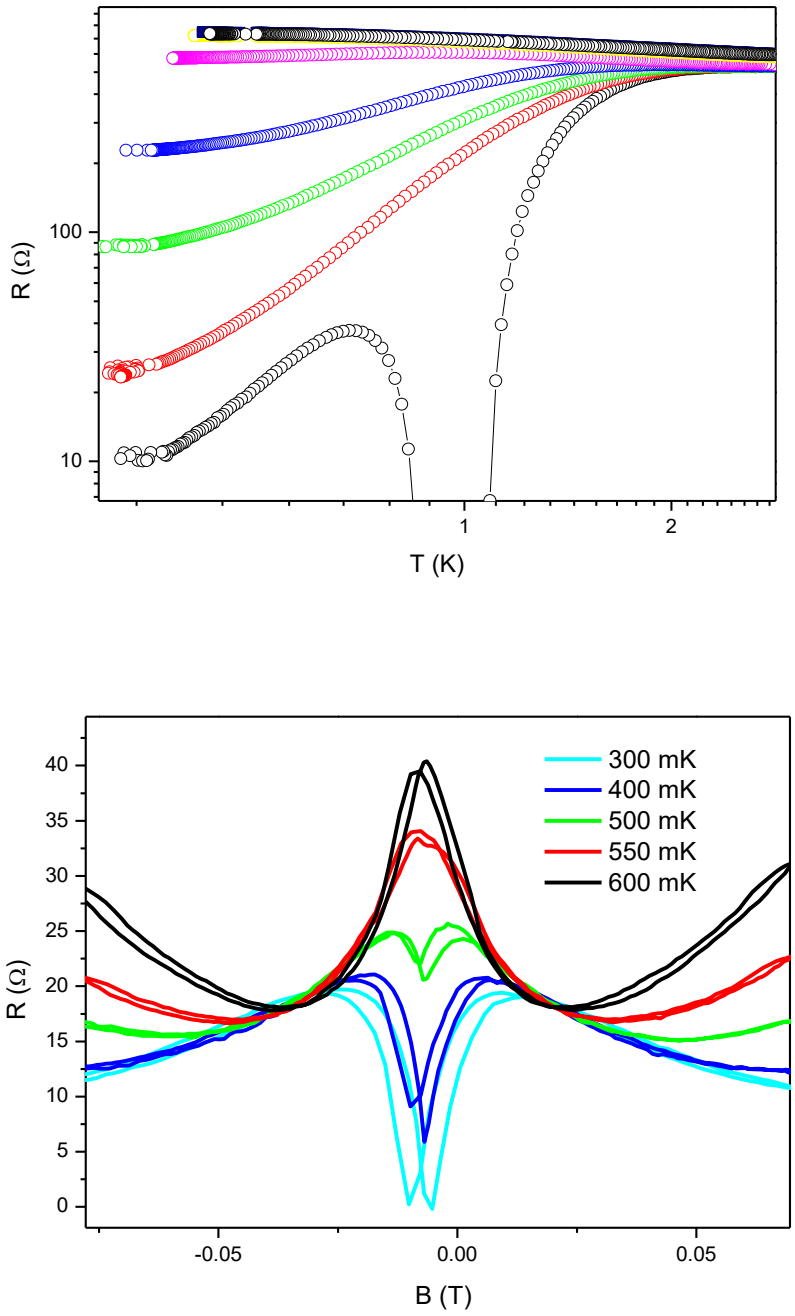

Figure 30 (a) The temperature dependent resistance plotted in double log scale. As shown before re-entrant features that peak at the BKT temperature occur under certain measurement conditions. The small yet finite resistance of this re-entrant phase has not yet been investigated. (b) The low field magnetoresistance of this finite resistance regime shows a crossover from a negative magnetoresistance to a positive magnatoiresistance as temperature is reduced. These features are similar to the weak localization to anti-localization that occurs in Dirac and Weyl semi-metal systems.

The determination of the band structure and such linear disperion relations are typically experimentally investigated through ARPES measurements. Although, as pointed out in the introductory chapter, ARPES measuremetns have been conducted on boron doped diamond, these studies have focused on the bulk bands and to date no studies on the surface state of the superconducting diamond system have been conducted. It has been known for some time already that polished diamond has a definite surface state [108] and recently atomically flat diamond surfaces have exhibited Landau quantization of a hole gas in the formation of Shubnikov de Haas oscillations [109], there the local carrier mobility was determined to be as high as several thousand cm^2/V s at low temperature. Additionally, as determined by the microstructure analysis such as HR-TEM and EELS, the grain boundaries of the system are known to be composed of a low dimensional boron-carbide interfacial material. This is significant as such boron phases are frequencly investigated as potential Dirac materials with non trivial topology, as recently shown in the Borophene system [95].

Thus the realization of such magnetoresistance features in this system along with the knowledge of the complex microstructure calls for a more thorough investigation into the possibilty of a topological band structure. This is particularly interesting when considering the wealth of evidence [110] suggesting the heavy doping of boron leads to a low lying hole impurity band that increases in weight with boping concentration. It is then not difficult to imagin the intersection of hole impurity band with the intrinsic valence diamond band, possibly leading to a linear dispersion at such points that can responsible for the magnetoresistance observed here.

To better understand the phenomena, the magnetoresistance is analyzed in light of the HLN formalizim [111] as usually conducted for materials with non-trivial toplogical phases. Acordingly the crossover from the negativce to positive magnetoresistance is explained in terms of a temperature competition between scattering events, either intervalley or intravalley scattering (which can interm be related to previous chapters where with lower temperture the system was shown to exhibit a crossover from intragranular to intergranualr transport regimes). The HLN formula is given by:

$$\Delta\sigma(B) = \frac{e^2}{\pi h}\left(F\left(\frac{\tau_B^{-1}}{\tau_\varphi^{-1}}\right) - F\left(\frac{\tau_B^{-1}}{\tau_\varphi^{-1}+2\tau_i^{-1}}\right) - 2F\left(\frac{\tau_B^{-1}}{\tau_\varphi^{-1}+\tau_i^{-1}+\tau_*^{-1}}\right)\right) \qquad (36)$$

Where F(x) is the diagamma function, τ_φ^{-1} is the dephasing scattering rate, τ_i^{-1} is the intervalley scattering rate andτ_*^{-1} is the intravalley scattering rate. However due to the additional change

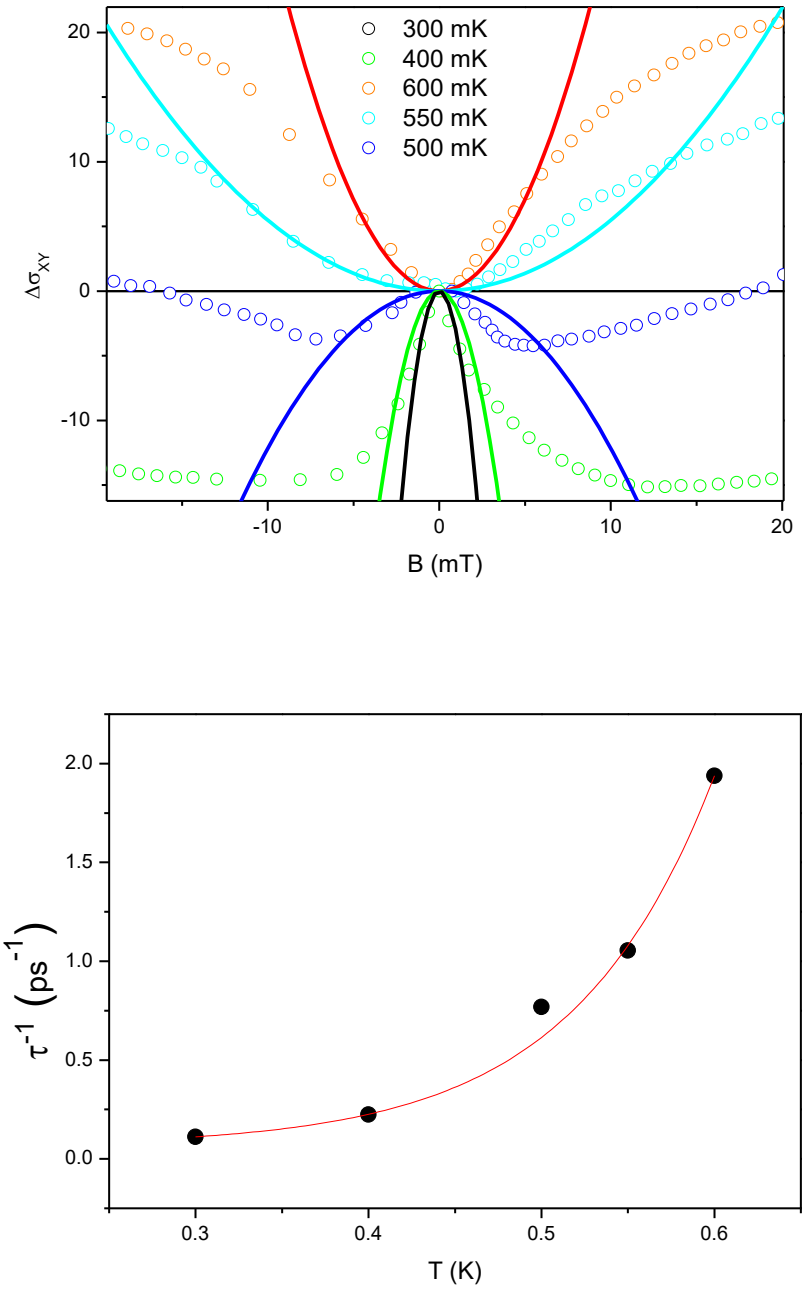

Figure 31 (a) The magnetoconductance represented as the difference between conductance at applied field and the zero field value. Only the low field region is shown as this is the region of interest that can be fitted to equation. Scattering events not related to inter and intra valley competition are responsible for the additional magnetoresistance features causing deviation from the parabolic fitting. (b) The temperature dependent intervalley scattering rate is determined from the fitting of equation 36, as shown this scattering rate increases steeply with increasing temperatures, similar to topological insulating materials.

in magnetoresiustance behaviour after the critical field we find it is better to fit the data with the approximate form of the equation which is parablic and valid for the low field regions only. This is given by:

$$\Delta\sigma(B) = \frac{e^2}{24\pi h}\left(\frac{4eDB\tau_\varphi}{\hbar}\right)^2 \left(1 - \left(\frac{1}{\left(1+{}^{2\tau_\varphi}/_{\tau_i}\right)^2}\right) - \left(\frac{2}{\left(1+{}^{\tau_\varphi}/_{\tau_i}+{}^{\tau_\varphi}/_{\tau_*}\right)^2}\right)\right) \quad (37)$$

Where D is the diffusion constant taken from reference [] and B is the applied field. The fitting of the data to this approximate form of the HLN equation is shown in figure 30 (a) where the sdame data presented in figuer 29 (b) has been recast as the difference in magnetoconductance at applied fields and zero field for each isotherm. As can be seen there the fitting only captures the low field region adequetly but can however be fitted to the entire temperature range of curves. From the best curve fitting we extract the temerpature dependence of the intervalley sattering rate (shown in figure 30 (b)), as expected and comparable to the topological non-trivial materials [112] this scattering rate increases with increasding temperature, leading to the negative manetoresistance as temperature is increased.

In additiona to the crossover from a negative to positive magnetoresistance we have observed anomalous features possiblity related to the chiral anomaly that is generally taken as a signiture of a Weyl semi-metal system [113]. This is shownin figure 31 (a) where the low field magnetoresitance is measureedd at different applied biases. As seen there the weak anti-localization peak structure can greatly be enhanced by lowering the measurement bias, also observed is a pronounced apparent negative resistance region that decreases substantially with increasing field strength. Recently there have been a number of reports on the experimental observation of Weyl systems based on the chiral anomaly. For Weyl semimetals in the absence of any gauge field coupling, the numbers of Weyl fermions of different chirality is separately conserved. However, with the application of parallel electric and magnetic fields, the separate number conservation laws are violated due to subtle quantum mechanical effects [114,115], leaving only the total number of fermions to be conserved. In other words by applying magnetic and electric fields along the same plane can lead to charge pumping of ferions from one weyl node to another (i.e. intervalley scattering), this leads to the very large negative magnetoresistance characterisitc of the Weyl materials.

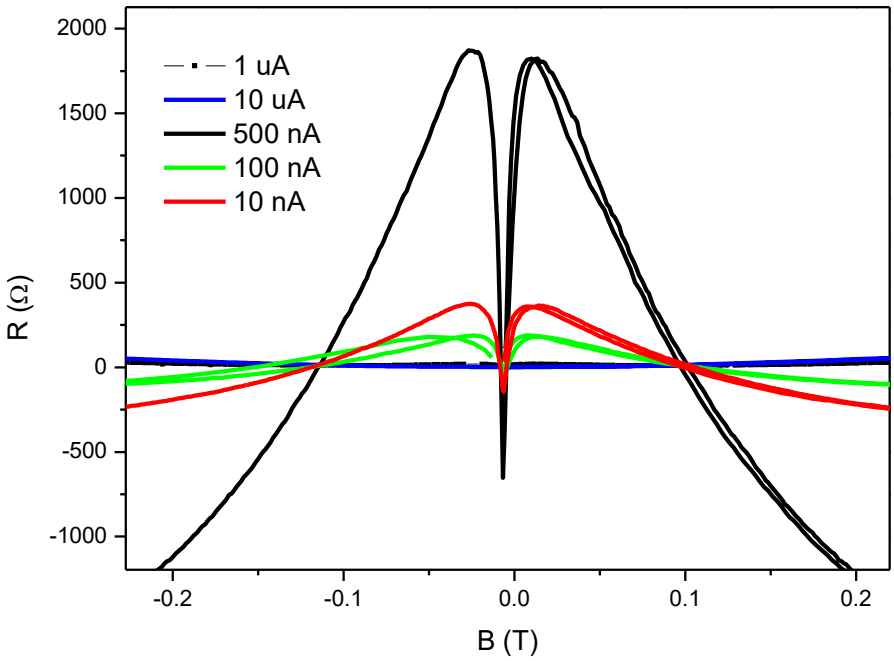

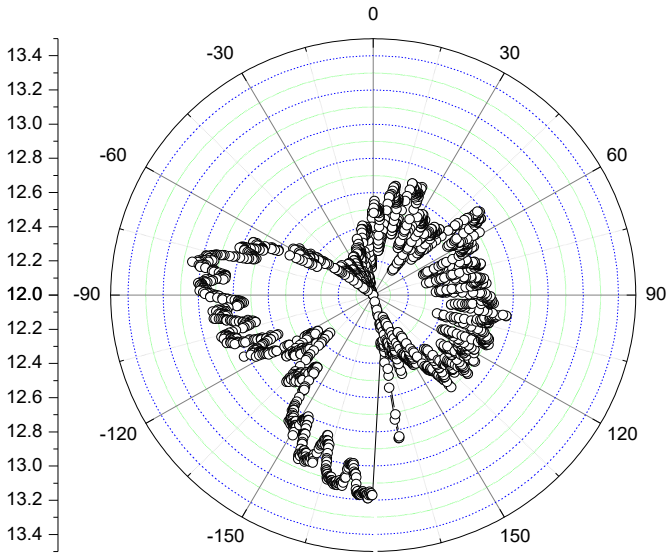

Figure32.a. The low temperature resistive phase is highly sensitive to the value of the applied current and can be tuned to show peak features higher than the normal state resistance. A pronounced negative magnetoresistance phase is also observed after passing a temperature independent critical field crossing point. These features are similar to what has been reported for a number of topological insulators and are related to the so called chiral

The existrance of Weyl charactersitics have been examined using angle dependet magnetoressitance as the negative magnetoresistance features described above intimaterly dependent on the alingment of the applied magnetic field and direction of electric field driving the DC measnurement. Thus far Weyl systems have exhibited periodic magnetoresistance features with a period of 90 ˚[116]. However in such reports the system is generally compossed of 2D thin film samples or single crystals with well defined surface structure and geometry. In the case of the boron doped diamond however the situation is complicated by the complex microsctructure. As shown in figure 31 (b) the boron doped diamond samples do exhbit pronounced angular dependence in the magnetoiresistance, however the period of oscillation in 45 ˚. It has also recently been shown that two different classes of Weyl semi-metals exist, named type 1 and type 2 [117]. The difference being how the linear dispersion at the Weyl points are oriented with respect to each other. This is shown in figure 32 where Type 1 Weyl points are located on the same plane (fermi level) and type 2 where the intersection of conduction and valence bands is skewed. Considering the ARPES resutls shown in figure 2 of the introduction it is tempting to assume a type 2 situation for the boron doped diamond wher the electron and hole pockets can be connected to the intrinsic diamond valence and boron dopant (hole) impurity bands respectivly.

Although this chapter presents analysis that is somewhat speculative due to the lack of information regarding the band structure of boron-doped diamond, the anomalous mangetoresitance features such as temperature dependent crossover from negative to positve magnetoresitance and angle depenent oscillations hint at possible non-trivial topology and will most definitly be requiring additional transport as well as complimentary studies in order to further investigate such features.

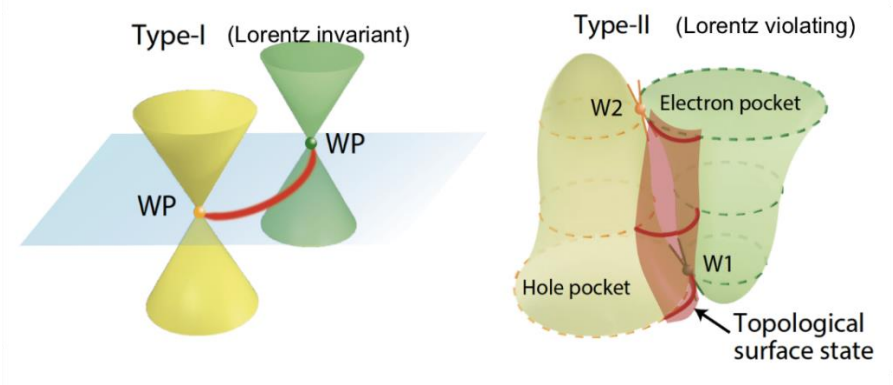

Figure 33. The two classes of Weyl semi-metals. Figure from reference [117]

Concluding remarks on the superconducting boron-doped diamond section.

The first part of this thesis has directly probed quantum transport features that are related to low dimensionality of the nanocrystalline diamond system. Not only has the possibility of a 2D phase been demonstrated through the AL scaling theories, but the manifestation various physical phenomena related to two dimensionality have also been observed. This includes the observation of a BKT transition which is possibly of the charge subclass of this universal class. The observation of a BKT transition is significant as it highlights the existence of topological defects related to vortex and antivortex binding. This theme was followed in subsequent chapters where low field magnetoresistance measurements indicated a number of phenomena related to symmetry breaking effects including a transition from a negative to positive magnetoresistance which shows similar character to the Dirac and Weyl topological materials recently discovered. This is an intriguing discovery, as it is well known that in the transition regio0n the superconductivity is in a mixed state which includes both the Cooper pair superfluid as well as the diminishing but finite density of states of normal state electrons, if the 2D indeed occurs, then it is quite plausible that normal state electrons can show Dirac or Weyl dispersions. This is particularly relevant when considering recent verification of fermi-arcs in low dimensional boron, a material believed to occur along the grain boundaries of the system. In any case from this study it is quite clear that the granular system does in fact exhibit a number of interesting features that are quite similar to the well-established 2D systems. This highlights the need for deeper investigations into the pairing of the system as the material is likely to be reclassified as an unconventional system.

Part 2

Strain engineering in Graphene

Chapter 6

Strain engineering in graphene

6.1 Dirac dispersion of electrons

Graphene is one of those rare and special materials that are able to seemly overnight explode onto the research scene, causing excitement due to new and interesting physics in a relatively easily accessible system. Although theoretically investigated as far back as [118], the real advancements in graphene research occurred in 2004 when a team headed by K. Novosolov and A. Geim from the university of Manchester were for the first time able to experimentally isolate a single layer of graphene and extensively test the quantum signatures of this Dirac semi-metal [119]. This study lead to the 2010 Nobel prize in physics and since then graphene has seem an almost unprecedented amount of research attention, not only is graphene relatively easily produced from low cost materials, devices using conventional semiconducting fabrication techniques can be implemented ensuring that a wide research community could have access to study this material. The large amount of research activity surrounding graphene has been largely due to the exceptional quantum transport features due to the linear dispersion predicted by Wallace [118]. In graphene the hexagonal symmetry of the carbon lattice (shown in figure (a)) leads to hexagonal lattice in the Brillouin zone. The vertices of the Brillouin zone touch at special points, i.e. the K and K' points, leading to the linear dispersion and thus the relativistic physics enjoyed by this fermionic system. The charge carriers in graphene obey the Dirac-Like Hamiltonian:

$$H_K = v_f \sigma \cdot p \qquad (38)$$

Where v_f is the Fermi velocity of electrons in graphene ($v_f \sim 10^6$ m.s^{-1}), σ and p are the pseudospin and momentum operators respectively which are Pauli matrices in this two-band model around the *k* point. The band structure also has a non-trivial topology, with the states near the Dirac cones having a Berry phase of π meaning that they change their sign when covering a closed circuit in the reciprocal space (from K to K' points). This linear dispersion relation in graphene leads to some very interesting physical properties of the charge carriers. Being an ideal two dimensional material, some of the first investigations into the quantum transport investigated the Quantum Hall effect (QHE), this is shown in figure

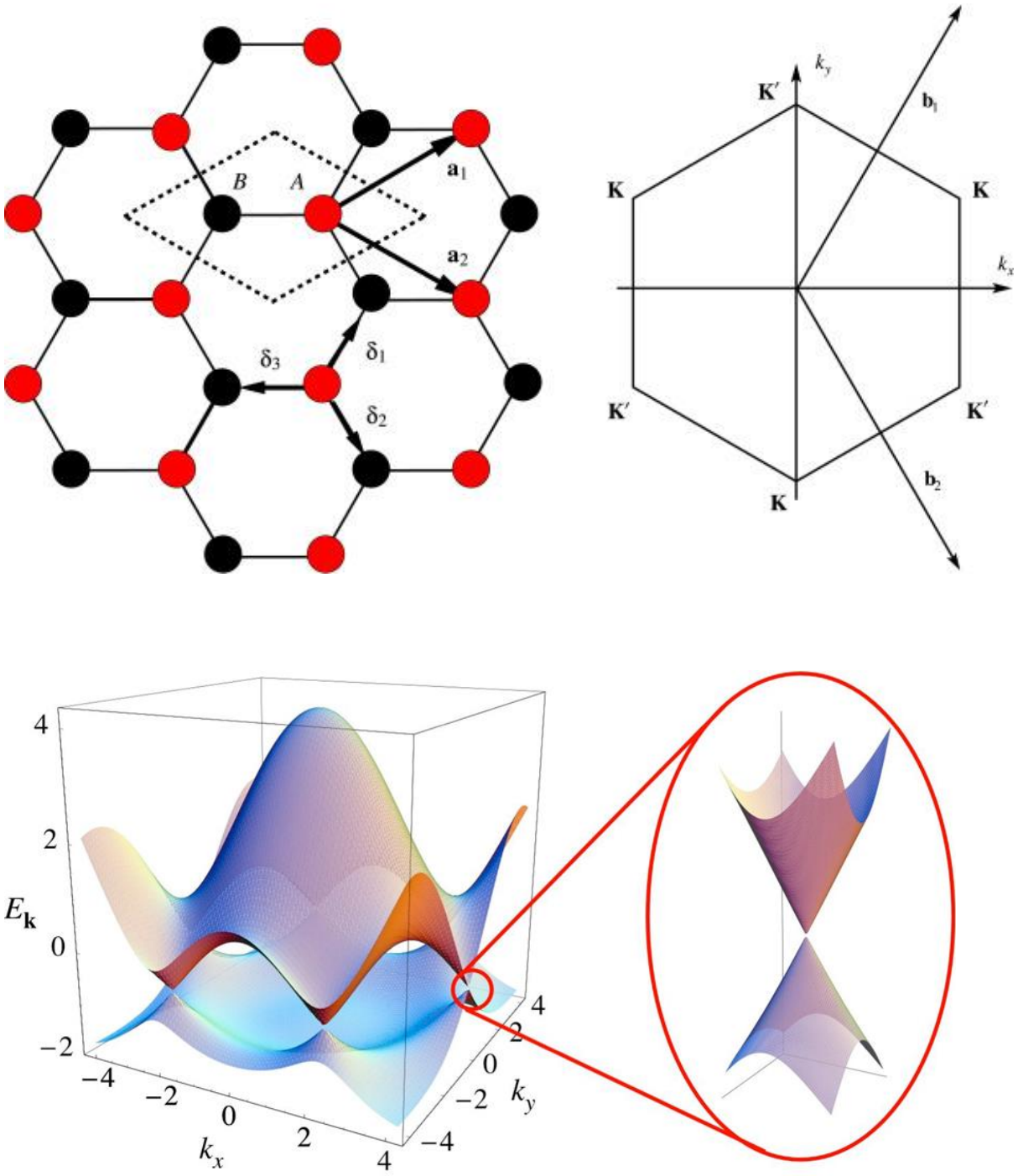

Figure 34: Graphene is composed of a hexagonal lattice (a) with two inequivalent atoms, A and B, as shown in (a) along with the lattice vectors and bond lengths. (b) The Brillouin zone of graphene is also hexagonal with inequivalent vertices called the K and K' points which alternate. The dispersion relation of graphene is linear at the Dirac points, (c) the intersection of the valence and conduction band form Dirac cones with different chirality for the different valleys. Figure adapted from reference [212]

45 (a and b). As shown in figure pronounced quantum Hall plateaus can be clearly seen but however do not occur in the expected sequence observed in traditional 2D materials. In graphene the Hall plateaus correspond to half-integer values as indicated by the first plateau which occurs at $2e^2/h$, with a Hall sequence of $(4e^2/h)(N + ½)$. This results in a ladder of equidistant steps in in the Hall resistivity which are not interrupted when passing through zero (figure). These features are a result of the Landau quantization and in graphene have been claimed to be within an experimental accuracy of ≈ 0.2% [120]. The half-integer QHE in graphene has been theoretically investigated by a number of groups [121,122] and have been related the effect to subtle properties of massless Dirac fermions such as the existence of both electron- and hole-like Landau states at exactly zero energy [123]. Such features are a direct consequence of the Atiyah-Singer index theorem found in quantum field theory and the theory of superstrings [124]. As the charge carriers in graphene behave as massless relativistic particles and move with little scattering under ambient conditions signatures of the Quantum Hall effect have been observed even at room temperature at fields surprising low for such a phenomenon. The survival of the quantum Hall effect to ambient temperatures has been attributed to the large cyclotron gaps characteristic of the Dirac nature of fermions in graphene. In addition to the large cyclotron gap, there are a number of other factors that allow for such quantum phenomena to persist up to such high temperatures; graphene devices show very high carrier concentrations (up to 1013 cm^{-2}) with only single 2D subband occupation, an essential ingredient to fully populate the lowest Landau level. This feature is in contrast to other 2D systems such as GaAs heterostructures which can be depopulated in moderate magnetic fields or exhibit multiple subband occupation which causes a reduction of the effective energy gap. Additionally, the mobility of electrons in graphene is exceptionally high and does not change much in a large temperature range from liquid-helium to room temperature. Another signature of the Dirac nature of the fermions is that single layer graphene devices have a zero field conductivity that never falls below a well-defined value which is independent of temperature at least between 4 and 100K. Single layer graphene devices have shown a minimum resistivity of ~ 6.5 KΩ within an experimental error of ≈15%. This minimum resistivity was found to independent of their mobility that can vary by a factor of 10. This minimum value has been related to $h/fe^2 = 6.45$ kΩ where h/e^2 is the resistance quantum and f is the quadruple degeneracy factor determined from the Hall Effect measurements. The effect is thus different from the conductance quantization observed in other quantum transport experiments and is an intrinsic property of electronic systems described by the Dirac equation. This feature is due to localization effects being strongly suppressed for such relativistic charge carriers.

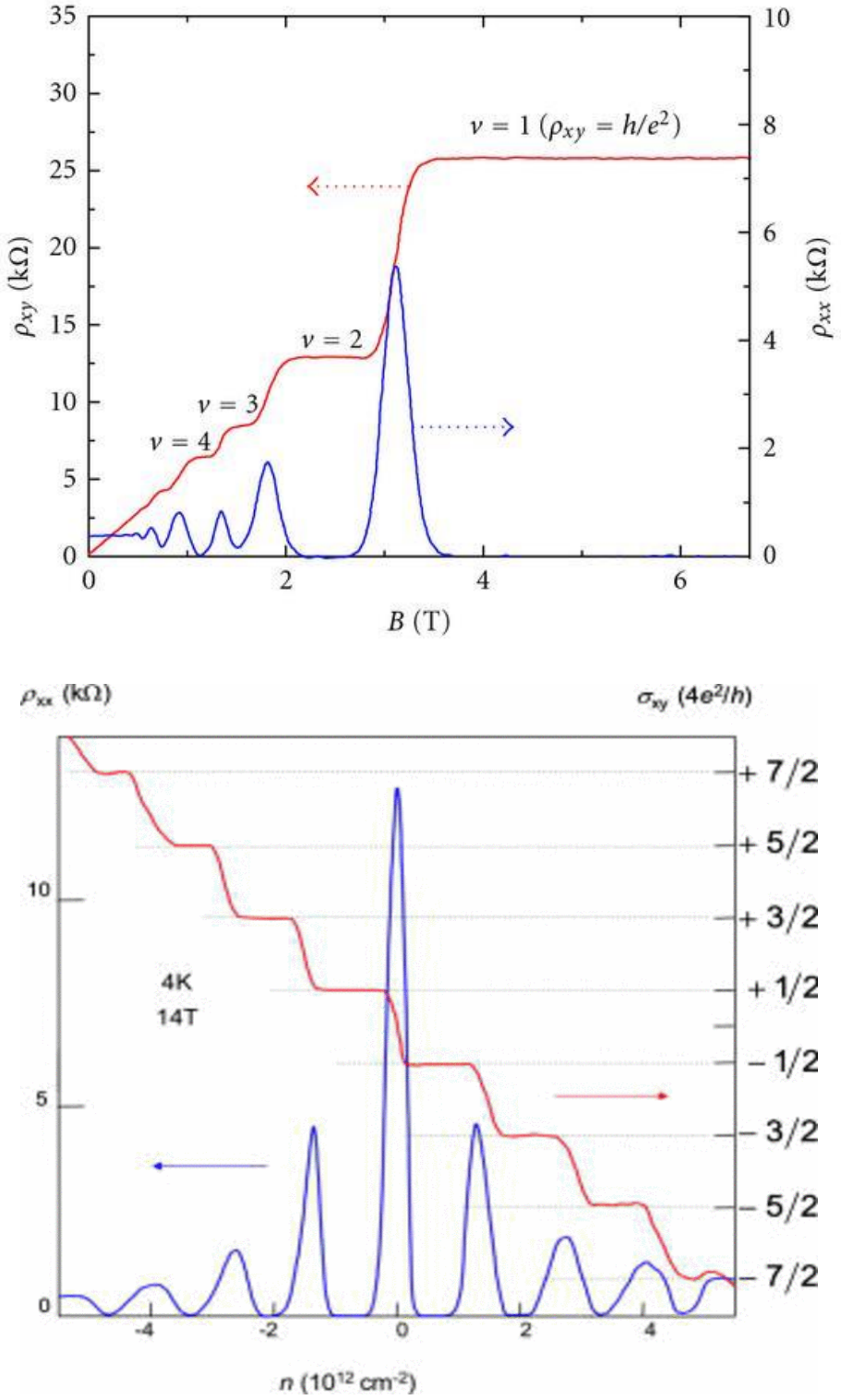

Figure 35 (a) Both the longitudinal and transverse resistivity show the effects of the Dirac nature of fermions on the Landau quantization, i.e. the half-integer Quantum Hall effect. The longitudinal and transverse resistivity as a function of the carrier concentration, the steps in the transverse conductivity clearly show the half integer dependence. Figure from references [119, 120]

The physics regarding quantum interference effects probed at low magnetic fields has also generated as substantial amount of interest in graphene research. This again is due to the Dirac nature of the fermions. Because of the chirality and Berry phase of the carriers there are strong restrictions on the type of scattering events that can occur for electrons within the same or different valleys in the band structure. For intravalley scattering events the conservation of helicity eigenvalues prevents backscattering, leading to the so-called Klein paradox [125]. On the other hand backscattering events can occur for scattering between different valleys (intervalley scattering), this is because the change in sign of the momentum is accompanied by a change in the helicity for such an occurrence. This effectively means that very specific scattering events in real space lead to the observation of either the Weak localization (WL) or weak anti-localization (WAL) effects. Long ranged scattering potentials such as ripples in the graphene sheet, dislocations and charged impurities are responsible for intravalley scattering favouring the WAL effect whereas short-ranged potential (point like) scattering events due to adatoms and vacancies lead to intervalley scattering and are observed as the WL effect. This allows for the determination of microscopic properties of graphene devices related to the disorder of the samples used. The observation of the WL effect is related to quantum interference between electrons with time reversed paths, thus the breaking of time reversal symmetry by application of small magnetic fields can be used to study such phenomena. The weak anti-localization effect was also shown to be heavily supressed by trigonal warping at energies near but away from the Dirac point. The trigonal warping is a causes an asymmetry in the band structure in adjacent K and K' valleys, as the effect will have opposite sings in the different valleys, this leads to suppression of the WL effect. Indeed both WL and WAL have been observed and extensively in graphene [126]. In figure the magnetoresistance of single layer graphene devices fabricated using chemical vapour deposing (CVD) synthesis route is demonstrated. The weak localization effects can clearly be observed by the sharp negative magnetoresistance. CVD synthesized graphene be thoroughly been studied in graphene as the CVD route allows for larger scale growth [127]. However the CVD route in general leads to graphene with a lower mobility and a higher defect density. There has however been great progress in this field and high quality large scale graphene has been demonstrated, this synthesis route also offers the possibility of substitutional "doping" the graphene with elements such as nitrogen and boron [128,129].

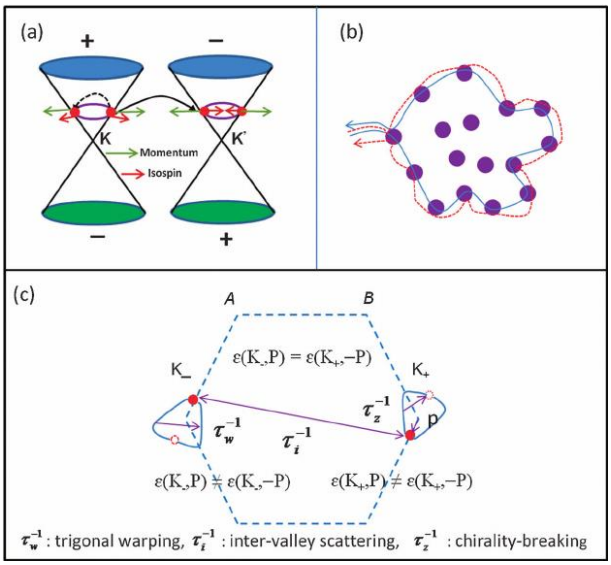

Figure 36 (a) scattering events can occur either due to inter or intra-valley events, whichever is dominant in the device under test can be determined through magnetoresitance measurements. (b) The WL effect is a result of interference between particles with time reversed paths, this is because, in the absence of strong spin-orbit coupling, in such an interference path both wavefunctions pick up the exact same phase and the inference is constructive. Valley warping away from the Dirac cones leads to suppression of the weak anti-localization effect. Figure obtained from reference [126]

6.2 Effects of strain on the transport properties

Although graphene has many interesting and valuable properties such as exceptional mobility and carrier concentrations being a semi-metal it suffers in terms of one essential electronic property required for conventional electronics, a band gap. Using electric gates, semiconducting systems can easily be controlled, this is however not possible in graphene. This limitation has however not hampered research into the utilization of graphene in semiconducting technologies. Much research has been and currently is being directed at novel ways of inducing a gap in the band structure. There are currently at least three main routes that have been proposed:

- Doping and chemical modification of the graphene sheet.
- Etching graphene into narrow ribbons.
- Strain engineering.

The first route is generally restricted to CVD synthesized graphene as the dopants can be introduced during the synthesis [128,129]. The substitutional doping of both nitrogen and boron into the graphene lattice has been extensively studied theoretically and has experimentally, to some degree, already been demonstrated. Although this type of synthesis can lead to opening a band gap, Nitrogen doping leads to n-type doping where boron doping to p-type material, such systems have a drastically reduced carrier mobility and generally exhibit higher levels of disorder thus limiting their usefulness in electronic applications [130]. Etching graphene into narrow nanoribbons has already lead to some interesting findings, the different types of edges in the graphene, i.e. armchair or chiral, as well as the width of the graphene channel influences the transport properties and can open a gap [131]. However, the fabrication of graphene ribbons, generally around 10 nm in width, in a controlled manner to allow for the exact edge morphology can be difficult.

The effect of strain on the transport properties of graphene has been theoretically investigated and shown to lead in addition to a band gap opening, exotic transport phenomena such as rare superconducting phases [132]. It has also been shown that local straining of the graphene lattice acts on the electrons in the same way as the application of magnetic fields, in other word straining can induce fictitious pseudo-magnetic gauges. The strength of such pseudo-magnetic fields can be extremely high, some reports of up to 300 T [133] .

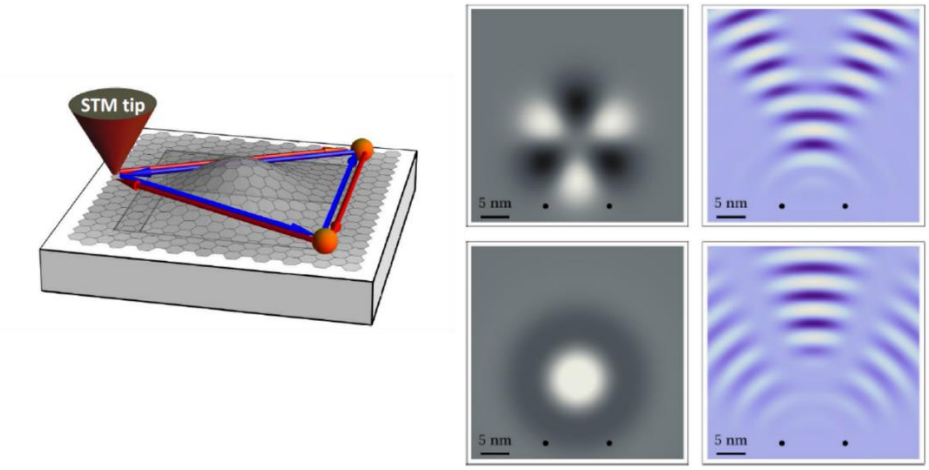

Figure 37 A novel method for measuring the pseudo-magnetic fields in strained deformaed graphene using the Aharonov-Bohm effect. As different strain potentials lead to different pseudo-field strengths (b and c respectively show field distribution for in plane and out of plane deformations), electrons traversing paths around the deformation and deliberately placed impurity scattering centres will exhibit different interference patterns which can be measured using the STM tip. Figures adapted from reference [134]

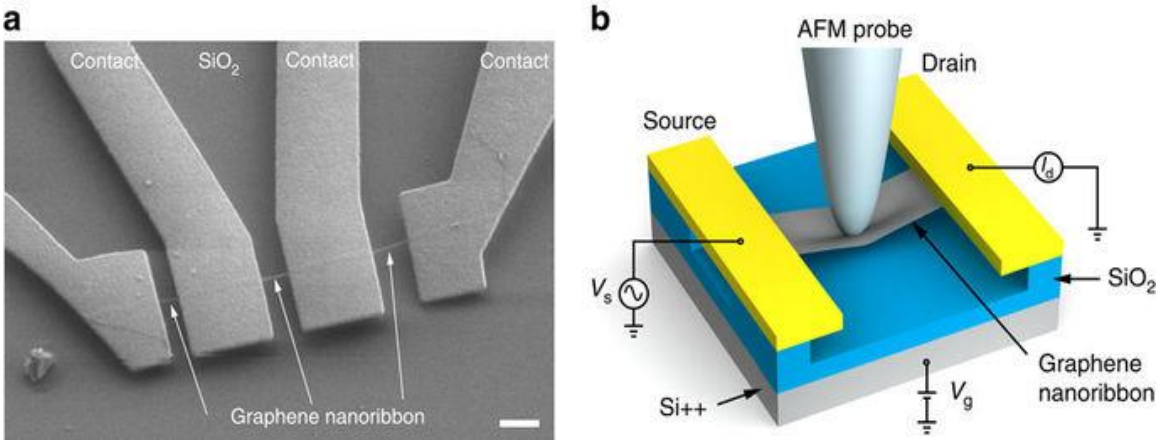

Figure 38 Electro-mechanical devices constructed from suspended graphene nanoribbons. AFM probes can be used to locally apply strain in an controlled manner using peizeoelectrical mechanicals parts in order to tune the electronic properties of the graphene channel. Figures taken from reference [135]

The formation of such large fields has serious consequences on the electronic properties, the formation of Landua levels along rippled regions is well documented [133]. One particularly interesting method for measuring strain in deformed graphene is through the observation of the Aharonov-Bohm effect using scanning tunnelling microscopy [134]. This is shown in figure, where graphene regions of different strained profiles give pseudo-magnetic field distributions and will thus lead to different interference patterns of electrons traversing the circumference of the deformation and being knocked back off scattering centres. This effectively leads to oscillations in the electron density which can be easily measured using the STM tip. Different gauge strengths will lead to different AB oscillations. Although this experiment requires some very technical specifications such as placement of scattering impurities and creating the deformation in a controlled manner, it has been argued to still be feasible but has however not yet been experimentally verified. Other avenues of strain engineering have employed the fabrication of elaborate devices constructed from suspended graphene ribbons and the application of a deformation from the tip of an AFM or STM probe. Such devices allow for a more controlled method of applying strain and thus modifying the electronic properties of the graphene conduction channel. They are however not very practical for electronic device fabrication. Such a device [135] is shown in figure where the graphene can be seen suspended between the gold electrodes. In such devices the electromechanical response of both single and bi-layer graphene samples were studied. For the single layered graphene device, it was observed that the strain induced an increase in the resistance, this related to a change in the Fermi velocity with straining. Such deformation were however not able to open a spectral

or a transport bandgap larger than 4 meV for straining under 5%, this was in agreement with theoretical predictions [136]. The electromechanical response of bilayer graphene however showed much richer phenomena such as oscillations in the resistance which were explained in terms of quantum interference effects between layers of the bi-layer system. These measurements were carried out at room temperature and thus again highlight quantum effect at ambient temperatures in graphene systems. The bilayer-based electromechanical device thus shows prospects for studying symmetry breaking in graphene as well as electronic interference phenomena at room temperature.

Due to the richness of physics as well as the potential for device applications reliable methods for the introduction, measurement and control of strain in graphene is currently a very active research topic with much scope for improvement as well as introducing novel methods for such strain engineering.

Chapter 7

Nano-scale deformation in graphene through Raman Annealing

7.1 Phonon dispersion in graphene

An essential characterization technique used in analysing a wide range of properties of carbon materials is Raman spectroscopy [137]. As mentioned in the previous chapter, there is an intimate relationship between the mechanical and electronic properties and thus Raman spectroscopy which probes phonon as well as phonon-electron correlations due to lattice vibrations is an exceptional tool for understanding many phenomena in graphene. Raman spectroscopy has been shown to not only be a potential candidate for non-destructive and quick characterization of single layered graphene but is also able to determine the number of layers as well as orientation of layers in thicker samples [138]. Due to the symmetry of a graphene sheet there are six of these phonon dispersion modes related to the possible vibrations. Of these, three are acoustic (A) phonon modes and three are optical (O) phonon modes. Each of these bands consists of one out-of plane (o) phonon mode and two in-plane modes (i), of which one is longitudinal (L) and one transverse (TO). The optical phonons in the zone-centre (Γ point) and zone edge (K and K' points) of the reciprocal lattice are the modes of particular interest as these can easily interact with electronic wavefunctions.

The most prominent band in ordered carbon material is the G band at 1580cm^{-1} which is associated with iTO and LO phonon modes, this band is a result of a first-order Raman scattering process due to in-plane vibrations of sp^2 carbon atoms. The 2D band situated at wavenumber of 2670cm^{-1} is the second order overtone of the D band. Both the 2D and D bands are a result of second order processes involving two phonons, these processes are known as double resonances. The 2D band is associated with two iTO phonons near the K points whereas the D band is a result of one iTO phonon and a defect, this mode corresponds to the breathing mode of the six atom ring and requires the presence of a defect to be

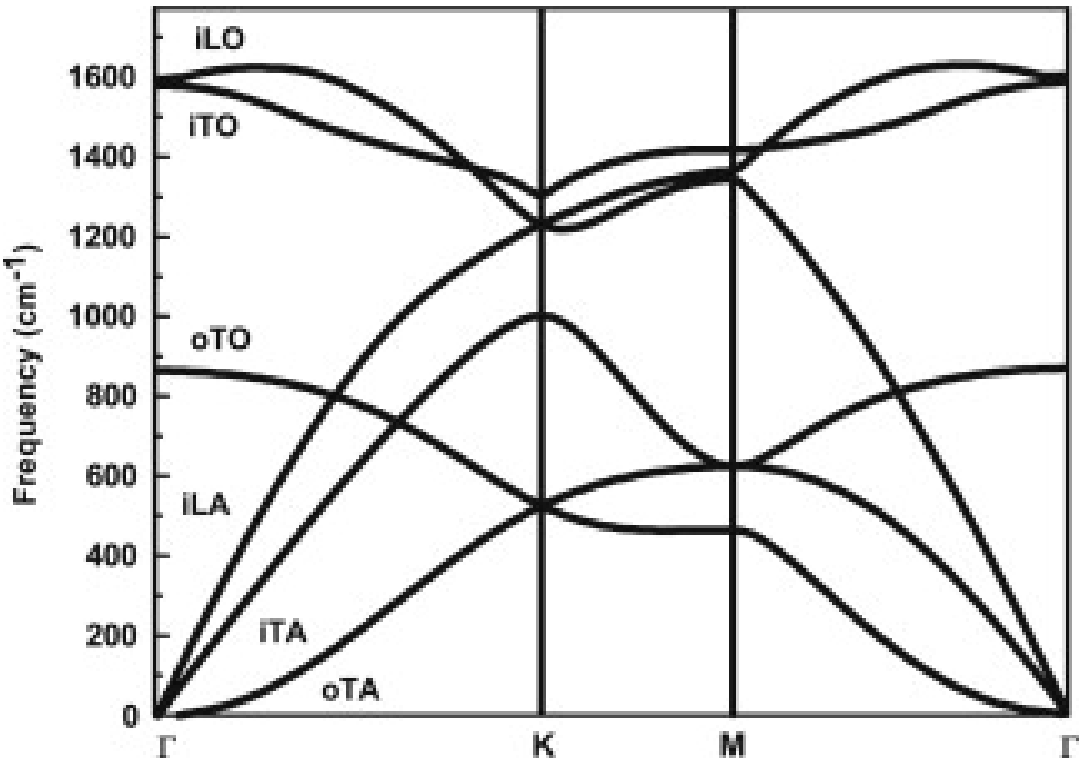

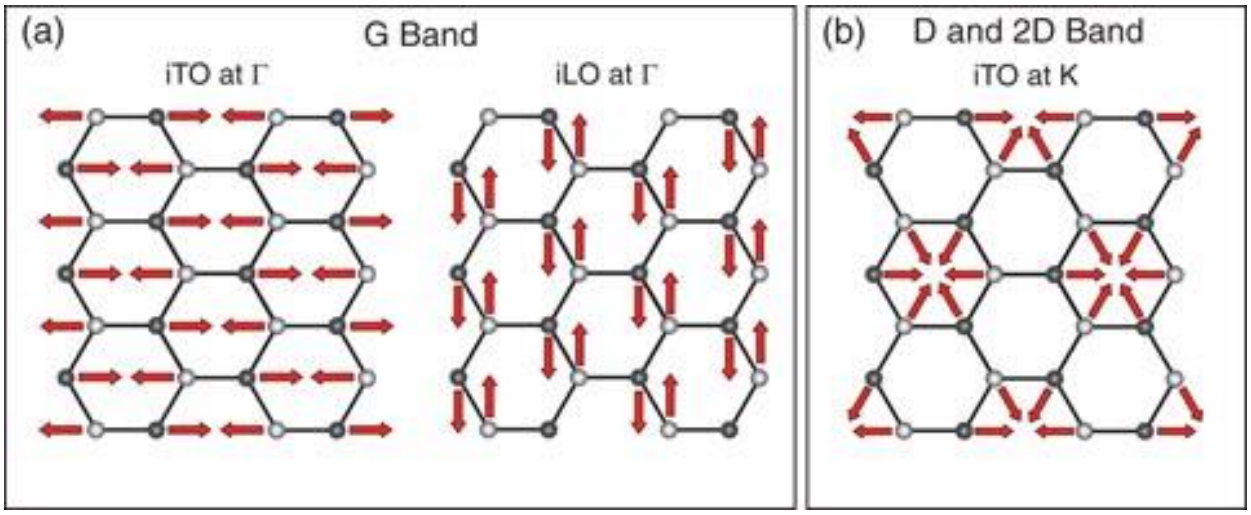

Figure 39. Phonon band structure of graphene. Some notable implications of the six fold symmetry is the van Hove singularities observed experimentally. (b) Graphene lattice with arrows indicating the phonon vibrational modes related to various phonon modes. Figure from references [213,214]

activated. Thus, only in a disordered sample or along the edge of a graphene flake, will the disorder induced D-band be observed.

This D band shows a strong dispersion with laser excitation energy due to Kohn Anomaly at these points. As the 2D band originates from a two phonon double resonance process, it is closely correlated to the band structure of graphene layers [139]. The 2D band features are dispersive with the number of layers of the graphene flake being probed. This dependence on the number of layers can be used to determine the number of graphene layers in few layer graphene system [140].

A double resonance process can also occur as an intravalley process, such a mode is sometimes referred to as the D' peak and is centred at 1625 cm^{-1} and is induced by certain types of disorder. This band has been observed in randomly oriented bilayer graphene due to a rotational-induced intervalley double resonance effects [141]. There is also a small peak (D + D') located at approximately 2450 cm^{-1} which is believed to originate from a combination of in-plane Longitudinal acoustic phonons and in-plane transverse optical phonon modes and is also sensitive to the number of layers in the sample [141].

The main difference between the Raman features of single and multi-layer graphene is the ratio of the 2D to G bands this is because as the G band increases roughly linearly with the number of graphene layers increases [142]. Figure 50 (b) gives a typical Raman spectra of a single layer graphene (SLG) sheet on a 300nm thick SiO2 layered Si substrate. The Raman spectra of samples used in this study were recorded with a WITec CRM200 Raman system with a double-frequency Nd:YAG laser (532 nm)as excitation source. The laser power at the sample is below 0.1 mW to prevent laser-induced heating and damage. Using Raman spectroscopy, graphene layers can be correctly identified on any substrate [143].

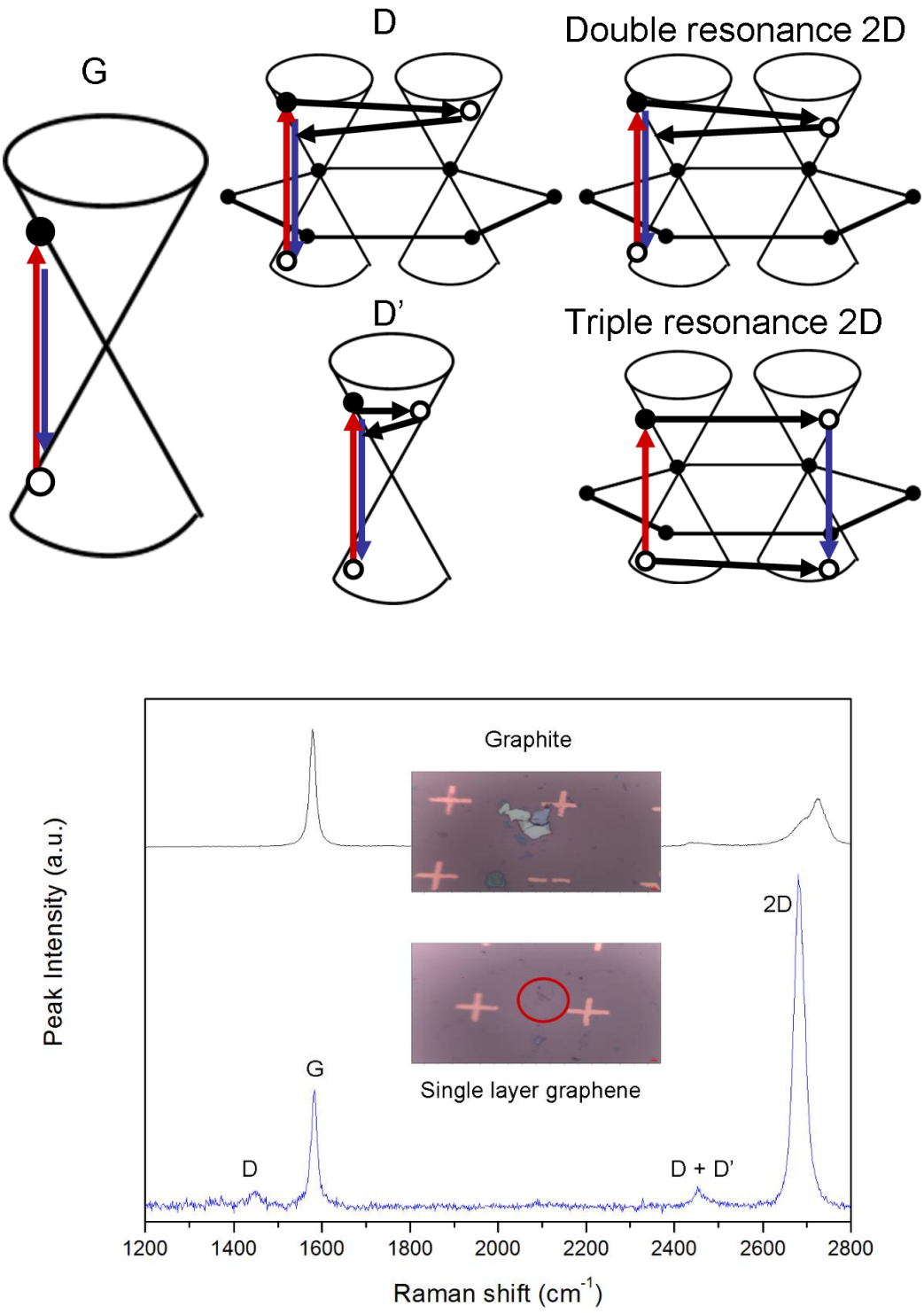

Figure 40. The phonon modes are intimately related to the electronic spectrum in graphene. This allows for a range of electronic transitions to be monitored through Raman spectroscopy. (b) The Raman spectrum of graphite and graphene are markedly different, important feature of the Raman spectrum of graphene is the pronounced 2D band at 2700 cm^{-1}

7.2 Effects of disorder on the Raman spectrum

As stated above Raman spectroscopy is a valuable means of analysing disorder in graphene samples [144]. The main features of disorder in the Raman spectrum are:

- Appearance of the D peak and increase in the I_D/I_G ratio
- Broadening of all peaks full width half maximum (FWHM)
- Appearance of the D' peak at 1620cm^{-1}
- The appearance of the D + D' peak
- The eventual merging of the G and D' peak resulting in a single up-shifted band at approximately 1600 cm^{-1}.

One of the most important and widely used features of disorder is the I_D/I_G intensity ratio. This analysis was first given by Tuinstra and Koenig [145] and has since enjoyed much success. It has been shown that the I_D/I_G ratio is inversely proportional to the defect free crystal size or coherence length, i.e. the distance between defect scatterers and is described by the following equation [145]:

$$\frac{I_D}{I_G} = \frac{C(\lambda)}{L_a} \qquad (39)$$

The D peak only occurs near a defect or edge and thus depends on the length between defects (L_D) whereas the G band intensity is proportional to the area sampled (L_a^2). The D peak intensity is proportional to the number of defects located in the sample area (L_L). This then gives that $I(D) / (L_L L_D)^2$ This means that for an area probed by a laser with a spot size of LL, there will be on average $(L_L L_D)^2$ defects in the sampled area. At high disorder levels however the Tuinstra and Koenig relation breaks down.

Raman conformal mapping of graphene has been frequently used in the analysis of material quality over the surface area of graphene devices using this knowledge of the D and G peaks. This is quite necessary as graphene samples, particularly CVD synthesized samples, may not be homogenous in terms of disorder, layer number and stacking order throughout the flake. These variations can lead to large deviations in device properties and are obviously unwanted. Thus in order to better characterise the individual graphene devices, Raman spectroscopy mapping is frequently used. This is achieved by taking multiple Raman spectra of the sample as one scans over the flake, this allows for the Raman signal to be mapped over the sample area giving a much better idea of the quality of the graphene flake in question. Figure shows a map

of the G-band intensity while the last image is a map of the ratio of 2D/G band intensity. From the colour mapping it was possible to determine that this specific graphene flake consisted out of two layers, but some region to the left of the material (indicated as being much lighter in colour) being only single layer. The dark regions of the mapping show that a third graphene layer at the bottom left edge of the material occurs as a small folded region. When fabricating a device it will be essential to keep all these details in mind as it is important in having a graphene device which is consistently thick as the electronic properties of single to multilayered graphene vary. This method of characterization has the obvious application in determining the suitability of any arbitrary graphene flake as the entire flake can be mapped showing disordered regions as well as regions which may have additional layers accidentally left over them. It should also be noted that the mapping and height determination is in agreement with the AFM measurement of the same graphene flake.

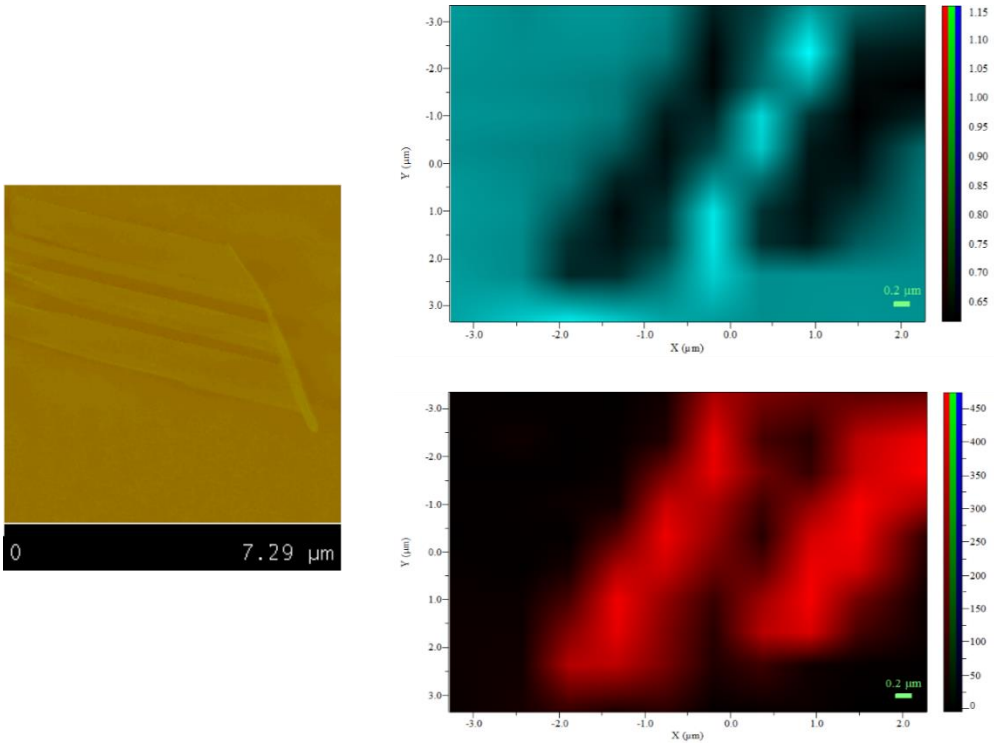

Figure 41 (a) AFM image of a graphene flake with unusual geometry, (b) Raman conformal mapping can help determine some of the properties of such flake through mapping the I_D/I_G as well as (c) the D peak intensity.

7.3 Effects of strain on Raman Spectrum

In addition to influencing the electronic properties of graphene, straining can lead to pronounced features in the phonon modes and hence the Raman spectrum as well [146]. However as the Raman peaks of graphene are influenced by many different properties of the individual flake the effects of strain can be overshadowed or masked and thus difficult to disentangle from other influencing factors, most notably doping. For effective strain engineering probed through Raman spectroscopy it is thus important to have a clear understanding of such effects when trying to understand the level and effects of strain on the specific flake or device. Luckily this area of research has received a large amount of attention and a vector decomposition of peak properties has allowed for the separation of doping and straining effects [147]. This is achieved through the analysis of the 2D and G peak frequencies, this is demonstrated in figure taken from reference, where the distribution of points was obtained from Raman spectroscopy of single layered graphene devices where the shifting of the Fermi level as well as the strain applied to the system could be precisely controlled. The shifting of the data points in this 2D/G map are due to the relative sensitivity of the two peaks to either doping or straining, and thus allows for a clear analytical method of measuring strain in graphene devices.

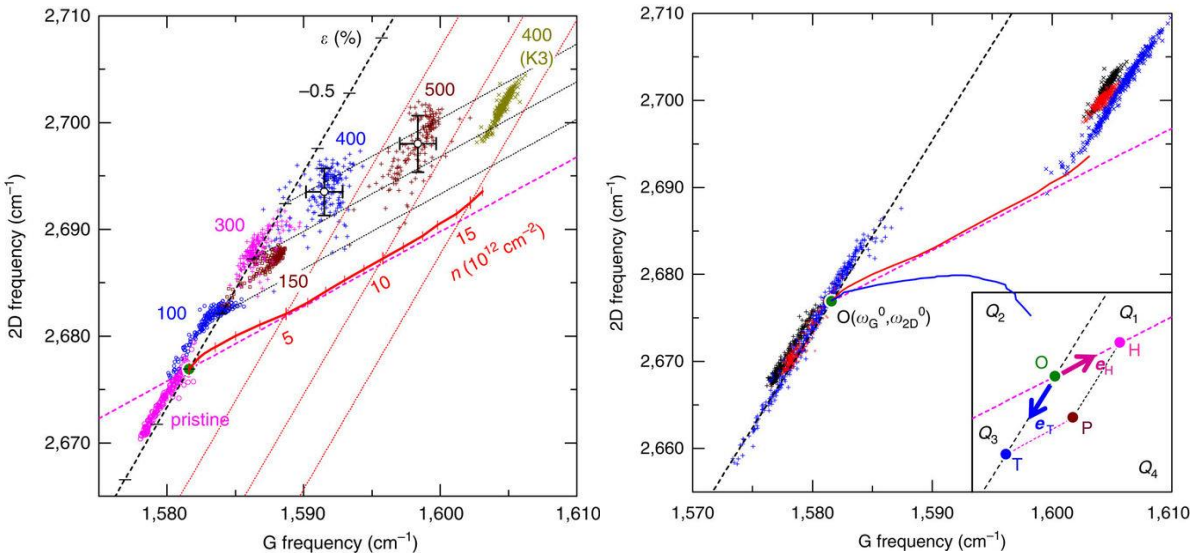

Figure 42. The 2D and G phonon modes are most sensitive to applied strain, thus by tracking the dispersion of these modes with relation to each other the effects of doping as well as strain can be disentangled from each other. Figure from reference [147]

7.4 Raman annealing

Due to its ease of operation, non-invasive nature and the strong sensitivity to carbon, Raman spectroscopy is an ideal tool not only for the detection of phonon properties but also for the modification of graphene as well. The effect of laser irradiation of graphene is well documented [148]. Studies at high laser power have demonstrated the possibility of burning holes into graphene as well as causing deformations in graphene regions suspended over fabricated trenches [149]. The response of graphene to femtosecond laser irradiation has also been investigated [150], here it was established that graphene has an exceptionally high single-shot damage threshold (31012 mJ/cm^{-2}) and that structural changes such as folding of the graphene sheet can occur. In this chapter we show the formation of nano to micron size deformations at moderate powers (< 60 mW) well below the damage threshold. As mentioned before the creation of strained regions in graphene can be of significance to the electronic properties due to the formation of psuedomagnetic fields which have major consequences for the conductivity in the strained region [133].

Here we demonstrate the utilization of Raman laser annealing for the in situ formation of strained. We determine the dominant effects, i.e. either strain or doping related, leading to position shifts of phonon modes of the treated area. The deformations can lead to pseudomagnetic fields as high as hundreds of Tesla, comparable to other reports on deformations in graphene.

Graphene samples used in this study were prepared using the micromechanical scotch tape method [119] and transferred to SiO_2 substrates. Optical microscopy and atomic force microscopy were used as complimentary techniques for the determination of the height and morphology of the deformations formed in the study. Raman spectroscopy at an excitation wavelength of 514.5 nm was used to determine the number of layers of the sample as well as the initial state of disorder of the respective samples. The laser induced deformations of the graphene sheet is observed after a laser exposure cycle similar to the isochronal annealing technique used in semiconducting research. The treatment essentially involves laser exposure of a spot on the graphene sample to a range of different powers ranging from 2 - 60 mW for a minute each. The Raman spectrum of the sample is then taken at a power of 0.33 mW between each treatment step in order to prevent further annealing during this data acquisition step. AFM imaging is carried out on the samples in order to determine the effect of the annealing on the surface of the sample. The most prominent observation is the formation of bubble-like

structures in the graphene sheet, these structures are localized at the area exposed to the higher powers of the laser beam. Figures 53 (a-f) show a compilation of data obtained during such an annealing procedure. Figures 53 (a) and (b) show the Raman intensity mapping of the local strained region. The yellow coloured circle in (b) is an indication of where the splitting of the G-peak occurs after exposure of 28 mW, the comparative figures show that the intensity of the second G-peak (G+) is only measured at the laser treated spot. Figure 53 (c) is the AFM image of the graphene sample before exposure to the laser beam. Figures (d) and (e) show the AFM images of the same graphene flake during the annealing process, the formation and growth of the deformed area due to laser exposures can clearly be seen.

The size of the bubble was approximately 1.4 μm in diameter after the final annealing step. We also observed that the bubbles only formed after exposure from a lower limit laser power (20 mW). The size of the bubbles are initially 100 nm in diameter and gradually increase in size upon subsequent laser exposures. The shape of the bubbles remain circular as they grow and the height of all samples were consistency measured to start at around 2.5 nm and increase to a maximum height of 3 nm as measured through AFM.

As mentioned above, nano-scaled bubbles have demonstrated the existence of pseudo-magnetic gauge fields. The strength of the field is related to the height and width of the bubble or deformed area as well as its curvature. The deformations observed here have a circular structure, somewhat blister like, with flat (sometimes rippled) tops and sharply curved edges. This would indicate that the largest degree of straining occurs at the circumference of the blisters and this is where the strongest gauge fields would occur. This type of circular or ring geometry may be useful for testing the Ahronov-Bohm effect described in a previous chapter for determining the interference effects and oscillations in the density of states through STM measurements [134]. Raman spectroscopy is used to extract more information about these deformations.

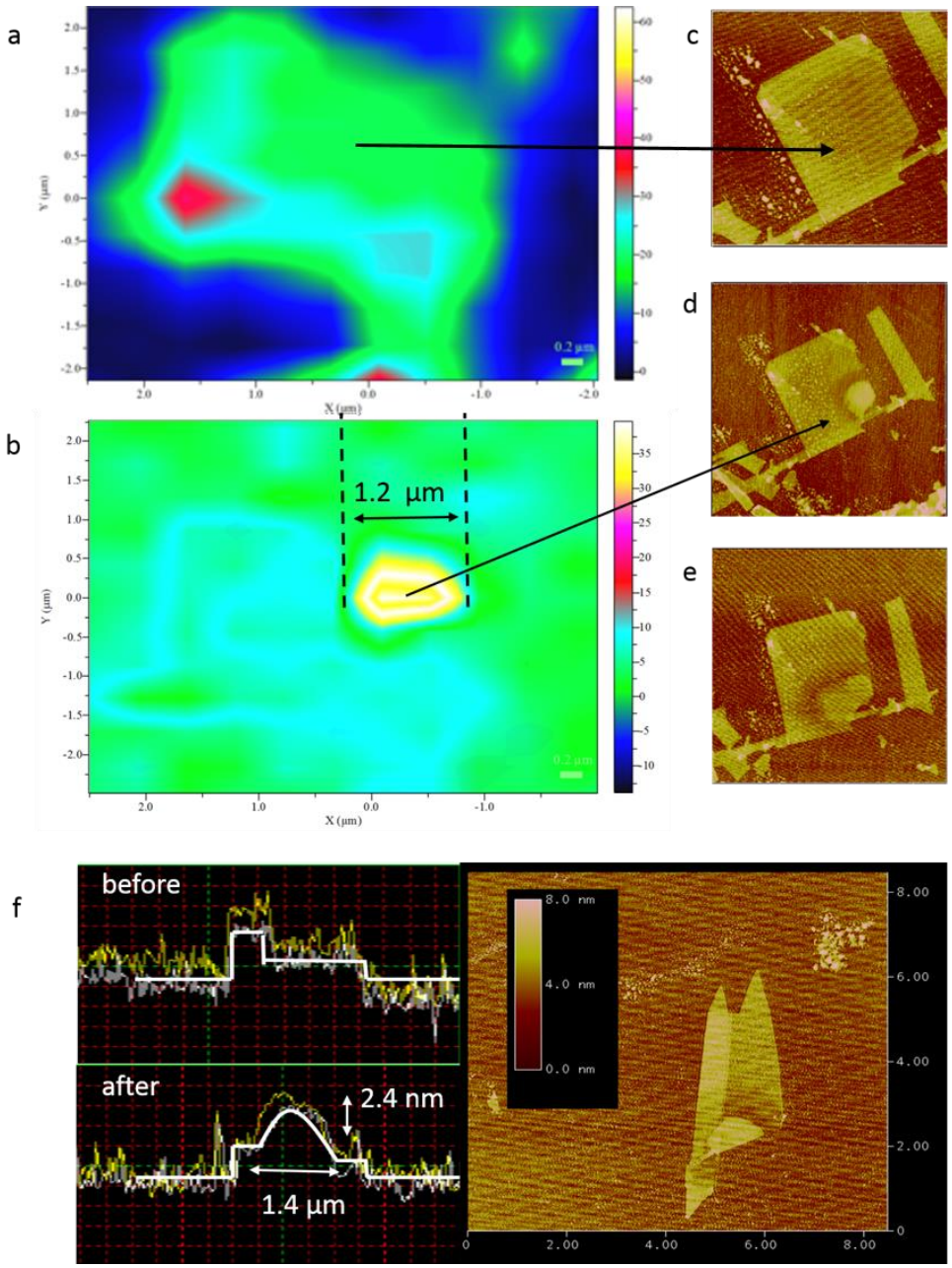

FIG. 43. Raman mapping of a single graphene flake showing the spatial distribution of the (a) untreated G-peak intensity and (b) the higher frequency Gþ mode intensity resulting from the laser annealing. (c) The AFM mapping of area of 66 lm before and (d) after the laser treatment at 28 mW; as can be seen, the treatment has the effect of causing a protrusion or bump in the graphene layer, (e) the size of the bump continues to grow after additional laser treatments up to 57 mW. (f) AFM image of a different sample; the height of the deformed area determined through AFM measurement was found to be 2.4 nm. AFM colour scale bars range from 0 to 10 nm.

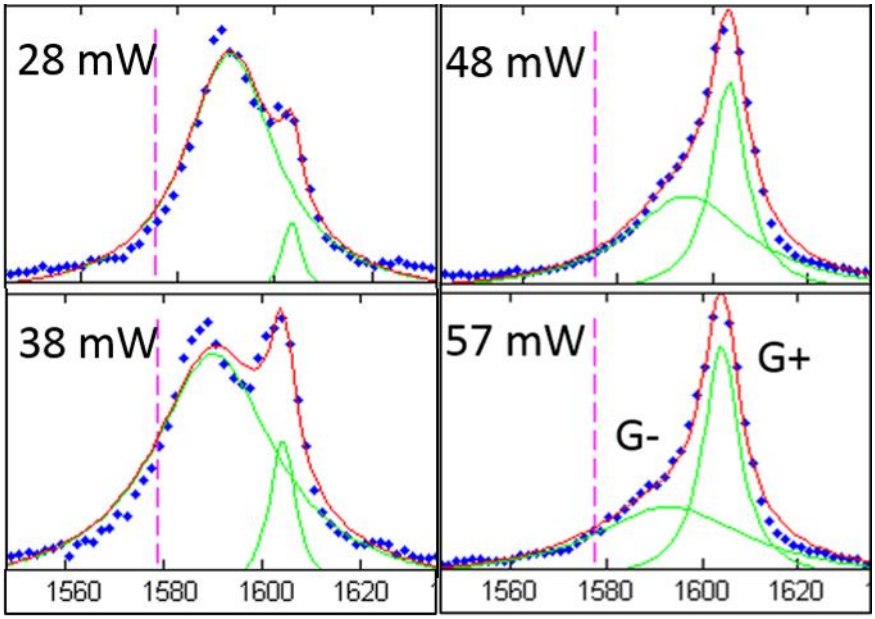

Figure 44 The evolution of the Raman spectrum with increasing laser power is shown. The G-peak is shifted and splits after a threshold power of 21 mW, and the two component modes behave differently upon subsequent laser treatment. The dots represent data and the lines are the Lorentzian fits.

Figure44 shows the splitting of the G-band, a well-known signature of strain [151], as well as the shifting of the two modes during subsequent laser exposures. As shown above, the G+ mode starts out with a small intensity but grows rapidly during the laser treatment, however the lower frequency G- mode decreases in intensity and exhibits a broadening (increase in its FWHM). As doping, due to substrate interaction or adsorbents [152], can cause similar features in the G-band a deeper investigation using the relative properties of the G and2D peaks is conducted, this is in-line with the technique described in ref [147]. There is was demonstrated that there exists a linear relationship (with gradient of approximately 2.2) between the change in 2D and G-band positions of pristine mechanically exfoliated graphene. By analysing the deviation of the data points from this linear relationship it is possible to extract the dominant contribution causing the observed peak shifting (whether resulting from strain or doping). The data points for our system are shown in figure 55 (a and b). Here it can be seen that the data points before and after the G-peak splitting at 21 mW show pronounced shifting from the initial positions. The best fit straight line to the data points before the peak split has a gradient of approximately 1.02. This value is below what has been previously reported [147] and indicates that even before the peak split there is coexistence of strain and doping effects most likely due to substrate interaction. The net observed effect is consistent with peak shifting related to

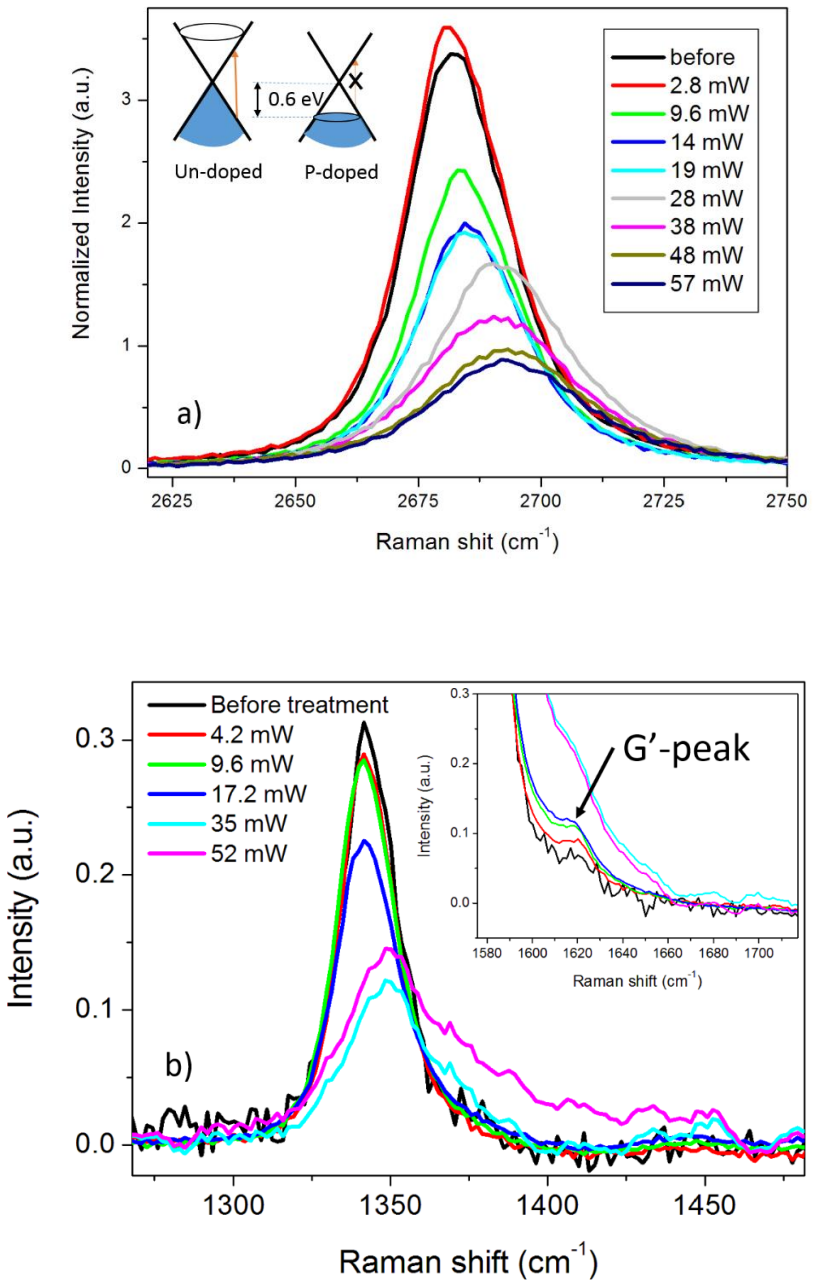

FIG. 45. The change in the (a) Raman 2D and (b) Raman D peak intensities normalized with respect to the Raman G-peak as a function of laser treatment power. The decrease in these peaks with respect to the G peak is attributed to quantum interference effects due to Pauli blocking (inset (a)), which causes the decrease in resonant phonon modes. The inset in (b) shows the G0 peak which is a strong indicator of disorder. This peak appears to remain unaffected during the laser treatment.

compressive straining up to 0.5%. The splitting of the G-peak is not expected to be a result of curvature as only uniaxial curved studies have shown this effect [153].

As can be seen in figure 54 and 55 (b) the G+ mode shows a large redshift of 25 cm^{-1}. The vector decomposition analysis indicates that this shift is due to p-type doping which is likely due to water and oxygen molecules being released from the substrate and causes the deformation during the laser treatment. Assuming a linear behaviour between the position of this G-mode and the Fermi level it is possible to calculate the level shifting in the band structure related to the shift in peak position (25 cm^{-1}). We also note the slope of the best fit straight-line corresponding to the G+ mode indicates that the wavenumber shift of this mode is largely due to doping and less likely from due to further changes in strain.

The lower frequency mode however shows a different behaviour with a best fit straight-line slope of 0.54. This indicates that this mode is less strongly affected by doping and here the shift in the Fermi level is calculated to be 0.24 eV. The strain variation of the peak positions of the G- mode is similar to that of the G+ mode indicating that most of the changes due to straining occur before the peak split (= -0.5%).

As there is a clear difference in the response of the G modes during the annealing experiments, additional investigations looking at the FWHM of the respective peaks. The G-peak FWHM are analysed with respect to the position shift of each G-peak, this is shown in figure 55 (a). Again the data set can be separated into three regions, corresponding to before the peak split and then the trends of the two modes after the peak split. It is observed that the peak shows a decrease in the FWHM which is a strong indication of p-type doping [154]. This is consistent with the interpretation of the position shifts given above. After the peak split however we note that the two modes behave quite differently.

At higher laser power annealing there is a pronounced difference in the FWHM characteristics of the two G-modes. The higher frequency G+ mode continues to show a downward trend, or narrowing of the FWHM whereas the lower frequency G- mode shows a strong increase in the FWHM with increasing laser power. This is quite significant as an increase in the FWHM of the G-peak is usually associated with an increase in disorder. However as the other hall mark features of disorder are not observe, viz. an increase in the I_D/I_G intensity ratio and increase in G'-peak intensity, see figure 56 (a and b). In addition, the 2D-peak decreases in intensity with respect to the Raman G-peak intensity. This effect can again be related to doping and has been shown to be a result of Pauli blocking of the resonance modes and thus leading to a net

constructive quantum interference of the Raman G mode, increasing the G-peak intensity and decreasing the ratio. This is further corroborated by the I_D/I_G intensity ratio behaviour which follows the same trend. This study thus clearly demonstrates a method for the formation of nano to micron scaled deformations of a graphene sheet using a non-destructive technique that also allows for doping. This method can be used in patterning of strain engineered graphene devices I a controlled way that is only limited by the laser spot size as well as the resolution of the XY-stage. By studying the geometry of the strained regions through AFM imaging we determine the height and width and calculate pseudomagnetic fields of up to hundreds of Tesla using the following formula [133]:

$$\Phi = \frac{\beta h^2}{la}\varphi_0 \qquad (40)$$

Where β is the hopping integral and varies between 2 and 3, *h* and *l* is the height and length of the deformation respectively and *a* is the carbon bond length. Is the flux quantum, i.e. a single flux line of magnitude h/2e. The Raman spectra of such strained regions have demonstrated a definite modulation of the electronic properties that can be related to both doping and straining. We note that a splitting of the G-peak occurs and that the resulting two modes behave quite differently upon additional laser exposure. The higher frequency mode (G+) shows behaviour of a highly doped graphene region and the lower frequency mode (G-) shows an anomalous FWHM behaviour i.e. large increase for unknown reason. We believe that this anomalous behaviour of the FWHM (G-) can be linked to the pseudo-magnetic gauge fields in the deformed regions as such feature in the G-mode have before been reported for Raman spectroscopy studies of graphene with a strong magnetic field applied to the sample [155,156,157].

Chapter 8

Deformation through nanomanipulation in multi-layered graphene

8.1 Nanomanipulation device fabrication technique

Although much research is conducted on the utilization of graphene for novel quantum electronic purposes [119,120], there are however many challenges in creating functional devices with graphene ranging such as the isolation of single or few layered sheets to the transfer, suspension, and manipulation of the material for device fabrication ensuring high quality reproducible conduction channels [158].

One of the most widely studied method for analysing the quality of graphene devices is the magnetic field dependent transport studies. As mentioned before, graphene has exhibited remarkable features and has recently been predicted to be a good platform for studying quantum linear magnetoresistance (QLMR) induced by inhomogenieties or disorder [159,160]. QLMR is one of the historical mysteries of quantum transport, arising from the discovery of the Kapitsa linear law used to explain magnteoresistance features in elemental bismuth originally solved by Abrikosov and later Parish and Littlewood [161]. The quantum LMR phenomenon is elusive in clean defect free homogeneous single, bilayer and trilayer graphene samples due to strong Shubnikov de Haas Oscillations (SdH) which overshadow this effect [162]. However evidence of QLMR in multilayer graphene grown on silicon carbide [159] as well as in mosaic bilayer graphene [160] have recently been reported and have thus renewed research in this illusive quantum phenomena.

The influence of interlayer effects on SdH oscillations and temperature dependent transport parameters in multilayer graphene devices is of great interest as many properties of the charge carriers can be inferred from these features. Temperature damped SdH measurements on single layer, bilayer and trilayer graphene have found suppressed hole and electron effective mass

(*m**) compared to single layer graphene values. This is generally attributed to the renormalization of band structure induced by electron-electron interaction and increase of effective mass with increasing number of layers [163]. One direction of research is to investigate whether or not this trend continues as the number of layers is further increased to few layered samples.

Other studies on multilayered graphene systems established that the electric field effect is prominent and that the frequency of the SdH oscillations could be varied by changing the gate voltage of the devices [164]. Despite the complexity of multilayer graphene systems such a richness in transport physics observed in bilayer and trilayer is a strong motivation to deeper understand few layered graphene samples, hence the study presented in this chapter which looks at the utilization of a novel fabrication process, nanomaniupulation that allows for the creation of suspended multi-layered graphene devices. One of the main advantages of this nanomanipulation technique is that deformations can be easily incorporated into these devices, this has allowed for the tuning of transport properties between the ideal 2DEG to one where QLMR can be observed. Conventional methods used in the fabrication of graphene devices include delicate and complex processes such as electron beam lithography coupled with reactive plasma etching as well as techniques using scanning probe microscopy specifically AFM-lithography and STM imaging and probing [119,120], these processes are however known to produce defects in the graphene layers. Additionally, besides suspended graphene devices, many reported devices have the graphene layer on a silicon oxide substrate which limits electron mobility due to impurities trapped between the SiO_2 and graphene and can lead to substrate doping.

This has motivated us to develop a novel method for the contamination-free fabrication of few layer graphene devices that does not require any lithography or chemical treatments. The process involves mechanically peeling off thin sheets of multilayered graphene from bulk exfoliated graphite stock, placement of the multilayers onto prefabricated electrodes. The process is demonstrated in figure 60. Utilization of this technique also ensures that the graphene layer is suspended and therefore provides transport results without substrate interactions. Since the defect level in nanomanipulated graphene is expected to be different from graphene layers grown by other techniques an investigation of the magnetoresistance of such devices has been conducted. By comparison with results obtained in single layer, bilayer and trilayer graphene devices fabricated by conventional Scotch tape method and e-beam lithography, a strong understanding of the origin of the evolution of transport characteristics in the transition from

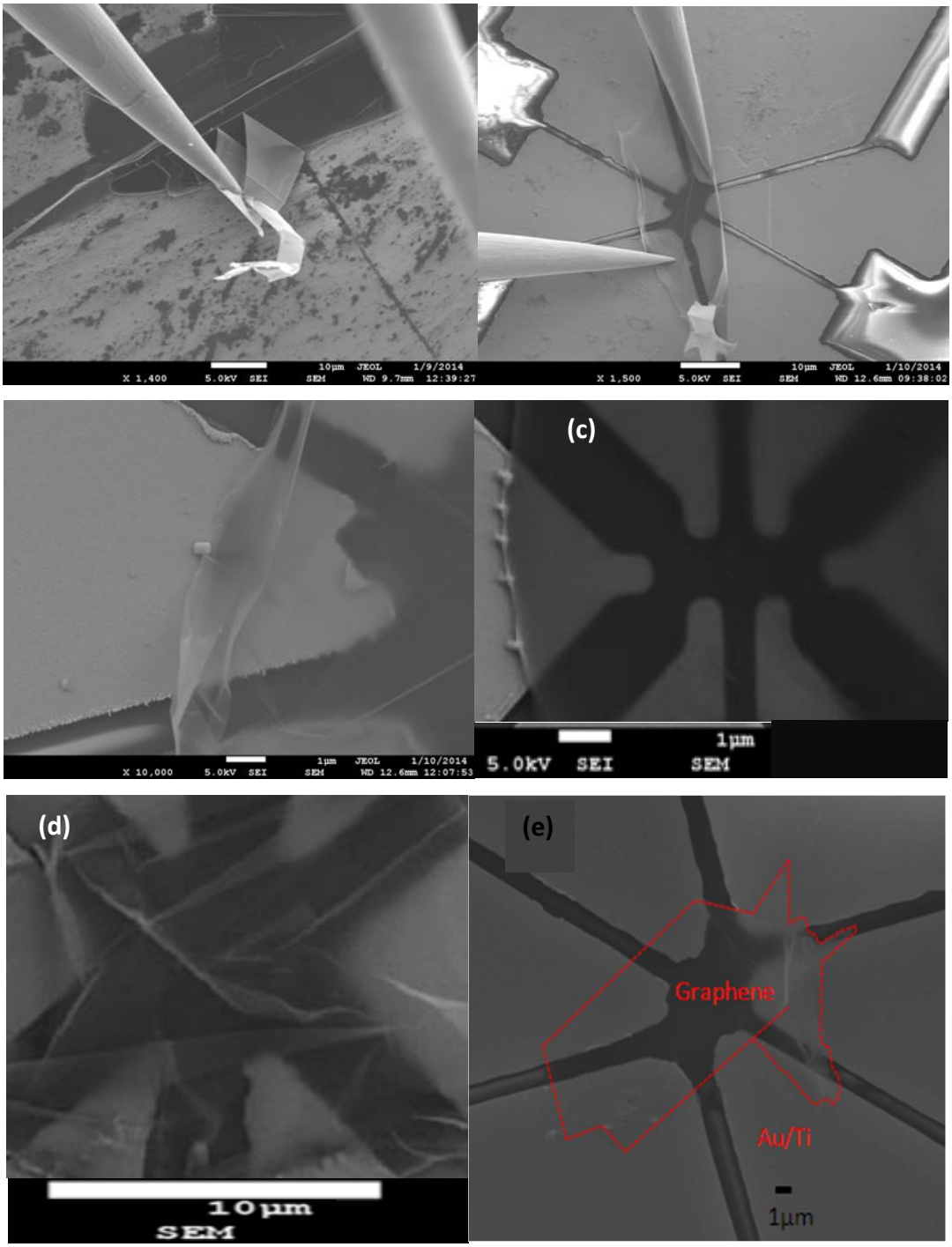

Fig. 46. (Colour on-line) SEM images illustrating the main steps followed in the development of suspended multilayered graphene devices. ***(a)*** *Thin strips of layered graphene are peeled off of larger flakes.* ***(b)*** *The strips are transported to desired location using a nanomanipulator probe tip.* ***(c)*** *Smooth, thick and non-wrinkled multilayer graphene device with Hall bar electrodes. The tungsten tabs keep the suspended graphene in place* ***(d)*** *Wrinkled graphene* ***(e)*** *Smooth, thin and transparent graphene. The dotted red line shows the edge of the graphene layer.*

single layer to graphite can be established [165], thus shedding light on the effect of the number of layers due to interlayer interactions.

The multilayered graphene stock samples were obtained by the conventional Scotch tape method developed by Novoselov and Geim [119] whereby highly ordered pyrolytic graphite is continually mechanically cleaved using an adhesive tape until few layers remain. In our approach, the Scotch tape exfoliated graphite flakes are then deposited onto a SiO_2 substrate. The substrate is then moved to the JEOL J7001F scanning electron microscope (SEM) where the nano-probes are housed. The process involves Kleindek nanomanipulators, with tip radius ~100 nm. Thin strips of layered graphene were peeled off of the larger flakes and transferred by moving the probe to prefabricated electrodes on a different substrate. The multilayered strips where then secured using platinum tabs formed from a combination of SEM beam and gas injection system (OmniGIS). Trimethylmethylcyclopentadienylplatinum (IV) was used as a precursor in the e-beam induced deposition at a chamber pressure of 1.5 $X10^{-5}$ mbar with a gas injection needle line pressure of 2 x 10^{-2} mbar.

This fabrication technique yields both smooth graphene and wrinkled graphene as shown in figures 60 (b) to 1(e). Raman spectroscopy is then used to determine the nature of the multilayer graphene samples. This is shown in figure 61, where a comparison of the Raman spectrum of a multi-layered graphene device is compared to that of single layer sample. The decomposition of the 2D band shows a peak structure different from that of graphite stock but not similar to the unique peak structure observed in bi- or trilayer graphene samples [138,140]. This implies that the sample is composed of more than 4 layers. The small D peak at 1350 cm^{-1} is also observed, indicating some disorder and can be used to track disorder resulting from point defects in the graphene layers as well as folding and rippling. Also noted is the small D peak at 1350 cm^{-1}. This Raman peak is an indication of disorder in the material which may be in form of point defects in the graphene layers as well as folding and rippling.

In wrinkled multilayer graphene (Fig. 60 (d)) the magnetoresistance properties observed are drastically different from smooth layered devices. The magnetoresitance shows quantum linear magnetoresistance (QLMR) at 300 mK in the magnetic field range -12 T to 12 T whereas thin, flat and homogeneous graphene devices showed irregular Shubnikov-de-Haas oscillation which start at intermediate fields of above 4 T and occur only at temperatures below 30 K.

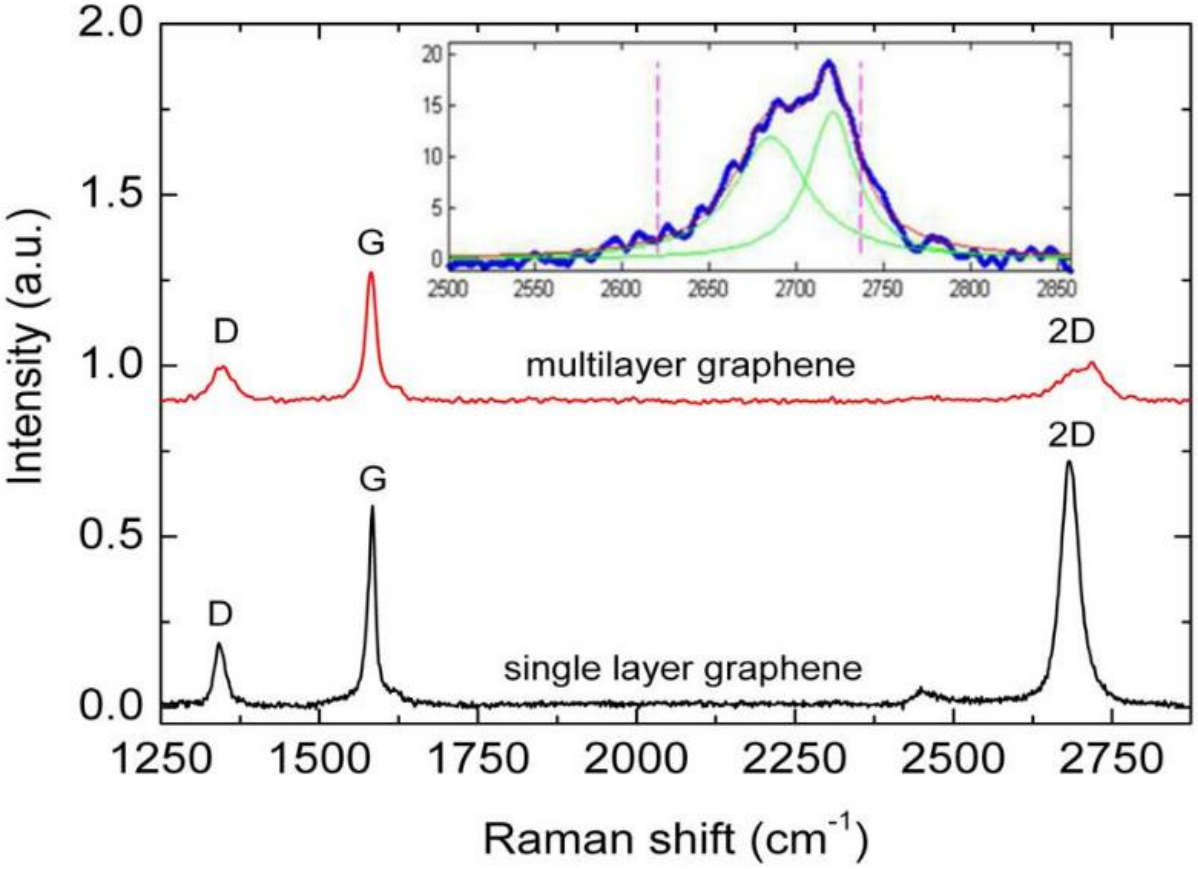

Figure. 47 shows a Raman spectrum for a relatively smooth multilayered graphene device created using Nano-manipulators. The prominent features of the multilayered sample used in this study include the 2D peak at 2700 cm-1 which has a lower intensity than the G peak at 1580 cm-1. This is unlike single layer graphene which has a 2D peak with much greater intensity than that of the G peak. The shape of the 2D band is routinely used to determine the number of layers in few layered samples20. This is possible due to the unique peak shapes which can be fitted with multiple Lorentzian specific to the number of layers up to 4 layers, beyond this number the 2D peak is too similar to that of graphite to determine number of layers. The sample used in this study shows a 2D peak that can be fitted with two Lorentzian curves, the one at higher frequency being more prominent, as is expected for graphite.

8.2 Quantum linear magnetoresistance and Hall Effect

The quantum linear magnetoresistance (Figure 62(a)) and the Hall effect measurements (Figure 62(b)) are useful for determining transport parameters related to the quantum transport physics in this wrinkled graphene system. Using the slope of the QLMR in Figure 62 (a), the carrier density (n_s) as well as the concentration of static scattering centres (N_i) can be determined, here they are found to be in the range 5.2 x 10^9 to 3.5 x10^{13} cm^{-2} and 2.24 x 10^{-2} to 1.02 x 10^{14} respectively. This was determined from data acquired at 300 mK. This is determined from the following description of linear quantum magnetoresistance given by [161,162]:

$$\rho_{xx} = \frac{N_i H}{\pi n_s^2 ec} \propto H \qquad (41)$$

And

$$\rho_{xy} = R_H H = \frac{H}{n_s ec} \qquad (42)$$

Where ρ_{xx} and ρ_{xy} are the longitudinal and transverse components of the magnetoresistance respectively, N_i is the concentration of static scattering centres and n_s is the carrier density [161]. The highest determined electron density in the highly deformed sample is up to 5 times the density (p~7 x$10^{12}$$cm^{-2}$) in polycrystalline mosaic bilayer graphene in which QLMR has previously been reported [159]. However, it is difficult to compare this value to previous reports on QLMR in multi-layered graphene device as in those reports the electron density has not been reported [160]. In fact, to our knowledge, the determination of the concentration of static impurity centres has not been reported before due to the lack of observations of the QLMR effect. The ratio of N_i/n_s in our sample is approximately three at magnetic fields up to 12 T. The exact scattering mechanisms in this material will be addressed in a future paper with temperature dependent MR data. The effective mass of charge carriers in the wrinkled graphene was determined to be 0.0014m_e at zero applied field and 0.121m_e *at 12* T (where m_e is the electron rest mass with a value of 9.109 x10^{-31} kg). This can be interpreted as an indication of a spectrum in wrinkled graphene allowing for both massive and massless fermionic excitations comparable to the reports on the coexistence of massive and massless Dirac Fermions observed in symmetry- broken bilayer graphene samples [166].

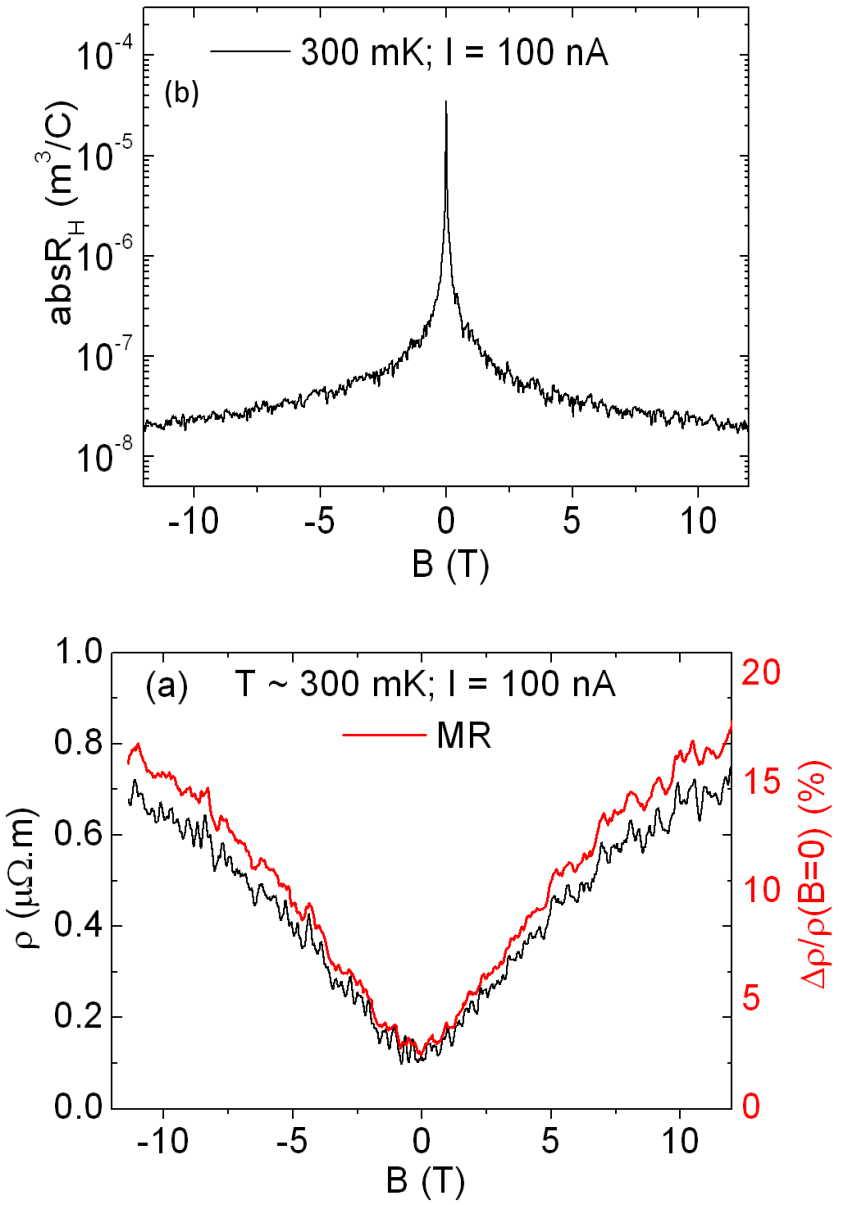

Fig. 48 (a) Quantum linear magnetoresistance for a wrinkled graphene device shown in figure 60(d). (b) Variation of absolute value of Hall coefficient (R_H) with magnetic field for wrinkled graphene device.

Theoretical works on quantum Hall effect of massless Dirac Fermions in a vanishing magnetic field have suggested that the mixing of Landau levels destroys the typical plateaus in Hall conductivity leading to the observed phenomena [167]. In such studies the breaking of the time reversal symmetry was attributed to ripples, folding and corrugations of the graphene samples, again highlighting the role of strain in this Dirac material [168].

Our observations of the QLMR and the modified effective masses of charge carriers are thus in line with literature and strongly suggest that the deformation induced in such devices (i.e. rippling, folding and corrugations) leads to symmetry-breaking. The high magnetic fields will tend to localize the carriers leading to large effective mass, however the localized wavefunctions are not observed to form discrete Landau levels. Under such circumstances the contribution of strong disorder from both interlayer scattering and weak localization from magnetic field will tend to make the Dirac Fermions more massive (in this case $m^* = 0.121 m_e$) which is 2.42 times more massive for ABA stacked trilayer graphene [169] and 3.46 times more massive for AB stacked bilayer graphene [170].

This novel nanomanipulation device fabrication for the production of multi-layered graphene devices thus establishes novel ways of investigating a number of rich and rare physical phenomena, most notably the elusive quantum linear magnetoresistance effect. This is strongly in opposition to conventional graphene devices where the graphene behaves as an ideal 2DEG, as demonstrated in the next section.

8.3 Shubnikov de-Haas Oscillations

The magnetic field dependence of resistance of a smooth multilayer graphene device was characterized over a wide temperature range of 2 - 50 K magnetic fields of up to 12 T applied perpendicular to the devices, this is shown in figure 63 (a and b). It was observed that the device initially exhibits a decrease in resistance as the temperature is raised to approximately 25 K after which further increase in temperature results in an increase in the resistance. The upturn of the temperature dependent resistance is weakly field dependent and occurs at slightly lower temperatures at zero applied field, this can be attributed to electron-electron interactions. Also observed are resistance fluctuations which occur at high magnetic field (8 T) for temperatures below 35 K.

To investigate this oscillatory behaviour in the temperature dependent resistance, magnetoresistance (MR) measurement of the device was undertaken (Figure 63 (b)). It was found that at temperatures below 25 K, the longitudinal magnetoresistance is initially flat then up to fields of 0 T - 4 T, after which oscillations occur with increasing amplitude as the field strength is increased. This is a hall mark of Landau quantization, with the pronounced oscillatory behaviour known as Shubnikov de Haas effect. A negative magnetoresistance

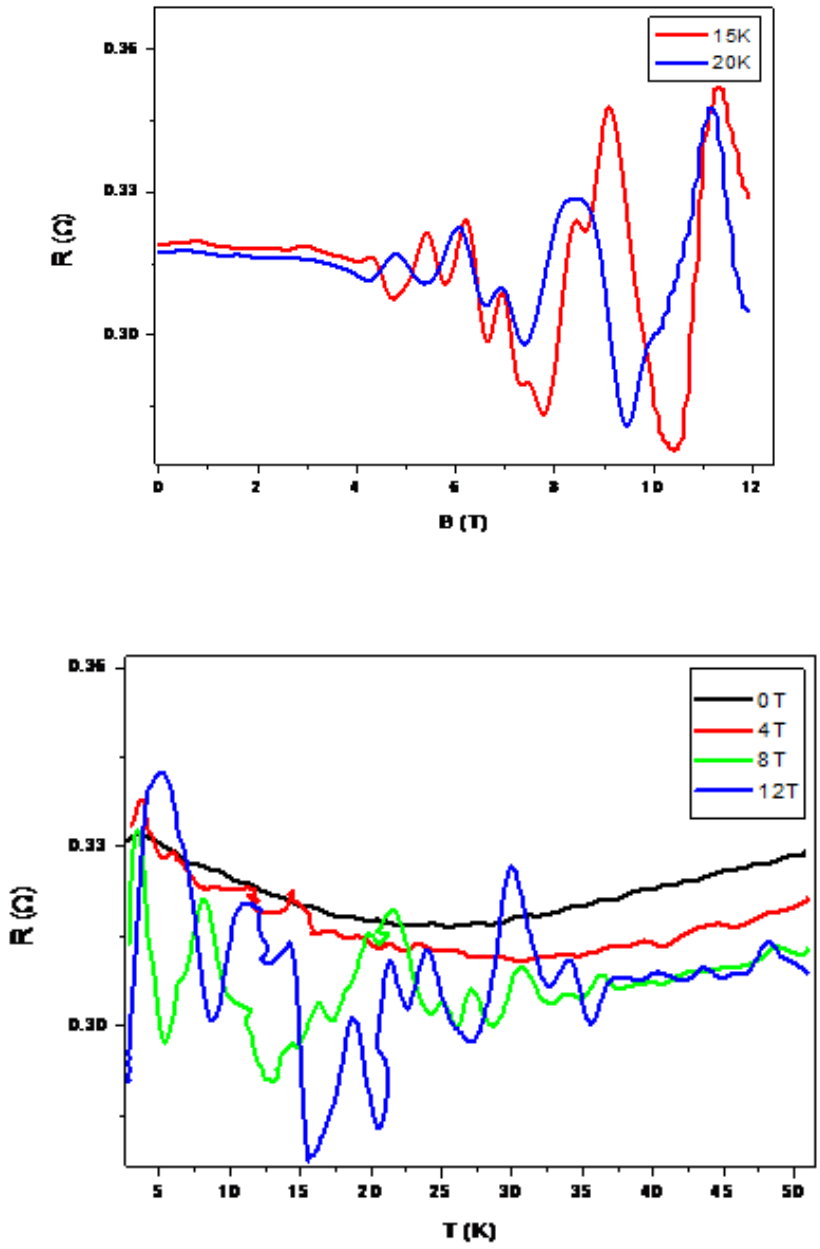

Figure 49 (a) Resistance temperature dependence of four-probe smooth flat, thin and transparent multilayer graphene device at zero magnetic field (black curve) and at a perpendicular applied magnetic field of 8 T. (b) SdH oscillations in the field dependence of the longitudinal resistance of a multilayered graphene device at 15 K.

below 25 K can be attributed to weak localization which has been previously observed in multilayer graphene [170]. These oscillations are observed to be damped as the temperature is increased. By determining the oscillatory frequency through Fourier transformation the Landau level filling index can be determined, $\nu = \frac{n_s h}{2eB}$, where h and e are the Planck's constant and the fundamental charge respectively. The difference between two consecutive Landau levels is thus determined by:

$$\upsilon_1 - \upsilon_2 = \frac{n_s h}{2eB_1} - \frac{n_s h}{2eB_2} = 1 \qquad (43)$$

Thus it is possible to evaluate the carrier density n_s via equation:

$$n_s = \frac{2e}{h}\left(\frac{1}{1/B_1 - 1/B_2}\right) \qquad (44)$$

Through measuring the difference $1/B_1 - 1/B_2$ between two neighbouring peaks in the inverse field plots. As the oscillations are not entirely clear due to multiple frequencies our analysis has only considered the major peaks and neglected the higher harmonics whose origin is expected to arise from interlayer effects.

The carrier density is found to be in the range 1.39×10^{12} - 2.85×10^{12} cm^{-2} and relatively independent of applied magnetic field. The values of carrier concentration are comparable with those reported in single layer (1.47×10^{12} cm^{-2} - 3.43×10^{12} cm^{-2}), bilayer graphene (3.19×10^{12} cm^{-2} - 7.12×10^{12} cm^{-2}) and trilayer graphene samples (4.25×10^{12} - 8.04×10^{12} cm^{-2}) [172,173,174]. From the carrier density the effective mass of the charge carriers can be determined, we find this to in the range $0.022m_e$ to $0.032m_e$. This is comparable with the effective mass measured in single layer ($0.033m_e$), bilayer layer ($0.025m_e$ - $0.055m_e$) and trilayer graphene ($0.035m_e$ - $0.072m_e$) and the ABA-stacked trilayer graphene $m_{ABA} = \sqrt{2m_{AB}} \approx 0.05m_e$ [169,170]. Apart from the carrier density shown in Figure 65 (c), we can extract two extra transport parameters from the SdH oscillations, namely the carrier lifetime or the quantum scattering time and the phase coherence length. The quantum lifetime is determined by following formula for the general form of MR in a two-dimensional electron system (2DES) within the SdH oscillation regime [175]:

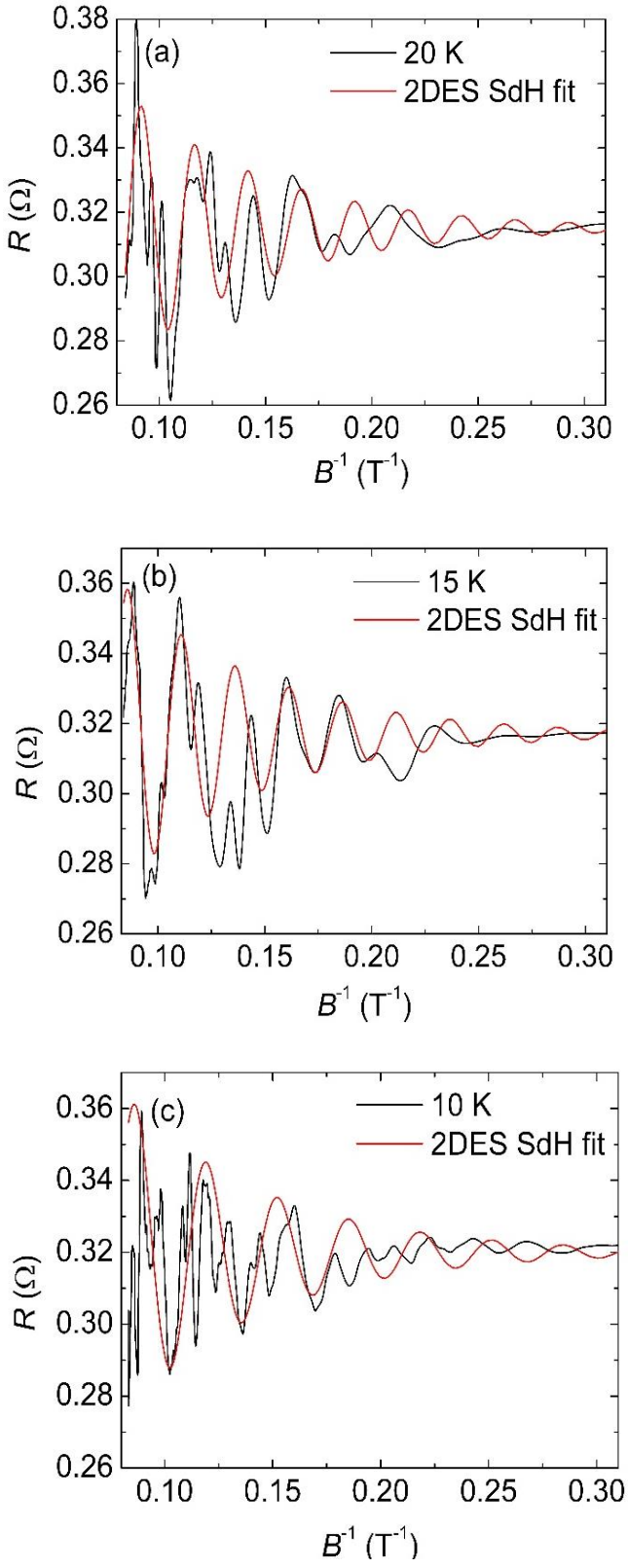

Figure 50. A comparison of the longitudinal resistance as a function of inverse applied magnetic field. Although oscillations do not occur at the same field there is a correspondence in the period at different temperatures (a) 20 K, (b) 15 K, and (c) 10 K.

$$R = R_0[1 + \xi \sum_1^{\infty} D(X)\exp(\frac{s\pi}{w_c\tau})\cos(s\frac{\hbar s_F}{eB} - s\pi + s\varphi_0)] \qquad (45)$$

from which the first order oscillation amplitude be expressed as:

$$A = \xi D(X)\exp(-\frac{\pi}{w_c\tau}) \qquad (46)$$

where $w_c = eB/m^*$ is the cyclotron frequency and $D(X) = \frac{2\pi k_B T/\hbar w_c}{\sinh(2\pi k_B T/\hbar w_c)}$ is the damping factor, k_B is the Boltzmann constant, T is temperature and ξ is a constant [176]. Thus by plotting the extrema amplitudes (A) versus $1/B$ of the oscillation it is possible to determine the carrier lifetime, which is here found to be in the range 11 - 36 fs for mean effective mass $0.026m_e$ (corresponding to a mean carrier density of 1.95×10^{12} cm^{-2}). This value is lower than the lifetime of 54 fs observed in single layer graphene [177]. Figure 65 (b) shows the temperature dependence of the lifetime. The phase coherence length (L_φ) is estimated using formula [178]:

$$\Delta B = \frac{\varphi_0}{L_\varphi^2} \qquad (47)$$

And determined to be 31 nm at 15 K at 10 T. The inverse period of the SdH oscillation can also be used to estimate the cross sectional area (A) of the Fermi surface pocket perpendicular to the magnetic field using the following formula [178]:

$$\Delta(\frac{1}{B}) = \frac{2\pi e}{A\hbar} \qquad (48)$$

For a 10 T field at 15 K we find the Fermi surface area to be ~4.5×10^{17} m^{-2}. It is also observed that as the temperature is increased above 20 K the amplitude of oscillations in the high field regime reduces. The oscillations are also irregular, this can be attributed to interlayer interference effects or the modulation of the SdHO by other kinds of oscillations known as magneto-intersubband oscillations (MISO) and phonon induced resistance oscillations whose origin can be traced to scattering-assisted coupling of carrier states in different Landau levels which can be probed through Raman spectroscopy [155,156,157].

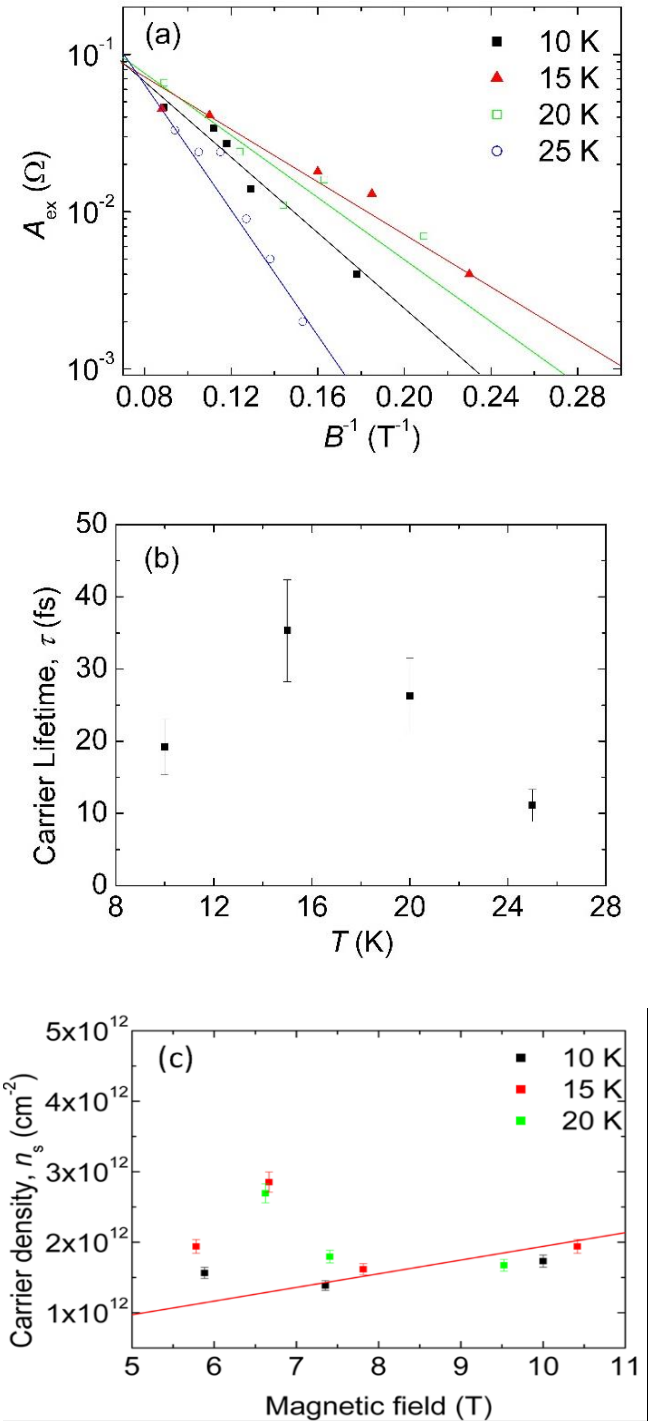

Figure 51 (a) A plot of longitudinal resistance oscillation extrema amplitude (A) versus inverse of perpendicular applied magnetic field. (b) The variation of quantum scattering time with temperature. The scattering time is determined from the slopes of A versus $1/B$ plots in Fig. 6 (a). (c) Calculated carrier density as a function of applied magnetic field at different temperatures. The red bold line is the theoretical Landau level degeneracy $4NeB/h$ where N=2 for single layer graphene.

8.4 High Frequency response of multilayered graphene

Complimentray studies on the High frequency response of multilayered graphene devices fabricated using the method outlined above have been conducted. Manipulation and placement of the exfoliated multilayered graphene onto prefacricaed coplanar waveguides with a channel width of around 0.8 μm was carried out. S-parameter measurements were conducted at room temperature using a custom built (Janis) cryogenic micro-manipulation probe station coupled to an Agilent Precision Network Analyser (PNA). The Low-energy excitations were induced by ensuring that the AC current was kept below saturation. The measurements were conducted over a frequency range and carried out using the short-open-load-through (SOLT) components of the GGB CS-15 calibration kit, here the reference of the signal range was set to 0.01 to 50 GHz and the IF bandwidth was reduced to 500 Hz to enhance the accuracy and reduce noise in the measurement. Following convention the open-short de-embedding equation was utilized in order to extract the measurement parasitices that could influence the results [179]:

$$Y_{DUT} = [(Y_{msd} - Y_{open})^{-1} - (Y_{short} - Y_{open})^{-1}]^{-1} \qquad (49)$$

Where Y_{msd} is the measured admittance of the coplanar waveguide (CPW) plus the attached multilayered graphene flake, Y_{open} and Y_{short} are the admittance of the open and short responses respectivly. The response of the graphene is then obtained by converting the admittance to impedance [180]. As shown in figure 7 the imaginary and real components of the impendence are plotted as a function of frequency, up to 50 GHz. We note a very high conductance in the device associated with the metallic nature of the material. This is probably due to the multilayered nature of the graphene flake, providing multiple conduction channels. Other interesting features of the measurement include a small frequency range of negative reactance i.e. capacitive behaviour which switches back to positive (inductive behaviour) above 15 GHz. The device exhibits an intersection of the real and imaginary parts of the impedence at a frequency of 45 GHz. This corresponds to a cross over from diffusive to ballistic transport with an elastic scattering time of 2.2 ps. This result is consistant with our

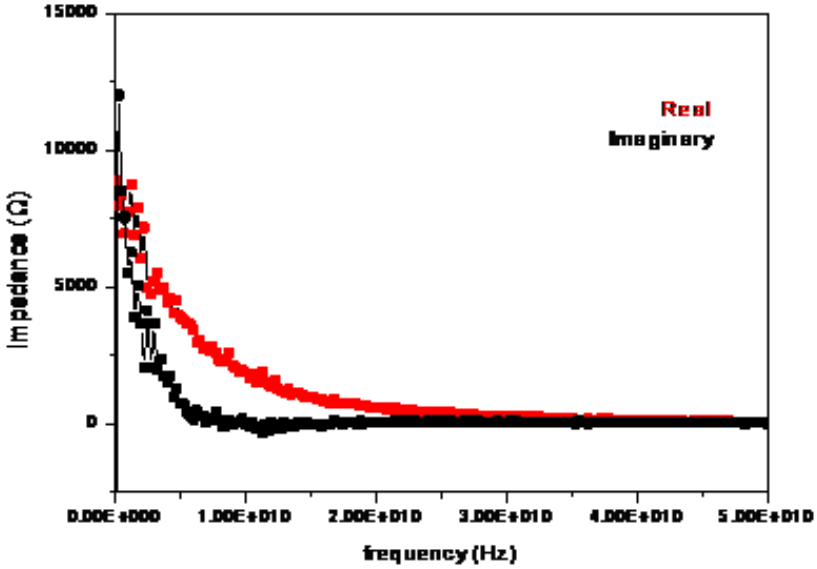

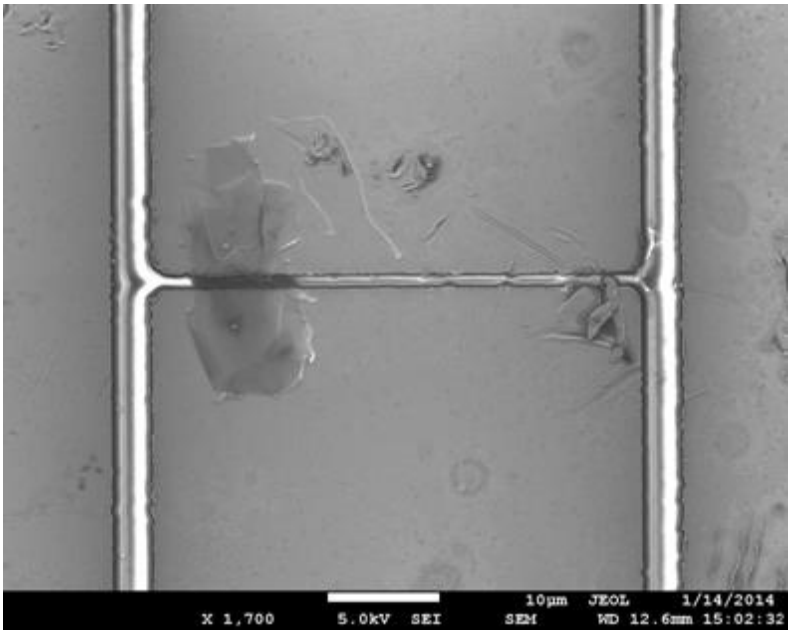

Figure 52. The high frequency response of a multilayered graphene coplanar wave guide device. The real and imaginary components of the impedance are plotted as a function of frequency up to 50 GHz. SEM image of one of the coplanar waveguide devices with multilayer graphene conduction channel.

previous reports on multi-layer carbon superlattice structures which were fabricated from thin graphitic carbon layers [181]. The results shown here are also in line with the high frequency of carbon nanotubes where the charateristic frequency was found to be even smaller than in the present work [182]. It is however, interesting to note that the real and imaginary parts of the impedence remains flat at high frequency regime, idicating that this material has a great potential for high frequency application as exepcted for graphene devices.

In this work we have demonstrated magnetoresistance properties of nano-manipulated suspended multilayer graphene fabricated through a novel nanomanipulation fabrication technique. This fabrication technique allowed for the induction of deformations which were observed to greatly modify the transport properties of the respective devices. In wrinkled graphene we observed a quantum linear magnetoresistance from which we derived carrier densities of up to 5 times that reported for bilayer graphene. The densities were found to scale linearly with applied fields. The smooth multilayer graphene devices on the other hand exhibited SdH oscillations from which we derived carrier density, effective mass, quantum lifetime and phase coherence length which are comparable to those reported for of bilayer and trilayer graphene devices fabricated using conventional techniques. The role of wrinkling is to cause strong disorder that makes the Dirac Fermions in the graphene more massive while at the same time leading to broken-symmetry Dirac points that survive the strong disorder in such a way that massless Dirac Fermions can be sustained. These results of this may be useful in the designing of graphene based devices and establishing of a strong understanding of the transport physics of multilayered carbon based systems. The QLMR results can be useful in the understanding of the role of inhomogeniety in low dimensional systems. In the light of emerging literature on QLMR in mosaic graphene [159,160] we think that our work can add value to this renewed interest in QLMR and its interplay with SdHO in disordered superlattice systems. Fabrication of high frequency coplanar waveguides were also demonstrated using this nanomanipulation technique. The graphene channels of such devices show a high transmission up to 50 GHz.

Concluding remarks on the deformation physics of graphene section

The second half of this thesis is dedicated to the study of deformation physics of graphene. This is an interesting topic as it is one of the more recent directions being followed that allows for the manipulatio0n of transport properties and is able to open a gap in this semi-metal. There are a number of additional interesting features such as the formation of pseudo-magnetic fields that can be of interest in graphene electronics. In particular, I have looked at nanomanipulation as well as a laser assisted annealing method for the deformation of graphene. Both mechanisms have shown to allow for a certain degree of control of the deformation that leads to pronounced changes in the transport as well as phonon modes of the graphene system. Graphene remains one of the most widely studied nano-materials and has a range of interesting properties, these deformation mechanisms studied here will be valuable for the strain engineering direction that is currently being investigated as a serious route for the realization of nano-mechanical and nano-elctrical devices based on this material.

Chapter 9

Conclusion

9.1 Graphene and Superconducting diamond as suitable quantum matter for quantum device applications

This body of work has seen the investigation in the quantum transport of two unique low dimensional carbon systems, namely nanocrystalline boron doped diamond films and graphene. Although ostensibly considered a three dimensional material, here for the first time it has been demonstrated that the system exhibits a pronounced 2D phase. The two dimensionality was established by fitting a combination of the AL and LVV scaling analysis for superconducting (granular) systems. We determine that the 2D phase develops as a result of the Cooper pair coherence length being restricted to the individual grains, most probably due to charging effects between grains. As the system is further cooled the coherence length grows more and eventually the Josephson coupling energy between grains becomes more significant than the charging energy between grains resulting in Josephson tunnelling between grains and hence the global superconducting state. The coupling or tunnelling between grains was also determined by the 3D-AL scaling model and thus our analysis is consistent with granular superconducting films where such dimensionality crossovers have been detected. We have further investigated the two dimensionality of the system by exploring the field induced superconductor to insulator transition. Following the universal scaling scheme established by M. P. Fisher which has successfully been used in a range of 2D superconducting systems. This universal scaling analysis relies on the concept of duality and explains the insulating side of the transition as a bosonic phase comprised of localized Cooper pairs which has been called the Bose or charge-glass phase. We have indeed observed the universal scaling analysis with critical exponents with in the theoretical range for this bosonic system. This is taken as a clear indication that the system does indeed exhibit a 2D phase as established by the AL and LVV scaling. One further manifestation of the two dimensionality of the system is the occurrence of the BKT transition. This transition is related to the formation of vortex states which nucleate

around topological defects and bind to form the long range coherent superconducting state. The BKT transition has been verified through analysis of the power law scaling of the current-voltage characteristics as well as the temperature dependent resistance which is fitted to the HL model. Both methods of analysis give the same BKT temperature to within 40 mK. The BKT temperature was also observed to coincide with the previously reported anomalous bosonic peak, and hence provides supporting evidence that this re-entrant feature is actually a result of the two dimensionality of the system and not necessarily an anomalous feature of three dimensionality as previously claimed. In addition to these features of two dimensionality we have observed novel features not yet reported for the system, this includes zero bias anomaly in the differential resistance. The ZBA are only observed within the fluctuation regime and have a strong temperature and magnetic field dependence. These features are similar to the mid gap states or Andreev bound states observed in the high Tc superconductors and are generally taken as a signature of non s-wave order parameter. The occurrence here as well as the established 2D phase then raises some interesting questions regarding the nature of pairing in the system. At temperatures near and below the re-entrant resistive (BKT) peak we have observed a crossover from negative to positive magnetoresistance in the low field residual resistance. Although not yet conclusively established for this system, these results have been interpreted as a possible topological non-trivial phase comparable to the recently discovered Dirac and Weyl materials. The phase is most likely a result of the intersection of the impurity band with the intrinsic diamond valence band in such a way as to exhibit linear dispersion needed to explain such phenomena. The Magnetoresistance also show pronounced anisotropy similar to Weyl systems which exhibit the Jacky-Adler chiral anomaly. Part one of the work (i.e. related to the boron doped diamond) is concluded with an overview of current diamond based microelectronic and optic device application, this includes some conceptual ideas on junction devices that can be fabricated from superconducting diamond in order to further probe the order parameter of the system. Such studies are still lacking for this material. Device concepts involving resonator devices fabricated using focus ion beam have also been proposed. We also present preliminary proof of concept device elements that we have fabricated using this method, structures include 500 nm nanowire structures as well as SQUID loops. These structures are however yet to be measured.

Part two of the work is focused on strain engineering of both single layer as well as multi layered graphene. As strain engineering has been identified as one of the methods for inducing a gap in the semi-metal, this research direction is currently widely studied. We have thoroughly

investigated the phonon spectrum of graphene using Raman spectroscopy and established a novel method for the formation nanoscaled blisters or bumps in single layered graphene flakes. This method is dubbed Raman or laser annealing as it utilises the Raman spectrometer laser source to locally heat the substrate beneath the graphene. This local heating causes adsorbed gas molecules to be released from the substrate and inflate the local region ofr graphene. The Raman spectrum of the deformations have been mapped using Raman spectroscopy and conformal mapping, the doping effect of the released gas molecules as well as the straining due to deformation are disentangled from the spectra by analysing the splitting and shifting of G-band. The deformation of graphene is expected to result in pseudo magnetic fields of between tens to hundreds of Tesla. This method provides a novel and controllable route for patterning deformations on microscopic graphene flakes, and can easily be applied to actual graphene electronic devices in order to tune its properties. Secondly a novel device fabrication route for the production of multi-layered graphene devices has been investigated. This involves nanomanipulators to peel thin strips of graphene from bulk HOPG stock and gas injection to contact the graphene to pre-fabricated electrodes. This techniques allows for the fabrication of suspended multi-layered devices where the morphology of the surface of the graphene can be controlled. The manipulation process allowed for the deformation of devices and hence a comparative study between smooth and wrinkled devices was conducted. In the case of the smooth graphene conduction channels the expected 2DEG behaviour of the material was clearly observed in the magnetoresistance. We have observed Landau quantization I the form of Shubnikov de Haas oscillations which allowed for extraction of charge carrier properties. We established a slightly larger electron mass due to interlayer coupling. One the other hand the wrinkled device do not exhibit the magnetoresistance oscillations but instead a linear positive magnetoresistance. This deformation thus disrupts the 2D structure of the graphene and hence augments to properties. The nanomanipulation device fabrication process thus allows one to tune the transport properties of multi-layered graphene through deformation routes and may be of use in further device applications.

Although the carbon allotropes such as carbon nanotubes, graphene and fullerenes are some of the most widely studied materials in terms of quantum transport, their integration in quantum technologies (beyond carbon nanotubes) is still a very active area of research. This is partially due to difficulties in handling the various materials as well as utilizing conventional fabrication techniques in producing reliable devices with a standardized functionality. Through the studies presented here, novel transport features as well as device processing techniques have been

explored for the two materials of interest. These studies have highlighted novel and interesting properties for developing novel carbon based devices. Although the two parts can been seen as separate studies there are a range of recent studies that have investigated the physics relating to electronic systems composed of graphene on diamond. Devices consisting of such a hybrid carbon system have already been fabricated and show a largely increased current carrying capacity. To date however the quantum transport of such hybrid systems have not been established and the incorporation of superconducting boron doped diamond with graphene (which can be modified through the various deformation s routes shown here) is expected to result in devices with interesting properties.

This study has highlighted the novel physics and device prospects of two very different low dimensional carbon systems. It is clear that both superconducting diamond and graphene still have many transport features and quantum signatures that have not yet been fully explored. Currently the physics community is experiencing a surge of interest in identifying quantum matter suitable for the incorporation into quantum information technologies. As yet both of these system, (to a larger extent graphene) have been investigated as potential quantum matter for such technologies but no serious application has been found yet. It is thus necessary to further develop and test carbon based devices such as those outlined here in order to help establish carbon based quantum technology.

9.2 Future prospects and potential quantum technologies

9.2.1 Incorporating Raman annealing into conventional graphene device fabrication.

Electron Beam Lithography (EBL) is one of the most prominent techniques utilized in the fabrication of micro- to nanoscale devices. This process allows for the direct patterning of devices down to sub-10nm resolution (depending on resist and maximum resolution of microscope) and can be applied to a wide range of materials. As this fabrication technique is provides a way of high resolution patterning, it is particularly useful for graphene device fabrication. This is because as mentioned before nanoscaled patterning of graphene can greatly enhance the electronic properties. Thus far we have only looked at the fabrication of graphene devices using unconventional techniques such as the nanomanipulation process outlined before. There are however many unique modifications that can be made to the graphene devices using the functionality of electron beam lithography. The electron beam lithography process is briefly outlined now along with possibilities of the incorporation of the Raman annealing procedure with increased control of the deformation potential created.

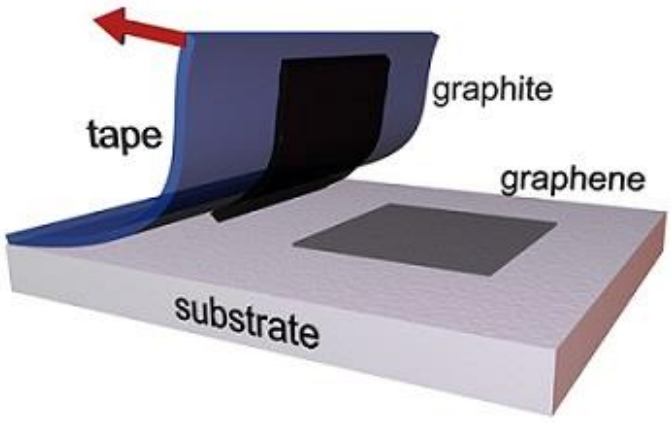

Figure 53 one of the simplest but most widely used method for producing high quality single layer graphene is the scotch tape method developed by the Nobel prize winning physicist Novoselov and Geim [119]. The method involves using an adhesive tape to peel away bulk layers of HOPG until only one layer of graphene remains on the substrate. Figure from reference [182].

The first step in any graphene device fabrication process is securing the graphene. The source of graphene can play a large role in the quality of samples, graphene is usually obtained from three different methods, mechanical exfoliation, CVD synthesis or chemical oxidation of graphitic stock. Shown in figure 67 is the most ubiquitously used method called the scotch tape method which allows for the peeling off of graphene layers from an HOPG stock to give single layer graphene. This route also gives graphene of superior quality compared to graphene obtained through chemical synthesis route. Once graphene flakes of the desired thickness are correctly placed onto the marked SiO2 and characterized with Raman spectroscopy and AFM imaging it was possible to fabricate devices using an electron beam lithography (e-beam) technique. For this process we have utilized a JEOL JSM-700 1F scanning electron microscope driven by Raith pattern generator and EBL controller. The graphene is then coated with a number of thin layers of PMMA polymer which is then baked to harden. This creates a thin film which can be patterned through the lithography to any desired geometries.

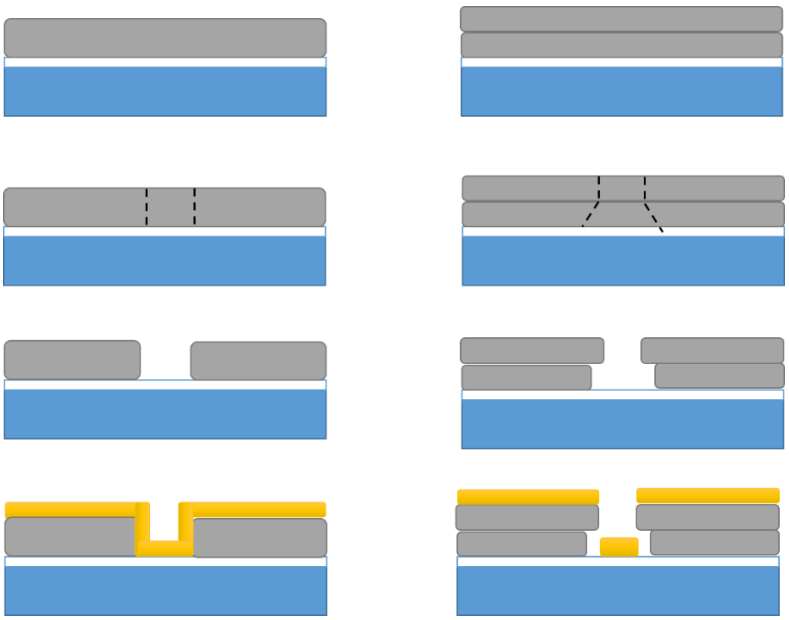

Figure 54 When only one layer of PMMA is used there is a strong possibility of the metallization layer failing to adhere to the substrate due to inner wall coating, as shown in the left column of the above schematic. To overcome this problem an undercut is designed into the layers by spin coating resist layers of different molecular weights and concentrations. The harder (higher molecular weight) or more concentrated the resist solution the more robust the layer is to the electron beam, this translates into different beam degradation rates and allows for an undercut that prevents the inner wall coating and ensures higher device success rates.

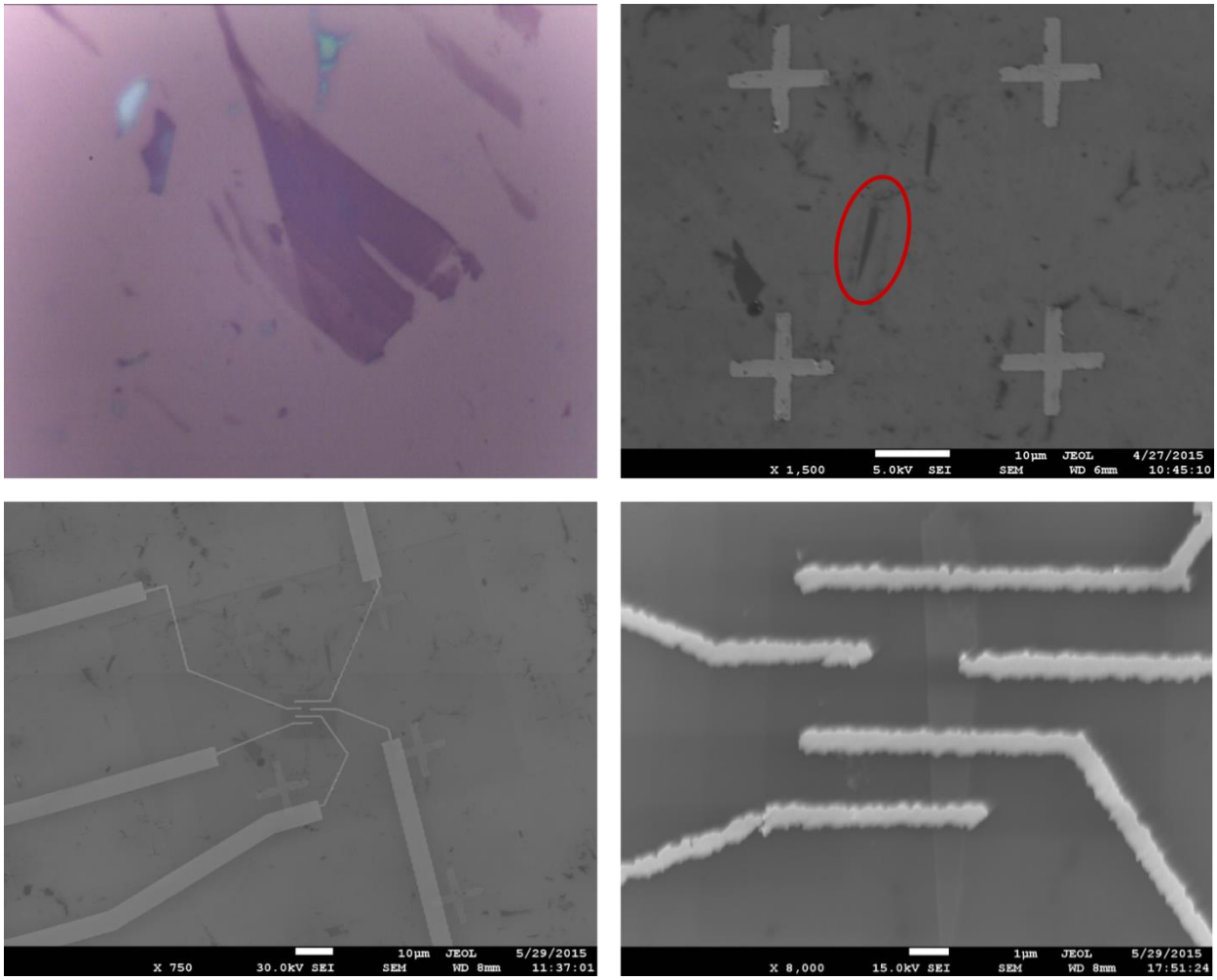

Figure 55. Electron beam lithography is a technical and time intensive process. (a) Single layer graphene flakes are identifiable through optical microscopy due to thin film interference effects, flakes of suitable geometry can thus easily be identified. (b) The graphene flake of interest is indicated by the red ring, its location and orientation on the Si wafer is known thanks to the gold markers which form an array at the centre of the substrate. (c) Multiple exposures and depositions are conducted in order to develop the pattern device. (d) A higher magnification of the device shown in (c) fabricated using the flake shown in (a), the sample was identified as low defect single layer graphene through a combination of Raman spectroscopy and AFM mapping. After the device is complete, wire bonding from the device contact pad onto sample measurement platform is essential for providing good contacts for quantum transport measurement.

The nature of the PMMA used for the mask such as molecular weight, concentration and type of polymer can have serious implications for the resolution of the patterns. Two different PMMA solutions are used because the different molecular weights are broken down at different rates when exposed to the electron beam, this ensures that upon development an undercut is created, the undercut allows for better lift-off especially when creating very ne structures. This is diagrammatically shown in figure 68. The electron beam is then used to pattern the PMMA, exposure of the beam to the PMMA layer degrades the PMMA thus allowing for drawing. After the exposure the degraded polymer regions are washed away using a series of chemicals treatments that only affect the exposed regions (due to the change of their solubility).

After the desired pattern has been created, the mask is ready for deposition. This can be achieved through various evaporative techniques however we have found that electron beam evaporation leads to a high quality circuitry. After the evaporation is completed, the PMMA mask can be washed away using a general solvent such as acetone. This leaves behind only the deposited metal along the patterned area. This process can be applied a number of times to the same device so as to allow for the development of devices with alternating layers. Each layer can lead to additional functionality of the device. An example is demonstrated in figure where micro-scaled array of superconducting metal has been patterned over a functional graphene device. Such structures are particularly interesting for studying superconducting proximity effects in graphene devices [183].

If the array of circular patterns where however utilized not to create an array of metallic islands but rather to form a mask that controls the potion and level of exposure of a laser beam during the Raman annealing process. This would allow for the patterning of deformations on a scale smaller than what is achievable through the unmasked treatment described in a previous chapter. In that case the size of the deformations would be only limited to the resolution of the patterned mask. We have already investigate the patterning of nanoscale arrays that have been implemented in the development of aligned ZnO nanorods structures suitable for photonic device applications. This is shown in figure 70. All that remains is the incorporation of such a technique for the development of nanoscale structures over the fabricated graphene devices such as those shown in figure 69 and 70 (d).

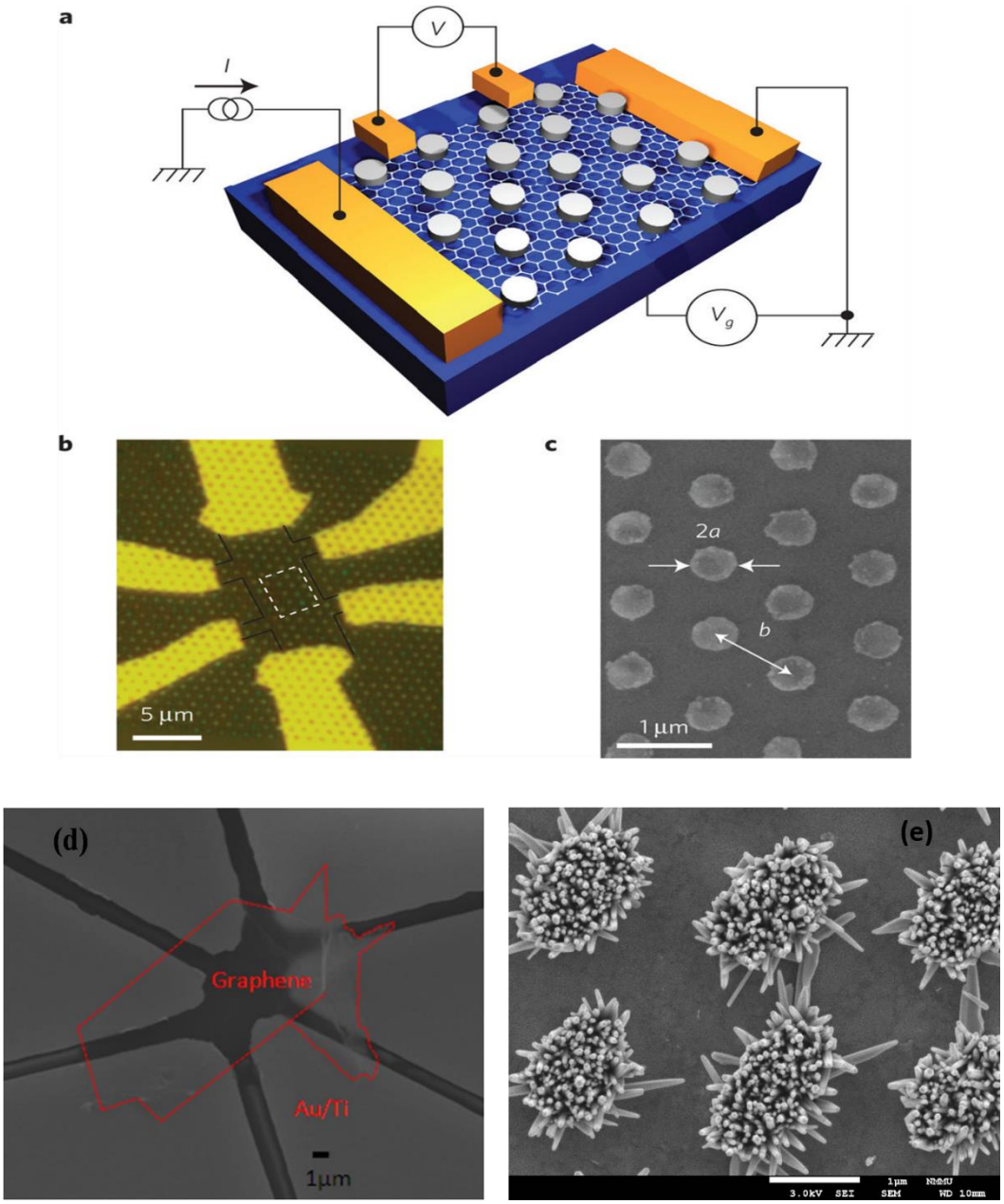

Figure 56. (a-c) Schematic and SEM images of graphene devices with superconducting array patterned over the graphene devices. Images taken from reference [183]. A similar method can be utilized for creating arrays that can be used in patterning the deformed regions using an additional Raman annealing step instead of metallic deposition. This would allow for the fabrication of graphene based device (d) with period deformed regions with modified electronic properties. (e) We have already utilized this EBL patterning to fabricate ZnO nanorod arrays, and have been able to achieve patterns down to 500 nm in diameter.

9.2.2 Contemporary diamond electronics and optic technologies

Although not a conventional material of electronic devices, the use of diamond for niche area application is well documented. Diamond based microelectronics in general make use of the structural hardness of diamond and its durability to ion bombardment, however the negative electron affinity (NEA) of diamond is extremely useful for electrical emitters. Some notable examples of diamond electronics include diamond based vacuum field emission devices [184], specifically nanodiamond lateral field emission vacuum transistors [185]. Such transistors have been experimentally demonstrated with integrated gate and anode electrodes, the devices demonstrated transistor behaviour with gate controlled modulation of the channel current with the expected linear and saturation transport regimes as well as distinct cut-off. Such nanodiamond lateral field emission vacuum transistors exhibited a DC voltage gain of between 200 and 800 and high values of output impedance, reaching up to 10 GΩ.

Diamond has already attached a substantial amount of interest as a potential material for developing quantum technology thanks to its optical properties. The nitrogen vacancy centre (NV-centre) which offers a stable spin state of long coherence is relatively easily probed and manipulated using optical setups. This is particularly interesting for developing quantum memory storage registries. Thanks to various technological and processing developments such NV-centres have also been engineered into single photon emitter arrays [186]. To date, however there is little documented usage of superconducting diamond properties for device application. Only recently [188,189] have reports emerged on the suitability of superconducting diamond for superconducting detectors. Such reports are mainly focused on the slow electron-phonon cooling in this system probed through sub THz radiospectroscopy, this property as well as the relatively high normal state resistance make the system particularly suitable for devices such as hot electron bolometers (HEB) and microwave kinetic inductance detectors (MKID). One of the first demonstrations of microelectronic device elements using boron doped superconducting diamond was the demonstration of a diamond superconducting quantum interference device [190]. In that work the micro-SQUID was fabricated using a combination of electron beam lithography and reactive ion etching. The SQUID demonstrated functionality up to magnetic fields of 4 T with an insensitivity to the direction of the applied

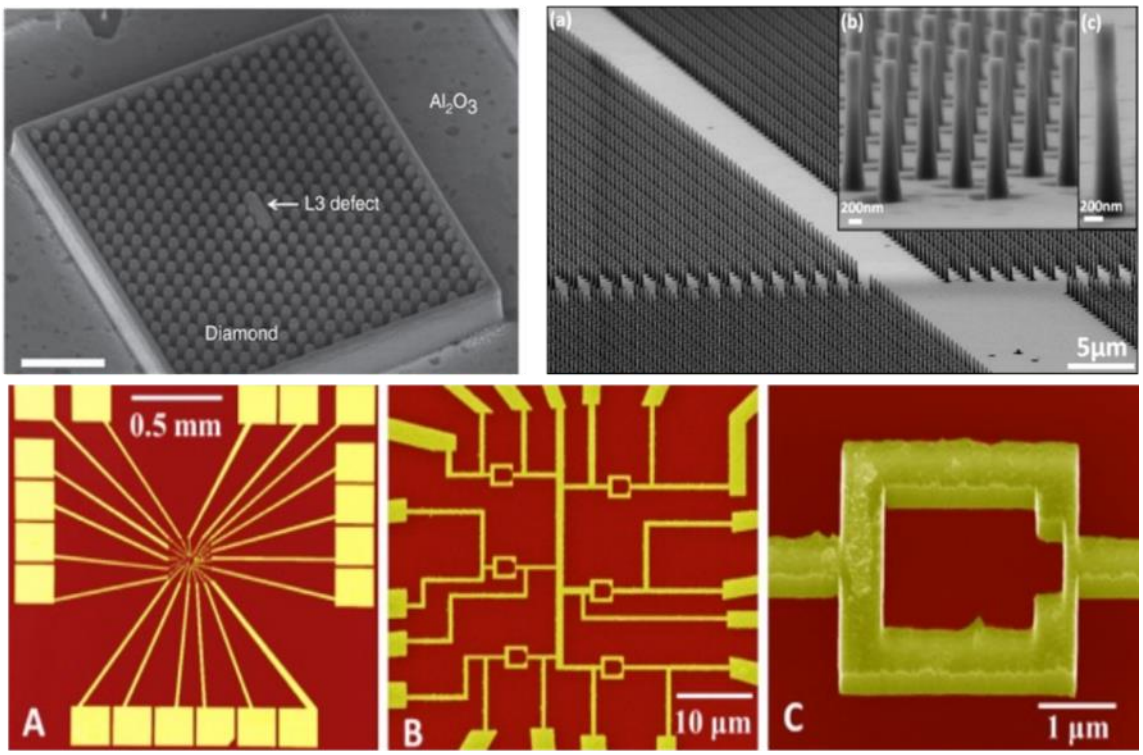

Figure 57 Two examples of single photon emitter arrays fabricated from diamonds with controlled distribution of nitrogen dopants that form the NV-centres. Such devices are interesting due to potential use for quantum memory storage registries, where the readout and probing is done using coherent optical sources. Figures obtained from reference [186, 204]. Monolithic device structures fabricated from boron doped superconducting diamond. (a) Contact pad geometry, (b) array of SQUID devices connected to electrode contacts (c) image of single SQUID structure, the weak links are observed on the right of the image and have a thickness of 500 nm. Picture taken from reference [190]

field and was thus claimed to potentially valuable for detecting quantum motion as a diamond-based nanomechanical oscillator. As diamond is a structurally hard material etching and patterning techniques are usually the most technical challenging aspect of device fabrication, this can however be overcome through either focus Ion Beam (FIB) milling or reactive ion etching, both techniques are generally available in any standard fabrication facility allowing for fabrication to be conducted with relative ease. However as previously stated there are multiple signatures of unconventional superconductivity in this boron-doped diamond system and only once more details on the order parameter and topology of the superconducting diamond is established can work on demonstrating novel diamond based qubit technology begin.

9.2.3 Diamond based superconducting junction devices

At the heart of all superconducting quantum information technology is the Josephson junction (JJ). This tunnel junction relies on the Josephson coupling of superconducting regions separated by a thin non-superconducting interfacial tunnel barrier (or nanoconstriction) and is usually realized using conventional superconducting material interfaced with an insulating or normal metals. All current superconducting qubits are fabricated using single or multiple JJs. It is therefore imperative to not only have a clear understanding of the underlying physics, but also knowledge on how to adjust and manipulate the properties of such a device element. All diamond based JJ have already been fabricated by controlling the amount of boron during synthesis conditions, this allowed for stacked superconducting-normal-superconducting layers that have shown clear Josephson junction properties at cryogenic temperatures [191].

Coupling superconductors to ferromagnets have revealed exotic physical phenomena such as the ability to exhibit a phase shift of π for certain ferromagnetic junction thicknesses [192]. Superconducting spin-valves have also been realized using S/F layered structures, in such devices the Cooper pairing is described as a long ranged triplet state which is robust to magnetic fields. Layered S/F structures have also proven to be useful for the identification of the various pairing symmetries of the order parameter, most notable is the determination of odd frequency pairing which has already been identified in a number of such structures [193].

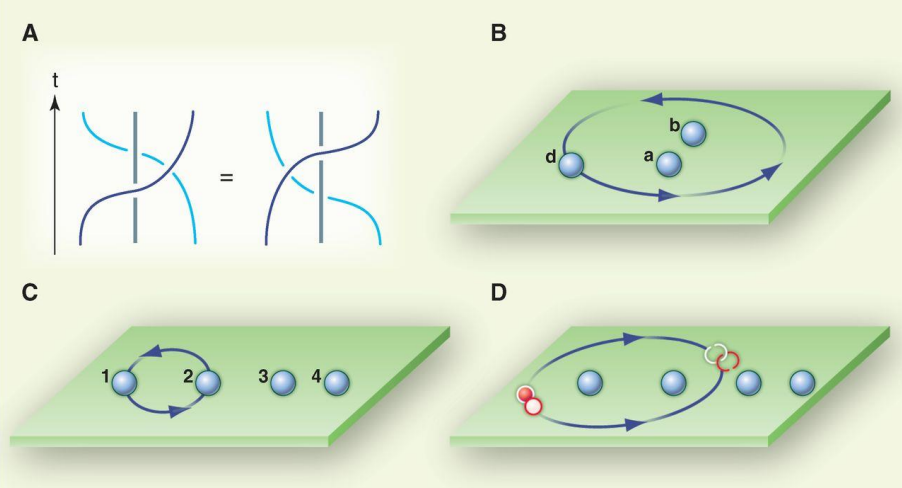

Figure 58 Topological protected quantum states are expected to be robust to environmental noise and dephasing, offering decoherence free logic operations using a procedure called braiding. The braiding is due to the non-abealian statistics that these topological quantum states follow. Figure from reference [194].

More recently there has been a surge in research directed at topologically protected quantum states and their introduction into quantum technologies [194]. This generally involves the coupling of semiconducting nanowires or topological insulators to superconductors in the hopes of exciting exotic quasiparticles, such as the Majorana fermion. Such quasiparticles obey fractional statistics allowing for quantum computational operations known as braiding. Qubits based on this principal are predicted to be robust to decoherence allowing for fault tolerant logic operations. Although there are a number of materials which have been proven to exhibit topological non-trivial phases the utilization of such phenomena in devices is still actively investigated. An interesting avenue of such research is directed towards the realization of topological superconductors. Topological superconductivity is however a rare physical phenomena and has been observed to intrinsically occur in only a hand full of materials. Topological superconductivity can however be induced in junction devices. The topological superconductor is theoretically predicted to host quantum states such as half flux vortices that are expected to be useful for the non-abelian logic operations.

One of the most active areas of research is thus the identification of material which host quantum states useful for quantum logic operations. One material that has already been identified as a potential candidate for quantum technology is diamond. This is because of the various quantum phenomena accessible in diamond, including the well-researched nitrogen vacancy centres (NV-centres) and more recently superconductivity in boron doped diamond films. Although deeper investigations are required, there are already reports on possible topological phase in the nanocrystalline boron doped diamond system. This includes the realization of a two-dimensional phase, the Berezinskii-Kosterlitz-Thouless transition, re-entrant effects and most notably the possibility of spontaneous time reversal symmetry breaking through the observation of crossover of weak to anti-weak localization regimes.

Potential for diamond based quantum technology is generally restricted to investigations of the NV-centres, thus being widely unexplored for superconducting or topological qubit development The work proposed here is twofold: firstly fabricating single junction structures using the superconducting diamond with a range of alternative junction materials such as ferromagnets, conventional s-wave superconductors and insulators (perhaps even vacuum such as in the vacuum transistors recently developed using silicon).

As pointed out, recent investigations into the transport properties of superconducting diamond have indicated the possibility of unconventional superconductivity (specifically two

dimensionality effects), there is therefore a need for a deeper investigation into the nature of the pairing. According to the Pauli exclusion principal, there are three degrees of freedom that need to be taken into account during the formation of Cooper pairs, these are the parity, spin and time dependence of the electron wave functions. In order to evaluate the pairing taking place in superconducting diamond appropriate junction devices based on coupling BDD to s-wave superconductor (Pb or Nb) will need to be investigated. In particular, for the determination of the orbital parity of the order parameter corner-junction devices (see figure 64) have shown to be useful for the identification of both p-wave and d-wave superconductors as such structures are known to present different field dependent transport characteristics due to anisotropic nature of the order parameter.

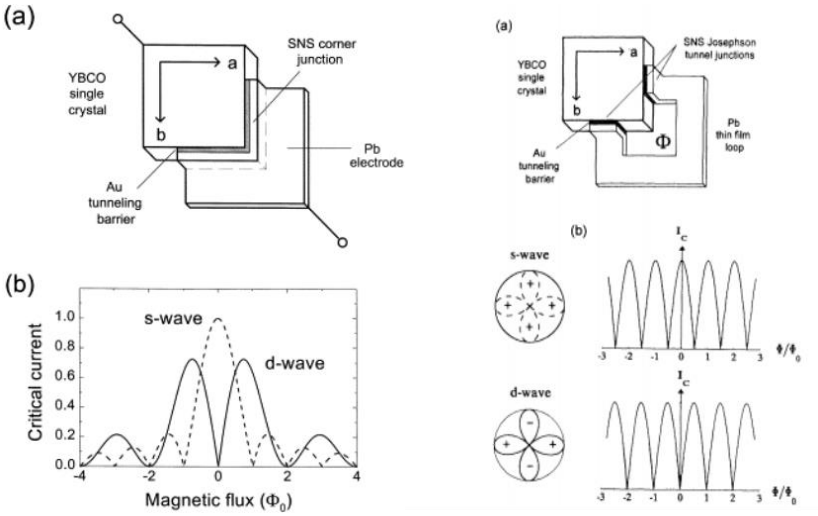

Figure 59. Two examples of device elements that will be useful for the determination of the properties of the Cooper pair wave function pairing. The left structure is the corner JJ which consists of a non-s-wave superconductor contacted through a JJ to a conventional s-wave material. The critical current (bottom left) would show oscillations with magnetic field with period characteristic of the order parameter of the non-s-wave superconductor. Such device elements have not yet been fabricated using superconducting diamond and are expected to lead to deeper insight into this unconventional material. The right diagram shows a SQUID loop fabricated from such a corner junction, again depending on the symmetry of the order parameter characteristic field dependent critical current response can be used to determine the properties of the superconducting diamond. Such device would have additional functionality if using a ferromagnetic material as tunnel barrier, allow for additional symmetry modes such as triplet states or even exotic quasi-particle excitations controllable through the applied flux. Figure from reference [195]

If the superconducting diamond does indeed host a topologically protected phase, when coupled to a ferromagnetic layer, it would allow for the development of odd frequency superconducting systems which are expected to be a signature of Majorana modes. This work is closely related to recent publications on spin-polarized semiconducting nanowires where the existence of such quasiparticles were demonstrated. Coupling the superconducting diamond to ferromagnetic layers or junctions would also allow for control of the spin pairing, potentially forming triplet states such as those reported in superconducting spin valves and hybrid superconducting-magnetic memory devices. The development of S/F junctions may be useful for the realization of controllable 0-π Junctions where the phase of the Josephson current can be controlled by applying a magnetic field, such phase controllable device elements are expected to be useful for the development of field-programmable gate arrays and may be of use for certain operations in flux and phase qubit systems.

9.2.4 Fabrication of superconducting diamond circuit elements using FIB ion milling

As shown previously, diamond has and is currently being investigated for a range of micro and nano-electronic applications. Although it is not a well-known or conventional material for fabricating electronics, there are many conventional fabrication techniques that can successfully applied to diamond films in order to pattern monolithic electronic circuitry. It is thus of utmost importance to ensure that the diamond films are of high quality. Microwave power enhanced CVD is the preferred synthesis route as it is allows for tuning the properties of the diamond film in a controlled way. This is achieved through fine control synthesis parameters such as the microwave power, precursor gas mixture as well as substrate and chamber temperatures. We have recently developed a custom build state of the art multipurpose deposition chamber for dedicated diamond film growth. The system has multiple chambers including electron beam evaporator with a six target crucible holder, RF-plasma chamber for etching capabilities, a thermal evaporator chamber as well as the microwave plasma source deposition chamber. This would allow for not only the synthesis of superconducting boron doped diamond films but also for the various procedures, such as metallic deposition and etching that are useful for fabricating integrated diamond technologies. Figure 76 shows this system with its various chambers. Thus far reactive ion etching (RIE) and electron beam lithography have been the usual go to techniques. The use of focused ion beam (FIB) milling in the fabrication of lamella foils for HR-TEM studies of diamond films is

well documented. Using FIB patterning, a technique become increasing more popular for small scale research grade device fabrication, it should be possible to pattern and develop circuit elements. One of the main disadvantages of FIB milling is contamination from the Ga ions used to mill, there are however a range of newly developed FIB microscopes that utilize inert or noble gas molecules for the ion source. Notable examples are the He produced by Carl Zeiss. Thus avoiding the contamination or doping of Ga ions and offering vastly reduced patterning times. We have already investigated FIB patterning as a method of diamond device fabrication. As shown in figure 77, nanowires with a thickness of 500 nm and a length of 100 µm have been fabricated from 500 nm thick diamond films. The ends of the nanowires are contact pads 300 um in width and length. An additional step in depositing metal contact, comprised of thin seeding layer of titanium and a Gold surface, would be essential for measuring the conduction channel. Alternatively, gas injection contacting of

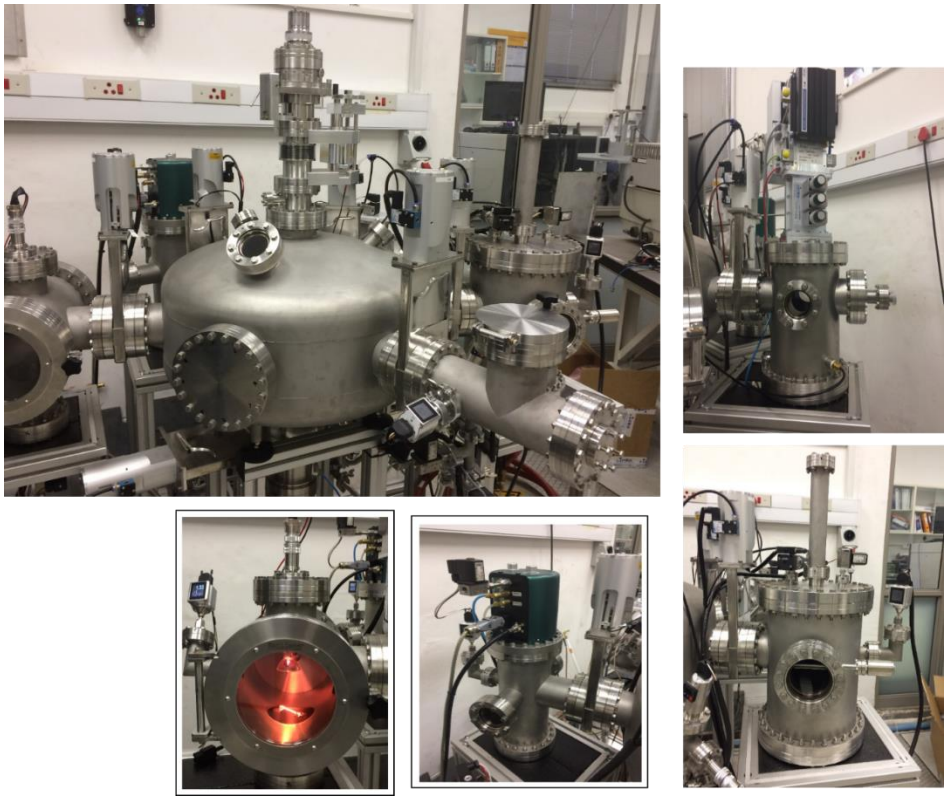

Figure 60 Multi-purpose rotating sample deposition chamber. (a) Thermal evaporation and CVD chamber. (b) RF-plasma chamber for substrate cleaning or etching. (c) Electron beam evaporating chamber with six crucible target allowing for multiple layer evaporations without breaking chamber vacuum. (d) Microwave powered CVD diamond chamber with trimethylborane gas source for the synthesis of superconducting boron doped diamond films.

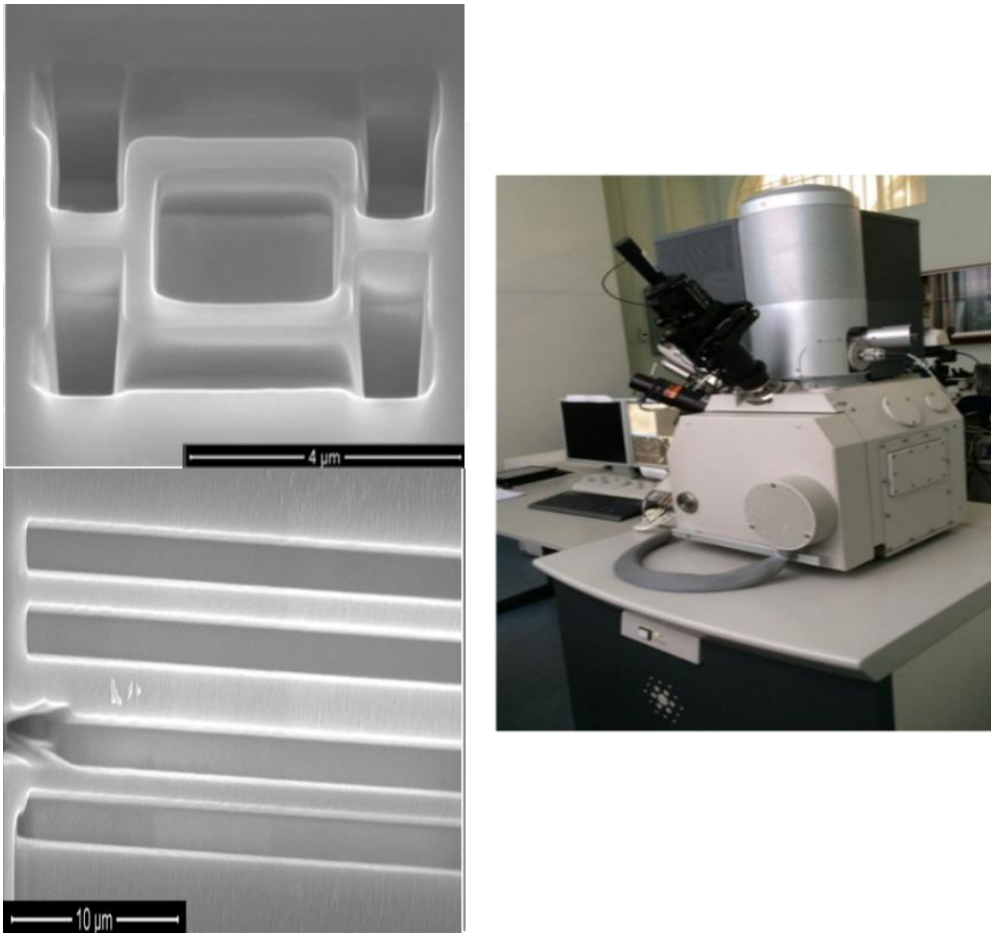

Figure 61. Using FIB-SEM ion milling allows for high precision monolithic patterning of boron doped nanocrystalline diamond films. (a) Nanowires of 500 nm in thickness have been fabricated as well as (b) SQUID structures. The ease of this patterning techniques allows for circuit elements with tailored geometries to be fabricated without any chemical processing typically used in lithography.

measurement wires to the contact pads can also be done, usually in the same FIB-SEM chamber. The image on the right is a potential SQUID loop also patterned from the boron-doped diamond using FIB milling. As there is currently not much literature on such diamond based electronic structures, they will require rigorous testing in order to determine the properties, particularly the quantum transport features. It is well documented that superconducting nanowire can allow for the observation of a range of interesting and novel properties. One are in particular is that of quantum phase slip whereby the order parameter of the superconducting material tunnels through narrow constrictions. This type of device is currently being heavily investigated for application such as quantum computing to quantum metrology.

Quantum information technology is being seriously pursued by a range of large corporations including IBM, Google, Microsoft and Intel. The most ubiquitous forms of quantum computers are based on superconducting qubits. Superconducting qubits can in general be classified into three categories based on the quantum degree of freedom exploited during the logic operations. These are the Charge, Flux and Phase qubits. Charge qubits, or Cooper pair boxes are superconducting islands that are controlled by an electric gate, the gate controls the tunnelling of electrons through a Josephson Junction separating the superconducting islands and measurement channel. Flux qubits are created from SQUID loops with weak links, either one, two or three, where the tunnelling between the weak links (JJ) is controlled by manipulating the flux that penetrates the effective area of the SQUID. The Phase qubit utilizes a combination of flux and charge in order to manipulate and measure the qubits. More recently coupling qubits to coplanar waveguides as well as 3D resonant cavities has been achieved. Such devices are generally referred to as Transmons.

References:

1. E. A. Ekimov, V. A. Sidorov, E. D. Bauer, N. N. Mel'Nik, N. J. Curro, J. D. Thompson, and S. M. Stishov, Superconductivity in diamond. Nature, **428**, 542 (2004).
2. E. Bustarret, C. Marcenat, P. Achatz, J. Kačmarčik, F. Lévy, A. Huxley, L. Ortéga, E. Bourgeois, X. Blase, D. Débarre, and J. Boulmer, Nature, **444**, 465 (2006).
3. T. Herrmannsdörfer, V. Heera, O. Ignatchik, M. Uhlarz, A. Mücklich, M. Posselt, H. Reuther, B. Schmidt, K.-H. Heinig, W. Skorupa, M. Voelskow, C. Wündisch, R. Skrotzki, M. Helm, and J. Wosnitza, Phys. Rev. Lett., **102**, 217003 (2009).
4. N. Dubrovinskaia, A. Eska, G. A. Sheshin, and H. Braun, Superconductivity in polycrystalline boron-doped diamond synthesized at 20 GPa and 2700 K. Journal of applied physics, **99**, 033903 (2006).
5. M. Nesládek, D. Tromson, C. Mer, P. Bergonzo, P. Hubik, P. and J. J. Mares, Superconductive B-doped nanocrystalline diamond thin films: Electrical transport and Raman spectra. Applied Physics Letters, **88**, 232111 (2006).
6. Y. Tzeng, S. Yeh, W. C. Fang, and Y. Chu, Nitrogen-incorporated ultrananocrystalline diamond and multi-layer-graphene-like hybrid carbon films. Scientific reports, **4**, 4531 (2014).
7. Bhattacharyya, S., Mechanism of high n-type conduction in nitrogen-doped nanocrystalline diamond. Physical Review B, **70** (12), p.125412 (2004).
8. Ramdas, A.K. and Rodriguez, S., Spin–orbit coupling, mass anisotropy, time-reversal symmetry, and spontaneous symmetry breaking in the spectroscopy of shallow centers in elemental semiconductors. Solid state communications, **117** (3), pp.213-222 (2001).
9. Dubrovinskaia, N., Wirth, R., Wosnitza, J., Papageorgiou, T., Braun, H.F., Miyajima, N. and Dubrovinsky, L., An insight into what superconducts in polycrystalline boron-doped diamonds based on investigations of microstructure. Proceedings of the National Academy of Sciences, **105** (33), pp.11619-11622 (2008).
10. Lu, Y.G., Turner, S., Ekimov, E.A., Verbeeck, J. and Van Tendeloo, G., Boron-rich inclusions and boron distribution in HPHT polycrystalline superconducting diamond. Carbon, **86**, pp.156-162 (2015).
11. Polyakov, S.N., Denisov, V.N., Mavrin, B.N., Kirichenko, A.N., Kuznetsov, M.S., Martyushov, S.Y., Terentiev, S.A. and Blank, V.D., Formation of boron-carbon nanosheets and bilayers in boron-doped diamond: origin of metallicity and superconductivity. Nanoscale research letters, **11** (1), p.11 (2016).

12. Polyakov, S.N., Denisov, V.N., Mavrin, B.N., Kirichenko, A.N., Kuznetsov, M.S., Martyushov, S.Y., Terentiev, S.A. and Blank, V.D., Formation of boron-carbon nanosheets and bilayers in boron-doped diamond: origin of metallicity and superconductivity. Nanoscale research letters, **11** (1), p.11 (2016).
13. Zhang, G., Janssens, S.D., Vanacken, J., Timmermans, M., Vacík, J., Ataklti, G.W., Decelle, W., Gillijns, W., Goderis, B., Haenen, K. and Wagner, P., Role of grain size in superconducting boron-doped nanocrystalline diamond thin films grown by CVD. Physical Review B, **84** (21), p.214517 (2011).
14. Wang, Y.G., Lau, S.P., Tay, B.K. and Zhang, X.H., Resonant Raman scattering studies of Fano-type interference in boron doped diamond. Journal of applied physics, **92** (12), pp.7253-7256 (2002).
15. Gajewski, W., Achatz, P., Williams, O.A., Haenen, K., Bustarret, E., Stutzmann, M. and Garrido, J.A., Electronic and optical properties of boron-doped nanocrystalline diamond films. Physical Review B, **79** (4), p.045206 (2009).
16. Yokoya, T., Nakamura, T., Matsushita, T., Muro, T., Takano, Y., Nagao, M., Takenouchi, T., Kawarada, H. and Oguchi, T., Origin of the metallic properties of heavily boron-doped superconducting diamond. Nature, **438** (7068), p.647 (2005).
17. Guyot, H., Achatz, P., Nicolaou, A., Le Fèvre, P., Bertran, F., Taleb-Ibrahimi, A. and Bustarret, E., Band structure parameters of metallic diamond from angle-resolved photoemission spectroscopy. Physical Review B, **92** (4), p.045135 (2015).
18. Guyot, H., Achatz, P., Nicolaou, A., Le Fèvre, P., Bertran, F., Taleb-Ibrahimi, A. and Bustarret, E., Band structure parameters of metallic diamond from angle-resolved photoemission spectroscopy. Physical Review B, **92** (4), p.045135 (2015).
19. Maier, F., Graupner, R., Hollering, M., Hammer, L., Ristein, J. and Ley, L., The hydrogenated and bare diamond (110) surface: a combined LEED-, XPS-, and ARPES study. Surface science, **443** (3), pp.177-185 (1999).
20. Bustarret, E., Achatz, P., Sacépé, B., Chapelier, C., Marcenat, C., Ortega, L. and Klein, T., Metal-to-insulator transition and superconductivity in boron-doped diamond. Philosophical Transactions of the Royal Society of London A: Mathematical, Physical and Engineering Sciences, **366** (1863), pp.267-279 (2008).
21. Klein, T., Achatz, P., Kacmarcik, J., Marcenat, C., Gustafsson, F., Marcus, J., Bustarret, E., Pernot, J., Omnès, F., Sernelius, B.E. and Persson, C., Metal-insulator transition and superconductivity in boron-doped diamond. Physical Review B, **75** (16), p.165313 (2007).

22. Kawano, A., Ishiwata, H., Iriyama, S., Okada, R., Yamaguchi, T., Takano, Y. and Kawarada, H., Superconductor-to-insulator transition in boron-doped diamond films grown using chemical vapor deposition. Physical Review B, **82** (8), p.085318 (2010).
23. Lee, K.W. and Pickett, W.E., Superconductivity in boron-doped diamond. Physical review letters, **93** (23), p.237003 (2004).
24. Xiang, H.J., Li, Z., Yang, J., Hou, J.G. and Zhu, Q., Electron-phonon coupling in a boron-doped diamond superconductor. Physical Review B, **70** (21), p.212504 (2004).
25. Boeri L., Kortus J. and Andersen O.K., Three-Dimensional MgB 2-Type Superconductivity in Hole-Doped Diamond. *Physical review letters*, **93** (23), p.237002 (2004).
26. Fukuyama, H., Ohta, Y., Shirakawa, T. and Horiuchi, S., Superconductivity in B-doped diamonds, *Journal of Physics and Chemistry of Solids*, **69** (12), pp.3265-3268 (2008).
27. Shirakawa, T., Horiuchi, S., Ohta, Y. and Fukuyama, H., Theoretical study on superconductivity in boron-doped diamond. Journal of the Physical society of Japan, **76** (1), p.014711 (2007).
28. Okazaki, H., Wakita, T., Muro, T., Nakamura, T., Muraoka, Y., Yokoya, T., Kurihara, S.I., Kawarada, H., Oguchi, T. and Takano, Y., Signature of high T c above 25 K in high quality superconducting diamond. Applied physics letters, **106** (5), p.052601 (2015).
29. Blase, X., Adessi, C. and Connetable, D., Role of the dopant in the superconductivity of diamond. Physical review letters, **93** (23), p.237004 (2004).
30. Mareš, J.J., Nesladek, M., Hubík, P., Kindl, D. and Krištofik, J., On unconventional superconductivity in boron-doped diamond. Diamond and related materials, **16** (1), pp.1-5 (2007).
31. Mareš, J.J., Hubík, P., Nesládek, M., Kindl, D. and Krištofik, J., Weak localization—precursor of unconventional superconductivity in nanocrystalline boron-doped diamond. Diamond and related materials, **15** (11-12), pp.1863-1867 (2006).
32. Hekking, F.W.J. and Nazarov, Y.V., Interference of two electrons entering a superconductor. Physical review letters, **71** (10), p.1625 (1993).
33. Sachdev, S., The quantum phases of matter. arXiv preprint arXiv:1203.4565 (2012).
34. Kivelson, S.A., Bindloss, I.P., Fradkin, E., Oganesyan, V., Tranquada, J.M., Kapitulnik, A. and Howald, C., How to detect fluctuating stripes in the high-temperature superconductors. Reviews of Modern Physics, **75** (4), p.1201 (2003).
35. Sachdev, S., The quantum phases of matter. arXiv preprint arXiv:1203.4565 (2012).

36. Baskaran, G., Resonating valence bond mechanism of impurity band superconductivity in diamond. Journal of Superconductivity and Novel Magnetism, **21** (1), pp.45-49 (2008).
37. Spatially correlated microstructure and superconductivity in polycrystalline boron-doped diamond. Physical Review B, **82** (3), p.033306 (2010).
38. Takano, Y., Superconductivity in CVD diamond films. Journal of Physics: Condensed Matter, **21** (25), p.253201 (2009).
39. Sacépé, B., Chapelier, C., Marcenat, C., Kačmarčik, J., Klein, T., Bernard, M. and Bustarret, E., Tunneling spectroscopy and vortex imaging in boron-doped diamond. Physical review letters, **96** (9), p.097006 (2006).
40. Yokoyama, T., Ichioka, M. and Tanaka, Y., Theory of pairing symmetry in Fulde–Ferrell–Larkin–Ovchinnikov vortex state and vortex lattice. Journal of the Physical Society of Japan, **79** (3), p.034702 (2010).
41. Zhang, G., Samuely, T., Kačmarčík, J., Ekimov, E.A., Li, J., Vanacken, J., Szabó, P., Huang, J., Pereira, P.J., Cerbu, D. and Moshchalkov, V.V., Bosonic Anomalies in Boron-Doped Polycrystalline Diamond. Physical Review Applied, **6** (6), p.064011 (2016).
42. Mtsuko, D., Nesladek, M. and Bhattacharyya, S., Finite bias dependent evolution of superconductor-insulator transition in nanodiamond films. arXiv preprint arXiv:1606.06672 (2016).
43. Zhang, G., Zeleznik, M., Vanacken, J., May, P.W. and Moshchalkov, V.V., Metal–bosonic insulator–superconductor transition in boron-doped granular diamond. Physical review letters, **110** (7), p.077001 (2013).
44. Sachdev, S., Quantum criticality: competing ground states in low dimensions. Science, **288** (5465), pp.475-480 (2000).
45. Sato, M. and Ando, Y., Topological superconductors: a review. Reports on Progress in Physics, **80** (7), p.076501 (2017).
46. Hasan, M.Z. and Kane, C.L., Colloquium: topological insulators. Reviews of Modern Physics, **82** (4), p.3045 (2010).
47. Gladchenko, S., Olaya, D., Dupont-Ferrier, E., Douçot, B., Ioffe, L.B. and Gershenson, M.E., Superconducting nanocircuits for topologically protected qubits. Nature Physics, **5** (1), p.48 (2009).

48. Shi, W., Sun, J., Yao, W., Jiang, J., Liu, L., Yin, H. and Qi, Z., A study of deposited YBaCuO thin films by DC magnetron sputtering. Modern Physics Letters B, **1** (09n10), pp.369-374 (1988).
49. Galitski, V.M. and Larkin, A.I., Superconducting fluctuations at low temperature. Physical Review B, **63** (17), p.174506 (2001).
50. Beloborodov, I.S., Lopatin, A.V., Vinokur, V.M. and Efetov, K.B., Granular electronic systems. Reviews of Modern Physics, **79** (2), p.469 (2007).
51. Pradhan, A.K., Roy, S.B., Chaddah, P., Chen, C. and Wanklyn, B.M., Fluctuation phenomena in excess conductivity and magnetization of single-crystal $Bi_2Sr_2CaCu_2O_{8+y}$. Physical Review B, **50** (10), p.7180 (1994).
52. Ghosh, A.K., Bandyopadhyay, S.K. and Basu, A.N., Generalization of fluctuation induced conductivity in polycrystalline $Y_{1-x}Ca_xBa_2Cu_3O_y$ and $Bi_2Sr_2Ca_1Cu_2O_{8+\delta}$ superconductors. Journal of applied physics, **86** (6), pp.3247-3252 (1999).
53. Varlamov, A.A., "Fluctuoscopy" of Superconductors. In Fundamentals of Superconducting Nanoelectronics, (pp. 1-43). Springer, Berlin, Heidelberg. (2011)
54. Jurelo, A.R., Castillo, I.A., Roa-Rojas, J., Ferreira, L.M., Ghivelder, L., Pureur, P. and Rodrigues Jr, P., Coherence transition in granular high temperature superconductors. Physica C: Superconductivity, **311** (1-2), pp.133-139 (1999).
55. Aslamasov, L.G. and Larkin, A.I., The influence of fluctuation pairing of electrons on the conductivity of normal metal. Physics Letters A, **26** (6), pp.238-239 (1968).
56. Deutscher, G., Goldman, A.M. and Micklitz, H., Percolation-localization crossover and depression of the superconducting transition temperature in films of metal-insulator mixtures. Physical Review B, **31** (3), p.1679 (1985).
57. Shi, Y.H., Wang, H.S., Wang, Y.G., Lu, Y., Zhao, B.R., Zhao, Y.Y. and Li, L., The superconductivity, structure and microstructure of Ba□ Y□ Sc□ Cu oxides. Solid state communications, **63** (7), pp.641-643 (1987).
58. Maki, K., Critical fluctuation of the order parameter in a superconductor. I. Progress of Theoretical Physics, **40** (2), pp.193-200 (1968); Thompson, R.S., Microwave, flux flow, and fluctuation resistance of dirty type-II superconductors. Physical Review B, **1** (1), p.327 (1970).
59. Livanov, D.V., Savona, G. and Varlamov, A.A., Strong compensation of the quantum fluctuation corrections in a clean superconductor. Physical Review B, **62** (13), p.8675 (2000).

60. Lerner, I.V., Varlamov, A.A. and Vinokur, V.M., Fluctuation spectroscopy of granularity in superconducting structures. Physical review letters, **100** (11), p.117003 (2008).
61. Blanter, Y.M., Vinokur, V.M. and Glazman, L.I., Weak localization in metallic granular media. Physical Review B, **73** (16), p.165322 (2006).
62. Jaeger, H.M., Haviland, D.B., Orr, B.G. and Goldman, A.M., Onset of superconductivity in ultrathin granular metal films. Physical Review B, **40** (1), p.182 (1989).
63. Klemencic, G.M., Fellows, J.M., Werrell, J.M., Mandal, S., Giblin, S.R., Smith, R.A. and Williams, O.A., Fluctuation spectroscopy as a probe of granular superconducting diamond films. Physical Review Materials, **1** (4), p.044801 (2017).
64. Skocpol, W.J. and Tinkham, M., Fluctuations near superconducting phase transitions. Reports on Progress in Physics, **38** (9), p.1049 (1975).
65. Schneider, R., Zaitsev, A.G., Fuchs, D. and von Löhneysen, H., Excess conductivity and Berezinskii–Kosterlitz–Thouless transition in superconducting FeSe thin films. Journal of Physics: Condensed Matter, **26** (45), p.455701 (2014).
66. W. E. Lawrence and S. Doniach, in Proceedings of the Twelfth International Conference on Low Temperature Physics, edited by E. Kanda (Keigaku, Tokyo), p. 361 (1971).
67. Fisher, M.P., Quantum phase transitions in disordered two-dimensional superconductors. Physical Review Letters, **65** (7), p.923 (1990).
68. Breznay, N.P., Steiner, M.A., Kivelson, S.A. and Kapitulnik, A., Self-duality and a Hall-insulator phase near the superconductor-to-insulator transition in indium-oxide films. Proceedings of the National Academy of Sciences, **113** (2), pp.280-285 (2016).
69. Seidemann, J., Sacépé, B., Ovadia, M., Shahar, D. and Feigel'man, M.V., Low-temperature anomalies in disordered superconducting films near $ B_ {c2} $. arXiv preprint arXiv:1609.07105 (2016).
70. Baturina, T.Y.I., Islamov, D.R., Bentner, J., Strunk, C., Baklanov, M.R. and Satta, A., Superconductivity on the localization threshold and magnetic-field-tuned superconductor-insulator transition in TiN films. Journal of Experimental and Theoretical Physics Letters, **79** (7), pp.337-341 (2004).
71. Ovadia, M., Kalok, D., Sacépé, B. and Shahar, D., Duality symmetry and its breakdown in the vicinity of the superconductor–insulator transition. Nature Physics, **9** (7), p.415 (2013).

72. Fazio, R. and Schön, G., Charge and vortex dynamics in arrays of tunnel junctions. Physical Review B, **43** (7), p.5307 (1991).
73. Baturina, T.I. and Vinokur, V.M., Superinsulator–superconductor duality in two dimensions. Annals of Physics, **331**, pp.236-257 (2013).
74. Chtchelkatchev, N.M., Vinokur, V.M. and Baturina, T.I., Low temperature transport in tunnel junction arrays: Cascade energy relaxation. In Physical Properties of Nanosystems (pp. 25-44) (2011). Springer, Dordrecht.
75. Yazdani, A. and Kapitulnik, A., Superconducting-insulating transition in two-dimensional a-MoGe thin films. Physical review letters, **74** (15), p.3037 (1995).
76. Bielejec, E. and Wu, W., Field-tuned superconductor-insulator transition with and without current bias. Physical review letters, **88** (20), p.206802 (2002).
77. Okuma, S. and Kokubo, N., Field-induced superconductor-insulator transition and grain size in thin granular films of indium. Solid state communications, **93** (12), pp.1019-1023 (1995).
78. Rainis, D. and Loss, D., Majorana qubit decoherence by quasiparticle poisoning. Physical Review B, **85** (17), p.174533 (2012).
79. Kalok, D., Bilušić, A., Baturina, T.I., Mironov, A.Y., Postolova, S.V., Gutakovskii, A.K., Latyshev, A.V., Vinokur, V.M. and Strunk, C., Non-linear conduction in the critical region of the superconductor-insulator transition in TiN thin films. In Journal of Physics: Conference Series (Vol. **400**, No. 2, p. 022042 (2012)). IOP Publishing.
80. Kosterlitz, J.M. and Thouless, D.J., Ordering, metastability and phase transitions in two-dimensional systems (1973). Journal of Physics C: Solid State Physics, **6** (7), p.1181.Jos, J.V., (2013).
81. 40 years of Berezinskii-Kosterlitz-Thouless theory. World Scientific.
82. Berezinskii, V.L., Destruction of long-range order in one-dimensional and two-dimensional systems having a continuous symmetry group I. Classical systems. Sov. Phys. JETP, **32** (3), pp.493-500 (1971).
83. Anderson, P.W., Absence of diffusion in certain random lattices. Physical review, **109** (5), p.1492 (1958).
84. Proskurin, I., Ovchinnikov, A.S. and Kishine, J.I., October. On Berezinskii-Kosterlitz-Thouless transition in monoaxial chiral helimagnets. In Journal of Physics: Conference Series (**903**, 1, p. 012062 (2017)). IOP Publishing.
85. Kogan, V.G., Interaction of vortices in thin superconducting films and the Berezinskii-Kosterlitz-Thouless transition. Physical Review B, **75** (6), p.064514 (2007).

86. Hadzibabic, Z., Krüger, P., Cheneau, M., Battelier, B. and Dalibard, J., Berezinskii–Kosterlitz–Thouless crossover in a trapped atomic gas. Nature, **441** (7097), p.1118 (2006).
87. Glazman, L.I. and Koshelev, A.E., Thermal fluctuations and phase transitions in the vortex state of a layered superconductor. Physical Review B, **43** (4), p.2835 (1991).
88. Tang, Z.K., Zhang, L., Wang, N., Zhang, X.X., Wen, G.H., Li, G.D., Wang, J.N., Chan, C.T. and Sheng, P., Superconductivity in 4 angstrom single-walled carbon nanotubes. Science, **292** (5526), pp.2462-2465 (2001).
89. Lin, Y.H., Nelson, J. and Goldman, A.M., Suppression of the Berezinskii-Kosterlitz-Thouless transition in 2D superconductors by macroscopic quantum tunneling. Physical review letters, **109** (1), p.017002 (2012).
90. Benfatto, L., Castellani, C. and Giamarchi, T., Broadening of the Berezinskii-Kosterlitz-Thouless superconducting transition by inhomogeneity and finite-size effects. Physical Review B, **80** (21), p.214506 (2009).
91. Caviglia, A.D., Gariglio, S., Reyren, N., Jaccard, D., Schneider, T., Gabay, M., Thiel, S., Hammerl, G., Mannhart, J. and Triscone, J.M., Electric field control of the LaAlO 3/SrTiO 3 interface ground state. Nature, **456** (7222), p.624 (2008).
92. Halperin, B.I. and Nelson, D.R., Resistive transition in superconducting films. Journal of Low Temperature Physics, **36** (5-6), pp.599-616 (1979).
93. Minnhagen, P., The two-dimensional Coulomb gas, vortex unbinding, and superfluid-superconducting films. Reviews of modern physics, **59** (4), p.1001 (1987).
94. Zhao, M., Dong, W. and Wang, A., Two-dimensional carbon topological insulators superior to graphene. Scientific reports, **3**, p.3532 (2013).
95. Feng, B., Sugino, O., Liu, R.Y., Zhang, J., Yukawa, R., Kawamura, M., Iimori, T., Kim, H., Hasegawa, Y., Li, H. and Chen, L., Dirac fermions in borophene. Physical review letters, **118** (9), p.096401 (2017).
96. König, J., Schoeller, H. and Schön, G., Zero-bias anomalies and boson-assisted tunneling through quantum dots. Physical review letters, **76** (10), p.1715 (1996).
97. Lee, E.J., Jiang, X., Aguado, R., Katsaros, G., Lieber, C.M. and De Franceschi, S., Zero-bias anomaly in a nanowire quantum dot coupled to superconductors. Physical review letters, **109** (18), p.186802 (2012).
98. Ghosh, A., Wright, M.H., Siegert, C., Pepper, M., Farrer, I., Ford, C.J.B. and Ritchie, D.A., Zero-bias anomaly and kondo-assisted quasiballistic 2D transport. Physical review letters, **95** (6), p.066603 (2005).

99. Martinek, J., Utsumi, Y., Imamura, H., Barnaś, J., Maekawa, S., König, J. and Schön, G., Kondo effect in quantum dots coupled to ferromagnetic leads. Physical review letters, **91** (12), p.127203 (2003).

100. Appelbaum, J.A., Exchange model of zero-bias tunneling anomalies. Physical Review, **154** (3), p.633 (1967).

101. Hu, Chia-Ren. "Origin of the zero-bias conductance peaks observed ubiquitously in high-T c superconductors." Physical Review B, **57**, no. 2 (1998): 1266.

102. Fogelström, M., Rainer, D. and Sauls, J.A., Tunneling into current-carrying surface states of high-T c superconductors. Physical review letters, **79** (2), p.281 (1997).

103. Ekin, J.W., Xu, Y., Mao, S., Venkatesan, T., Face, D.W., Eddy, M. and Wolf, S.A., Correlation between d-wave pairing behavior and magnetic-field-dependent zero-bias conductance peak. Physical Review B, **56** (21), p.13746 (1997).

104. Tikhonenko, F.V., Kozikov, A.A., Savchenko, A.K. and Gorbachev, R.V., Transition between electron localization and antilocalization in graphene. Physical Review Letters, **103** (22), p.226801 (2009).

105. Liu, M., Zhang, J., Chang, C.Z., Zhang, Z., Feng, X., Li, K., He, K., Wang, L.L., Chen, X., Dai, X. and Fang, Z., Crossover between weak antilocalization and weak localization in a magnetically doped topological insulator. Physical review letters, **108** (3), p.036805 (2012).

106. Morpurgo, A.F. and Guinea, F., Intervalley scattering, long-range disorder, and effective time-reversal symmetry breaking in graphene. Physical Review Letters, **97** (19), p.196804 (2006).

107. Fu, L. and Kane, C.L., Topological insulators with inversion symmetry. Physical Review B, **76** (4), p.045302 (2007).

108. Himpsel, F.J., Eastman, D.E., Heimann, P. and Van der Veen, J.F., Surface states on reconstructed diamond (111). Physical Review B, **24** (12), p.7270 (1981).

109. Takahide, Y., Okazaki, H., Deguchi, K., Uji, S., Takeya, H., Takano, Y., Tsuboi, H. and Kawarada, H., Quantum oscillations of the two-dimensional hole gas at atomically flat diamond surfaces. Physical Review B, **89** (23), p.235304 (2014).

110. Ager III, J.W., Walukiewicz, W., McCluskey, M., Plano, M.A. and Landstrass, M.I., Fano interference of the Raman phonon in heavily boron-doped diamond films grown by chemical vapor deposition. Applied Physics Letters, **66** (5), pp.616-618 (1995).

111. Hikami, S., Larkin, A.I. and Nagaoka, Y., Spin-orbit interaction and magnetoresistance in the two dimensional random system. Progress of Theoretical Physics, **63** (2), pp.707-710 (1980).

112. Adroguer, P., Liu, W.E., Culcer, D. and Hankiewicz, E.M., Conductivity corrections for topological insulators with spin-orbit impurities: Hikami-Larkin-Nagaoka formula revisited. Physical Review B, **92** (24), p.241402 (2015).

113. Huang, X., Zhao, L., Long, Y., Wang, P., Chen, D., Yang, Z., Liang, H., Xue, M., Weng, H., Fang, Z. and Dai, X., Observation of the chiral-anomaly-induced negative magnetoresistance in 3D Weyl semimetal TaAs. Physical Review X, **5** (3), p.031023 (2015).

114. Gorbar, E.V., Miransky, V.A. and Shovkovy, I.A., Chiral anomaly, dimensional reduction, and magnetoresistivity of Weyl and Dirac semimetals. Physical Review B, **89** (8), p.085126 (2014).

115. Landsteiner, K., Anomalous transport of Weyl fermions in Weyl semimetals. Physical Review B, **89** (7), p.075124 (2014).

116. Li, C.Z., Wang, L.X., Liu, H., Wang, J., Liao, Z.M. and Yu, D.P., Giant negative magnetoresistance induced by the chiral anomaly in individual Cd 3 As 2 nanowires. Nature communications, **6**, p.10137 (2015).

117. Deng, K., Wan, G., Deng, P., Zhang, K., Ding, S., Wang, E., Yan, M., Huang, H., Zhang, H., Xu, Z. and Denlinger, J., Experimental observation of topological Fermi arcs in type-II Weyl semimetal MoTe 2. Nature Physics, **12** (12), p.1105 (2016).

118. Wallace, P.R., The band theory of graphite. Physical Review, **71** (9), p.622 (1947).

119. Novoselov, K.S., Geim, A.K., Morozov, S., Jiang, D., Katsnelson, M., Grigorieva, I., Dubonos, S. and Firsov, A.A., Two-dimensional gas of massless Dirac fermions in graphene. Nature, **438** (7065), p.197 (2005).

120. Novoselov, K.S., McCann, E., Morozov, S.V., Fal'ko, V.I., Katsnelson, M.I., Zeitler, U., Jiang, D., Schedin, F. and Geim, A.K., Unconventional quantum Hall effect and Berry's phase of 2π in bilayer graphene. Nature physics, **2** (3), p.177 (2006).

121. Herbut, I.F., Theory of integer quantum Hall effect in graphene. Physical Review B, **75** (16), p.165411 (2007).

122. Du, X., Skachko, I., Duerr, F., Luican, A. and Andrei, E.Y., Fractional quantum Hall effect and insulating phase of Dirac electrons in graphene. Nature, **462** (7270), p.192 (2009).

123. Neto, A.C., Guinea, F., Peres, N.M., Novoselov, K.S. and Geim, A.K., The electronic properties of graphene. Reviews of modern physics, **81** (1), p.109 (2009.).

124. Kailasvuori, J., Pedestrian index theorem à la Aharonov-Casher for bulk threshold modes in corrugated multilayer graphene. EPL (Europhysics Letters), **87** (4), p.47008 (2009.).

125. Katsnelson, M.I., Zitterbewegung, chirality, and minimal conductivity in graphene. The European Physical Journal B-Condensed Matter and Complex Systems, **51** (2), pp.157-160 (2006).

126. Morozov, S.V., Novoselov, K.S., Katsnelson, M.I., Schedin, F., Ponomarenko, L.A., Jiang, D. and Geim, A.K., Strong suppression of weak localization in graphene. Physical review letters, **97** (1), p.016801 (2006).

127. Kim, K.S., Zhao, Y., Jang, H., Lee, S.Y., Kim, J.M., Kim, K.S., Ahn, J.H., Kim, P., Choi, J.Y. and Hong, B.H., Large-scale pattern growth of graphene films for stretchable transparent electrodes. Nature, **457** (7230), p.706 (2009).

128. Wei, D., Liu, Y., Wang, Y., Zhang, H., Huang, L. and Yu, G., Synthesis of N-doped graphene by chemical vapor deposition and its electrical properties. Nano letters, **9** (5), pp.1752-1758 (2009).

129. Wang, H., Zhou, Y., Wu, D., Liao, L., Zhao, S., Peng, H. and Liu, Z., Synthesis of boron-doped graphene monolayers using the sole solid feedstock by chemical vapor deposition. Small, **9** (8), pp.1316-1320 (2013).

130. Vlassiouk, I., Smirnov, S., Ivanov, I., Fulvio, P.F., Dai, S., Meyer, H., Chi, M., Hensley, D., Datskos, P. and Lavrik, N.V., Electrical and thermal conductivity of low temperature CVD graphene: the effect of disorder. Nanotechnology, **22** (27), p.275716 (2011).

131. Han, M.Y., Özyilmaz, B., Zhang, Y. and Kim, P., Energy band-gap engineering of graphene nanoribbons. Physical review letters, **98** (20), p.206805 (2007).

132. Roy, B. and Juričić, V., Strain-induced time-reversal odd superconductivity in graphene. Physical Review B, **90** (4), p.041413 (2014).

133. Levy, N., Burke, S.A., Meaker, K.L., Panlasigui, M., Zettl, A., Guinea, F., Neto, A.C. and Crommie, M.F., Strain-induced pseudo–magnetic fields greater than 300 tesla in graphene nanobubbles. Science, **329** (5991), pp.544-547 (2010).

134. De Juan, F., Cortijo, A., Vozmediano, M.A. and Cano, A., Aharonov–Bohm interferences from local deformations in graphene. Nature Physics, **7** (10), p.810 (2011).

135. Benameur, M.M., Gargiulo, F., Manzeli, S., Autès, G., Tosun, M., Yazyev, O.V. and Kis, A., Electromechanical oscillations in bilayer graphene. Nature communications, **6**, p.8582 (2015).

136. Lu, Y. and Guo, J., Band gap of strained graphene nanoribbons. Nano Research, **3** (3), pp.189-199 (2010).

137. Ferrari, A.C. and Basko, D.M., Raman spectroscopy as a versatile tool for studying the properties of graphene. Nature nanotechnology, **8** (4), p.235 (2013).

138. Hao, Y., Wang, Y., Wang, L., Ni, Z., Wang, Z., Wang, R., Koo, C.K., Shen, Z. and Thong, J.T., Probing layer number and stacking order of few-layer graphene by Raman spectroscopy. small, **6** (2), pp.195-200 (2010).

139. Ferrari, A.C., Raman spectroscopy of graphene and graphite: disorder, electron–phonon coupling, doping and nonadiabatic effects. Solid state communications, **143** (1-2), pp.47-57 (2007).

140. Ferreira, E.M., Moutinho, M.V., Stavale, F., Lucchese, M.M., Capaz, R.B., Achete, C.A. and Jorio, A., Evolution of the Raman spectra from single-, few-, and many-layer graphene with increasing disorder. Physical Review B, **82** (12), p.125429 (2010).

141. Malard, L.M., Pimenta, M.A.A., Dresselhaus, G. and Dresselhaus, M.S., Raman spectroscopy in graphene. Physics Reports, **473** (5-6), pp.51-87 (2009).

142. Cançado, L.G., Jorio, A., Ferreira, E.M., Stavale, F., Achete, C.A., Capaz, R.B., Moutinho, M.V.O., Lombardo, A., Kulmala, T.S. and Ferrari, A.C., Quantifying defects in graphene via Raman spectroscopy at different excitation energies. Nano letters, **11** (8), pp.3190-3196 (2011).

143. Das, A., Chakraborty, B. and Sood, A.K., Raman spectroscopy of graphene on different substrates and influence of defects. Bulletin of Materials Science, **31** (3), pp.579-584 (2008).

144. Ferrari, A.C., Raman spectroscopy of graphene and graphite: disorder, electron–phonon coupling, doping and nonadiabatic effects. Solid state communications, **143** (1-2), pp.47-57 (2007).

145. Tuinstra, F. and Koenig, J.L., Raman spectrum of graphite. The Journal of Chemical Physics, **53** (3), pp.1126-1130 (1970).

146. Huang, M., Yan, H., Heinz, T.F. and Hone, J., Probing strain-induced electronic structure change in graphene by Raman spectroscopy. Nano letters, **10** (10), pp.4074-4079 (2010).

147. Lee, J.E., Ahn, G., Shim, J., Lee, Y.S. and Ryu, S., Optical separation of mechanical strain from charge doping in graphene. Nature communications, **3**, p.1024 (2012).

148. Krauss, B., Lohmann, T., Chae, D.H., Haluska, M., von Klitzing, K. and Smet, J.H., Laser-induced disassembly of a graphene single crystal into a nanocrystalline network. Physical Review B, **79** (16), p.165428 (2009).

149. Li, J., Chung, T.F., Chen, Y.P. and Cheng, G.J., Nanoscale strainability of graphene by laser shock-induced three-dimensional shaping. Nano letters, **12** (9), pp.4577-4583 (2012).

150. Roberts, A., Cormode, D., Reynolds, C., Newhouse-Illige, T., LeRoy, B.J. and Sandhu, A.S., Response of graphene to femtosecond high-intensity laser irradiation. Applied Physics Letters, **99** (5), p.051912 (2011).

151. Mohiuddin, T.M.G., Lombardo, A., Nair, R.R., Bonetti, A., Savini, G., Jalil, R., Bonini, N., Basko, D.M., Galiotis, C., Marzari, N. and Novoselov, K.S., Uniaxial strain in graphene by Raman spectroscopy: G peak splitting, Grüneisen parameters, and sample orientation. Physical Review B, **79** (20), p.205433 (2009).

152. Zhou, S.Y., Gweon, G.H., Fedorov, A.V., First, P.N., De Heer, W.A., Lee, D.H., Guinea, F., Neto, A.C. and Lanzara, A., Substrate-induced bandgap opening in epitaxial graphene. Nature materials, **6** (10), p.770 (2007).

153. Ni, Z.H., Yu, T., Lu, Y.H., Wang, Y.Y., Feng, Y.P. and Shen, Z.X., Uniaxial strain on graphene: Raman spectroscopy study and band-gap opening. ACS nano, **2** (11), pp.2301-2305 (2008).

154. Das, A., Pisana, S., Chakraborty, B., Piscanec, S., Saha, S.K., Waghmare, U.V., Novoselov, K.S., Krishnamurthy, H.R., Geim, A.K., Ferrari, A.C. and Sood, A.K., 2008. Monitoring dopants by Raman scattering in an electrochemically top-gated graphene transistor. Nature nanotechnology, **3** (4), pp.nnano (2008).

155. Faugeras, C., Amado, M., Kossacki, P., Orlita, M., Kühne, M., Nicolet, A.A.L., Latyshev, Y.I. and Potemski, M., Magneto-Raman scattering of graphene on graphite: electronic and phonon excitations. Physical review letters, **107** (3), p.036807 (2011).

156. Berciaud, S., Potemski, M. and Faugeras, C., Probing electronic excitations in mono-to pentalayer graphene by micro magneto-Raman spectroscopy. Nano letters, **14** (8), pp.4548-4553 (2014).

157. Kashuba, O. and Fal'ko, V.I., Role of electronic excitations in magneto-Raman spectra of graphene. New Journal of Physics, **14** (10), p.105016 (2012).

158. Liang, X., Jung, Y.S., Wu, S., Ismach, A., Olynick, D.L., Cabrini, S. and Bokor, J., Formation of bandgap and subbands in graphene nanomeshes with sub-10 nm ribbon width fabricated via nanoimprint lithography. Nano letters, **10** (7), pp.2454-2460 (2010).

159. Kisslinger, F., Ott, C., Heide, C., Kampert, E., Butz, B., Spiecker, E., Shallcross, S. and Weber, H.B., Linear magnetoresistance in mosaic-like bilayer graphene. Nature Physics, **11** (8), p.650 (2015).

160. Vasileva, G.Y., Smirnov, D., Ivanov, Y.L., Vasilyev, Y.B., Alekseev, P.S., Dmitriev, A.P., Gornyi, I.V., Kachorovskii, V.Y., Titov, M., Narozhny, B.N. and Haug, R.J., Linear magnetoresistance in compensated graphene bilayer. Physical Review B, **93** (19), p.195430 (2016).

161. Abrikosov, A.A., Quantum linear magnetoresistance. EPL (Europhysics Letters), **49** (6), p.789 (2000).

162. Abrikosov, A.A., Quantum linear magnetoresistance; solution of an old mystery. Journal of Physics A: Mathematical and General, **36** (35), p.9119 (2003).

163. Zhu, W., Perebeinos, V., Freitag, M. and Avouris, P., Carrier scattering, mobilities, and electrostatic potential in monolayer, bilayer, and trilayer graphene. Physical Review B, **80** (23), p.235402 (2009).

164. Zhang, Y., Small, J.P., Amori, M.E. and Kim, P., Electric field modulation of galvanomagnetic properties of mesoscopic graphite. Physical review letters, **94** (17), p.176803 (2005).

165. Hibino, H., Kageshima, H., Kotsugi, M., Maeda, F., Guo, F.Z. and Watanabe, Y., Dependence of electronic properties of epitaxial few-layer graphene on the number of layers investigated by photoelectron emission microscopy. Physical Review B, **79** (12), p.125437 (2009).

166. Latil, S. and Henrard, L., Charge carriers in few-layer graphene films. Physical Review Letters, **97** (3), p.036803 (2006).

167. Yoshioka, D., Effect of the Landau level mixing on the ground state of two-dimensional electrons. Journal of the Physical Society of Japan, **53** (11), pp.3740-3743 (1984).

168. Ghaemi, P., Cayssol, J., Sheng, D.N. and Vishwanath, A., Fractional topological phases and broken time-reversal symmetry in strained graphene. Physical review letters, **108** (26), p.266801.

169. Tan, Z., Tan, C., Ma, L., Liu, G.T., Lu, L. and Yang, C.L., Shubnikov-de Haas oscillations of a single layer graphene under dc current bias. Physical Review B, **84** (11), p.115429 (2011).

170. Castro, E.V., Novoselov, K.S., Morozov, S.V., Peres, N.M.R., Dos Santos, J.L., Nilsson, J., Guinea, F., Geim, A.K. and Neto, A.C., Biased bilayer graphene: semiconductor with a gap tunable by the electric field effect. Physical review letters, **99** (21), p.216802 (2007).

171. Berger, C., Song, Z., Li, T., Li, X., Ogbazghi, A.Y., Feng, R., Dai, Z., Marchenkov, A.N., Conrad, E.H., First, P.N. and De Heer, W.A., Ultrathin epitaxial graphite: 2D electron gas properties and a route toward graphene-based nanoelectronics. The Journal of Physical Chemistry B, **108** (52), pp.19912-19916 (2004).

172. Novoselov, K.S., Geim, A.K., Morozov, S.V., Jiang, D., Zhang, Y., Dubonos, S.V., Grigorieva, I.V. and Firsov, A.A., Electric field effect in atomically thin carbon films. Science, **306** (5696), pp.666-669 (2004).

173. Martin, K.P., Higgins, R.J., Rascol, J.J.L., Yoo, H. and Arthur, J.R., Quantum lifetime measurements of the two-dimensional electron gas at the inverted AlGaAs/GaAs interface. Surface Science, **196** (1-3), pp.323-327 (1988).

174. Tan, Z., Tan, C., Ma, L., Liu, G.T., Lu, L. and Yang, C.L., Shubnikov-de Haas oscillations of a single layer graphene under dc current bias. Physical Review B, **84** (11), p.115429 (2011).

175. Hwang, E.H. and Sarma, S.D., Single-particle relaxation time versus transport scattering time in a two-dimensional graphene layer. Physical Review B, **77** (19), p.195412 (2008).

176. Staley, N.E., Puls, C.P. and Liu, Y., Suppression of conductance fluctuation in weakly disordered mesoscopic graphene samples near the charge neutral point. Physical Review B, **77** (15), p.155429 (2008).

177. Liang, Q., Cressler, J.D., Niu, G., Lu, Y., Freeman, G., Ahlgren, D.C., Malladi, R.M., Newton, K. and Harame, D.L., A simple four-port parasitic deembedding methodology for high-frequency scattering parameter and noise characterization of SiGe HBTs. IEEE Transactions on Microwave Theory and Techniques, **51** (11), pp.2165-2174 (2003).

178. Vendelin, G.D., Pavio, A.M. and Rohde, U.L., Microwave circuit design using linear and nonlinear techniques. John Wiley & Sons (2005).

179. Bhattacharyya, S., Henley, S.J., Mendoza, E., Gomez-Rojas, L., Allam, J. and Silva, S.R.P., Resonant tunnelling and fast switching in amorphous-carbon quantum-well structures. Nature Materials, **5** (1), p.19 (2006).

180. Chimowa, G., Ncube, S. and Bhattacharyya, S., Observation of impedance oscillations in single-walled carbon nanotube bundles excited by high-frequency signals. EPL (Europhysics Letters), **111** (3), p.36001 (2015).

181. Chimowa, G., Flahaut, E. and Bhattacharyya, S., Temperature-dependent diffusive to ballistic transport transition in aligned double walled carbon nanotubes in the high frequency regime. Applied Physics Letters, **105** (17), p.173511 (2014).

182. http://www.graphene.ac.rs/exfoliation.html

183. Han, Z., Allain, A., Arjmandi-Tash, H., Tikhonov, K., Feigel'Man, M., Sacépé, B. and Bouchiat, V., Collapse of superconductivity in a hybrid tin–graphene Josephson junction array. Nature Physics, **10** (5), p.380 (2014).

184. Kang, W.P., Davidson, J.L., Wong, Y.M. and Holmes, K., Diamond vacuum field emission devices. Diamond and related materials, **13** (4-8), pp.975-981 (2004).

185. Subramanian, K., Kang, W.P. and Davidson, J.L., A monolithic nanodiamond lateral field emission vacuum transistor. IEEE Electron Device Letters, **29** (11), pp.1259-1261 (2008).

186. Toyli, D.M., Weis, C.D., Fuchs, G.D., Schenkel, T. and Awschalom, D.D., Chip-scale nanofabrication of single spins and spin arrays in diamond. Nano letters, **10** (8), pp.3168-3172 (2010).

187. Hausmann, B.J., Babinec, T.M., Choy, J.T., Hodges, J.S., Hong, S., Bulu, I., Yacoby, A., Lukin, M.D. and Lončar, M., Single-color centers implanted in diamond nanostructures. New Journal of Physics, **13** (4), p.045004 (2011).

188. Titova, N., Kardakova, A.I., Tovpeko, N., Ryabchun, S., Mandal, S., Morozov, D., Klemencic, G.M., Giblin, S.R., Williams, O.A., Goltsman, G.N. and Klapwijk, T.M., Slow Electron–Phonon Cooling in Superconducting Diamond Films. IEEE Transactions on Applied Superconductivity, **27** (4), pp.1-4 (2017).

189. Kardakova, A., Shishkin, A., Semenov, A., Goltsman, G.N., Ryabchun, S., Klapwijk, T.M., Bousquet, J., Eon, D., Sacépé, B., Klein, T. and Bustarret, E., Relaxation of the resistive superconducting state in boron-doped diamond films. Physical Review B, **93** (6), p.064506 (2016).

190. Mandal, S., Bautze, T., Williams, O.A., Naud, C., Bustarret, E., Omnes, F., Rodiere, P., Meunier, T., Bäuerle, C. and Saminadayar, L., The diamond superconducting quantum interference device. ACS nano, **5** (9), pp.7144-7148 (2011).

191. Watanabe, M., Kawano, A., Kitagoh, S., Yamaguchi, T., Takano, Y. and Kawarada, H., Stacked SNS Josephson junction of all boron doped diamond. Physica C: Superconductivity and its applications, **470**, pp.S613-S615 (2010).

192. Hilgenkamp, H., Pi-phase shift Josephson structures. Superconductor science and technology, **21** (3), p.034011 (2008).

193. Pal, A., Ouassou, J.A., Eschrig, M., Linder, J. and Blamire, M.G., Spectroscopic evidence of odd frequency superconducting order. Scientific reports, **7**, p.40604 (2017).

194. Stern, A. and Lindner, N.H., Topological quantum computation—from basic concepts to first experiments. Science, **339** (6124), pp.1179-1184 (2013).

195. Van Harlingen, D.J., Hilliard, J.E., Plourde, B.L.T. and Yanoff, B.D., Extending SQUID interferometry beyond the cuprates and beyond d-wave symmetry. Physica C: Superconductivity, **317**, pp.410-420 (1999).

196. Tholén, E.A., Ergül, A., Stannigel, K., Hutter, C. and Haviland, D.B., Parametric amplification with weak-link nonlinearity in superconducting microresonators. Physica Scripta, (T137), p.014019 (2009).

197. Chimowa, G., Erasmus, R.M. and Bhattacharyya, S., High-frequency electrical transport in nitrogen incorporated nano-crystalline diamond films in the GHz regime. EPL (Europhysics Letters), **109** (6), p.67002 (2015).

List of Publications

1. Coleman, C. and Bhattacharyya, S., Possible observation of the Berezinskii-Kosterlitz-Thouless transition in boron-doped diamond films. AIP Advances, **7** (11), p.115119 (2017).
2. Coleman, C., Mtsuko, D., Botha, C., Sandrock, C. and Bhattacharyya, S., Quantum Linear Magnetoresistance and Shubnikov De-Haas Oscillation in Suspended Wrinkled and Smooth Multilayer Graphene. Journal of Nanoscience and Nanotechnology, **17** (8), pp.5408-5414 (2017).
3. Coleman, C., Khorasani, S., Ncube, S., Mtsuko, D., Botha, C., Sandrock, C., Fernandes, M., Levendis, D. and Bhattacharyya, S., February. Nanomanipulation device fabrication: multilayerd graphene and OFET devices. In Fourth Conference on Sensors, MEMS, and Electro-Optic Systems (Vol. **10036**, p. 1003608 (2017)). International Society for Optics and Photonics.
4. Urgessa, Z.N., Botha, J.R., Djiokap, S.T., Coleman, C. and Bhattacharyya, S., Patterned growth of ZnO nanorods by chemical bath deposition. Physica B: Condensed Matter, **535**, p. 79 (2017).
5. Coleman, C., Erasmus, R. and Bhattacharyya, S., Nanoscale deformations in graphene by laser annealing. Applied Physics Letters, **109** (25), p.253102 (2016).
6. Mtsuko, D., Aslan, T., Ncube, S., Coleman, C., Wamwangi, D. and Bhattacharyya, S., Observation of Aharonov-Bohm and Al'tshuler-Aronov-Spivak oscillations in the background of universal conductance fluctuations in silicon nanowires. EPL (Europhysics Letters), **113** (4), p.47002 (2016).
7. Coleman, C., McIntosh, R. and Bhattacharyya, S., Controlling the activation energy of graphene-like thin films through disorder induced localization. Journal of Applied Physics, **114** (4), p.043716 (2013).